

# Quantification of primary and secondary organic aerosol sources by combined factor analysis of extractive electrospray ionisation and aerosol mass spectrometer measurements (EESI-TOF and AMS)

Yandong Tong<sup>1,\*</sup>, Lu Qi<sup>1</sup>, Giulia Stefenelli<sup>1</sup>, Dongyu S. Wang<sup>1</sup>, Francesco Canonaco<sup>1</sup>, Urs Baltensperger<sup>1</sup>, André S.H. Prévôt<sup>1</sup>, Jay G. Slowik<sup>1,‡</sup>

<sup>1</sup>Laboratory of Atmospheric Chemistry, Paul Scherrer Institute (PSI), 5232 Villigen, Switzerland

<sup>‡</sup>[Now at Department of Chemistry, University of Colorado, Boulder, 80310, USA](#)

*Correspondence* to Jay Slowik ([jay.slowik@psi.ch](mailto:jay.slowik@psi.ch))

## Abstract:

Source apportionment studies have struggled to quantitatively link secondary organic aerosol (SOA) to its precursor sources, due largely to instrument limitations. For example, aerosol mass spectrometers (AMS) provide quantitative measurements of the total SOA fraction, but lack the chemical resolution to resolve most SOA sources. In contrast, instruments based on soft ionisation techniques, such as extractive electrospray ionisation mass spectrometry (EESI, e.g., the EESI time of flight mass spectrometer, EESI-TOF), have demonstrated the resolution to identify specific SOA sources but provide only a semi-quantitative apportionment due to uncertainties in the dependence of instrument sensitivity on molecular identity. We address this challenge by presenting a method for positive matrix factorisation (PMF) analysis on a single dataset which includes measurements from both AMS and EESI-TOF instruments, denoted “combined PMF” (cPMF). Because each factor profile includes both AMS and EESI-TOF components, the cPMF analysis maintains the source resolution capability of the EESI-TOF, while also providing quantitative factor mass concentrations. Therefore, the bulk EESI-TOF sensitivity to each factor can also be directly determined from the analysis. We present metrics for ensuring both instruments are well-represented in the solution, a method for optionally constraining factor profile contributions for the profiles of factors that are detectable by one or both instruments, and a protocol for uncertainty analysis.

As a proof of concept, the cPMF analysis was applied to summer and winter measurements in Zurich, Switzerland. Factors related to biogenic and wood burning-derived SOA are quantified, as well as POA sources such as wood burning, cigarette smoke, cooking, and traffic. The retrieved EESI-TOF factor-dependent sensitivities are consistent with both laboratory measurements of SOA from model precursors and bulk sensitivity parameterisations based on ion chemical formulae. The cPMF analysis shows that with the standalone EESI-TOF PMF, in which factor-dependent sensitivities are not accounted for, some factors are significantly under/overestimated. For example, when factor-dependent sensitivities are not considered in the winter dataset, the SOA fraction is underestimated by ~25% due to the high EESI-TOF sensitivity to components of primary biomass burning such as levoglucosan. In the summer dataset, where both SOA and total OA are dominated by monoterpene oxidation products, the uncorrected EESI-TOF underestimates the fraction of daytime SOA relative to nighttime SOA (in which organonitrates

Formatted: English (United States)

Formatted: English (United States)

Formatted: English (United States)

Formatted: English (United States)

Formatted: English (United States)

Formatted: English (United States)

Formatted: English (United States)

1 and less oxygenated C<sub>x</sub>H<sub>y</sub>O<sub>z</sub> molecules are enhanced). Although applied here to an AMS/EESI-  
2 TOF pairing, cPMF is suitable for the general case of a multi-instrument dataset, thereby  
3 providing a framework for exploiting semi-quantitative, high-resolution instrumentation for  
4 quantitative source apportionment.

## 5 6 1. Introduction

7  
8 Atmospheric aerosols negatively affect visibility (Chow et al., 2002), human health (Pope et al., 2002;  
9 Laden et al., 2006; Beelen et al., 2014; Laden et al., 2006; Pope et al., 2002), and urban air quality  
10 (Fenger, 1999; Mayer, 1999) on local and regional scales. Aerosols also provide the largest uncertainties  
11 for global radiation balance and climate change (Myhre et al., 2014; Penner et al., 2011; Forster et al.,  
12 2007; Lohmann and Feichter, 2005; Forster et al., 2007; Penner et al., 2011; Myhre et al., 2014).  
13 Therefore, to develop appropriate mitigation policies, it is of vital importance to understand aerosol  
14 chemical composition, sources, and evolution. Organic aerosol (OA) is a major component of  
15 atmospheric aerosol and accounts for 20 to 90 % of the submicron aerosol mass (Jimenez et al., 2009).  
16 OA is typically classified as either primary organic aerosol (POA), which is directly emitted to the  
17 atmosphere, or secondary organic aerosol (SOA), which is produced by atmospheric reactions of  
18 emitted volatile organic compounds (VOCs). Both POA and SOA can exert serious health effects,  
19 including protein and DNA damage caused by reactive oxygen species (ROS), which can be either  
20 contained in the particles or induced by oxidation reactions following inhalation (FullerHalliwell and  
21 Cross, 1994; Li et al., 2014; 2003; Reuter et al., 2010; Kelly and Fussell, 2012; ReuterFuller et al., 2010;  
22 Li et al., 2003; Halliwell and Cross, 1994; 2014). Recent studies indicate that the oxidation potential of  
23 SOA is source-dependent. Therefore, different sources likely carry different health risks, highlighting  
24 the importance of OA source identification and quantification (Zhou et al., 2018; Daellenbach et al.,  
25 2020; Zhou et al., 2018). Previous studies have been relatively successful in quantitatively linking POA  
26 to its sources. However, quantification of SOA sources and/or formation pathways is more challenging  
27 due to 1) the chemical complexity of SOA, which can consist of thousands of unique oxidation products,  
28 including highly oxygenated molecules and high molecular weight organic oligomers, and 2) limitations  
29 of traditional instrumentation for characterising OA chemical composition, especially the SOA fraction.  
30 Therefore, the effects of individual SOA sources on health and climate remain poorly constrained.

31  
32 Positive matrix factorisation (PMF) is a widely used source apportionment technique. PMF is a bilinear  
33 receptor model which represents the measured mass spectral time series as a linear combination of  
34 factor mass spectra and their corresponding time-dependent concentrations (Paatero and Tapper,  
35 1994)(Paatero and Tapper, 1994). These factors may then be related to emission sources, and/or  
36 atmospheric processes, depending on their chemical and temporal characteristics. PMF has been  
37 implemented in extensive online and offline studies worldwide to quantify OA sources. The Aerodyne  
38 aerosol mass spectrometer (AMS) is widely used in OA source apportionment studies because it  
39 provides online, quantitative measurements of non-refractory PM<sub>1</sub> or PM<sub>2.5</sub> (particulate matter with  
40 aerodynamic diameter smaller than 1 or 2.5 μm, respectively) chemical composition with high time  
41 resolution. Source apportionment studies using PMF based on AMS data have successfully separated  
42 and quantified POA sources based on different chemical signatures, e.g., hydrocarbon-like OA (HOA)  
43 (ZhaoNg et al., 2019; Xu2011b; Zhang et al., 2019; Sun et al., 2016a; 2014; Elser et al., 2016; ZhangSun  
44 et al., 2014; Ng2016a; Xu et al., 2011b; 2019; Zhao et al., 2019), cooking-related OA (COA) (XuMohr  
45 et al., 2019; Zhao2012; Crippa et al., 2013; 2013b; Hu et al., 2016; Sun et al., 2016a; Sun et al., 2016b;  
46 CrippaXu et al., 2013a; Mohr2019; Zhao et al., 2012; 2019), biomass burning OA (BBOA) (Alfarra et  
47 al., 2007; Lanz et al., 2007; Sun et al., 2011), and coal combustion OA (CCOA) (Zhang et al., 2008;  
48 Zhang et al., 2014; Elser et al., 2016; Hu et al., 2016; Sun et al., 2016a; Zhang et al., 2014; Zhang et al.,

1 2008). However, SOA is typically reported as either a single SOA factor (denoted oxygenated organic  
2 aerosol, OOA), or as two factors distinguished by degree of oxygenation (i.e., less oxygenated OOA,  
3 LO-OOA, and more oxygenated OOA, MO-OOA) or by volatility (i.e., semi-volatile OOA, SV-OOA,  
4 and low-volatility OOA, LV-OOA) (Xu et al., 2019; Elser et al., 2016; Sun et al., 2016a; Sun et al.,  
5 2013; Jimenez et al., 2009; Zhang et al., 2011; Crippa et al., 2013a; 2013b; Sun et al., 2013; Elser et al.,  
6 2016; Sun et al., 2016a; Xu et al., 2019) rather than in terms of sources and/or formation processes.  
7 This limitation is due to the vaporisation/ionisation scheme in the AMS, which causes significant  
8 thermal decomposition and ionisation-induced fragmentation (DeCarlo et al., 2006). The corresponding  
9 decrease in chemical resolution, particularly for the multifunctional and/or highly oxygenated SOA  
10 components molecules of which SOA is comprised (DeCarlo et al., 2006). The corresponding decrease  
11 in chemical resolution, particularly for multifunctional and/or highly oxygenated SOA components (e.g.,  
12 multifunctional acids, peroxides, organonitrates, organosulfates, oligomers), limits the resolution of  
13 SOA source apportionment.

14  
15 The development of continuous or semi-continuous instruments with softer vaporisation/ionisation  
16 schemes has provided new insights into SOA composition, and is thus of considerable interest for source  
17 apportionment. Recent examples include the (semi-continuous) Filter Inlet for Gases and AEROSols  
18 chemical ionisation time-of-flight mass spectrometer (FIGAERO-CIMS) (Lopez-Hilfiker et al.,  
19 2014) (Lopez-Hilfiker et al., 2014), and the (continuous) extractive electrospray ionisation time-of-flight  
20 mass spectrometer (EESI-TOF) (Lopez-Hilfiker et al., 2019), which implement soft ionisation schemes  
21 at lower temperatures than the AMS, thereby reducing thermal decomposition and increasing chemical  
22 resolution (i.e., providing chemical formulae of molecular ions). A recent source apportionment study  
23 using FIGAERO-CIMS at a rural site in the southeastern USA successfully resolved three SOA factors,  
24 characterised by isoprene-derived species such as carboxylic acids from aqueous phase processes,  
25 highlighting the chemistry of biogenic species (Chen et al., 2020). Source apportionment studies in  
26 Zurich using an EESI-TOF identified SOA factors from monoterpene oxidation in summer (Stefenelli  
27 et al., 2019) and oxidation of biomass burning emissions in winter (Qi et al., 2019). EESI-TOF  
28 measurements identified SOA factors related to solid fuel combustion and aqueous phase processes in  
29 Beijing (Tong et al., 2021) and SOA factors with aromatic and biogenic origins in Delhi (Kumar et al.,  
30 2021). However, to date the factor concentrations returned by PMF analyses using these instruments  
31 are not quantitative.

32  
33 Quantification of the measurements by instruments such as EESI-TOF and CIMS is challenging, which  
34 implement soft ionisation schemes at lower temperatures than the AMS, thereby reducing thermal  
35 decomposition and increasing chemical resolution (i.e., providing chemical formulae of molecular ions).  
36 A recent source apportionment study using a FIGAERO-CIMS at a rural site in the southeastern USA  
37 successfully resolved three SOA factors, characterised by isoprene-derived species such as carboxylic  
38 acids from aqueous phase processes, highlighting the chemistry of biogenic species (Chen et al., 2020).  
39 Another source apportionment study from Lee et al. (2020) using FIGAERO-CIMS spectra successfully  
40 distinguished ambient SOA formation and ageing pathways in two forested regions. Source  
41 apportionment studies in Zurich using an EESI-TOF identified SOA factors from monoterpene  
42 oxidation in summer (Stefenelli et al., 2019) and oxidation of biomass burning emissions in winter (Qi  
43 et al., 2019). EESI-TOF measurements identified SOA factors related to solid fuel combustion and  
44 aqueous-phase processes in Beijing (Tong et al., 2021) and SOA factors with aromatic and biogenic  
45 origins in Delhi (Kumar et al., 2021). However, to date the factor concentrations returned by PMF  
46 analyses using these instruments are not quantitative.

1 [Quantification of the measurements by instruments such as EESI-TOF and CIMS is challenging](#)  
2 because the instrument sensitivity varies strongly with molecular identity. For CIMS, the sensitivity to  
3 different compounds is determined by the frequency of collisions between reagent ions and analytes,  
4 the ion-molecule reaction time, and the transmission efficiency of product ions to the detector, which  
5 depends on ion-molecule binding energy. [Lopez-Hilfiker et al. \(2016\)](#)[Lopez-Hilfiker et al. \(2016\)](#)  
6 developed methods to estimate the binding energy of iodide ( $I^-$ ) adduct ions of multifunctional organic  
7 compounds for species whose formation is collision-limited, providing a lower limit to their mass  
8 concentrations. Another method to explore the sensitivity is to measure single-compound aerosols or  
9 SOA generated from different precursors simultaneously by an EESI-TOF and a scanning mobility  
10 particle sizer (SMPS) to determine the mass concentration ([Lopez-Hilfiker et al., 2016](#))([Lopez-Hilfiker](#)  
11 [et al., 2016](#)). Lopez-Hilfiker et al. (2019) explored EESI-TOF sensitivities to selected reference  
12 compounds with different functional groups (including saccharides, polyols and carboxylic acids) and  
13 bulk SOA generated from oxidation of a single precursor VOC. For pure compounds, relative  
14 sensitivities vary by two orders of magnitude, with some composition-dependent trends evident (e.g.,  
15 increasing sensitivity of saccharides with decreasing molecular weight, and high sensitivities for polyols  
16 relative to other functionalities). In addition, a trend of decreasing sensitivity with decreasing molecular  
17 weight of the precursors was found for bulk SOA. While calibration with standard compounds is  
18 straightforward, the quantification of individual species within SOA is extremely challenging, due to  
19 its complex composition, the lack of chemical standards for most molecules, and the potential for  
20 structural isomers to have significantly different sensitivities. These issues were investigated recently  
21 for the EESI-TOF by generating SOA in the presence of a variable seed surface area, and comparing  
22 the difference in SOA ion concentrations measured by the EESI-TOF and the corresponding gas-phase  
23 concentrations measured by a Vocus proton transfer reaction-mass spectrometer (Vocus-PTR-MS)  
24 ([Wang et al., 2021](#))([Wang et al., 2021](#)). The observed sensitivities for different SOA components  
25 produced from the oxidation of limonene, *o*-cresol, or 1,3,5-trimethylbenzene ranged from  $10^3$  to  $10^5$   
26  $\text{ion s}^{-1} \text{ppb}^{-1}$ . A regression model was developed that was able to predict the ion-by-ion sensitivities to  
27 within a factor of 5 of the experimental value when the precursor VOC is known *a priori*. However, the  
28 study also showed significantly different sensitivities (up to a factor of 20) for structural isomers derived  
29 from different VOC precursors. [Similar isomer sensitivity differences for I-CIMS was also reported by](#)  
30 [\(Bi et al., 2021\)](#)[Similar isomer sensitivity differences for the I-CIMS were also reported by \(Bi et al.,](#)  
31 [2021\)](#). The fact that these isomers cannot be distinguished by 1-dimensional mass spectrometry,  
32 represents a fundamental limitation of calibration/parameterisation-based quantification and  
33 complicates interpretation of the binding energy-based approach (Lopez-Hilfiker et al., 2016), because  
34 ambient SOA may derive from unknown or complex mixtures of VOCs. Therefore, for source  
35 apportionment purposes, source-based sensitivities are preferred and essential to quantify SOA sources  
36 and formation processes.

37  
38 Here we present a new approach for quantification of SOA sources retrieved from source apportionment.  
39 This is achieved by PMF analysis of a single input matrix consisting of data from both a quantitative  
40 instrument with lower chemical resolution (i.e., AMS) and an instrument with high chemical resolution  
41 and a linear but molecule-dependent response (i.e., EESI-TOF). This method is based on the combined  
42 PMF (cPMF) analysis previously performed on combined OA/VOC data from AMS and PTR-MS,  
43 respectively ([Crippa et al., 2013b](#); Slowik et al., 2010; [Crippa et al., 2013a](#)), but utilises a more robust  
44 metric for ensuring adequate representation of both instruments in the model solution, optionally allows  
45 constraints to be placed on the factor profile contributions for one or both instruments, and provides a  
46 method for uncertainty analysis. The cPMF method is applied to AMS/EESI-TOF datasets collected  
47 during summer and winter campaigns in Zurich, Switzerland, for which single-instrument PMF  
48 analyses were previously reported (Qi et al., 2019; Stefenelli et al., 2019). The present study is the first

1 application of cPMF to a joint EESI-TOF/AMS dataset, and the first ~~attempt at~~ quantitative EESI-TOF-  
2 driven source apportionment.

## 3 4 **2. Methodologies**

### 5 **2.1 The measurement site and field campaigns**

6 Field campaigns were conducted at the Swiss National Air Pollution Monitoring Network (NABEL)  
7 station, an urban background site located in the Alte Kaserne, central Zurich (47°22' N, 8°33' E, 410 m  
8 above sea level), previously described in detail (Lanz et al., 2007; Canonaco et al., 2013; Lanz et al.,  
9 2007). The measurements used in the current analysis are from 20 June to 26 June 2016 and 25 January  
10 to 4 February 2017. These periods are excerpted from longer campaigns, and correspond to the times  
11 during which both the AMS and EESI-TOF achieved stable operation. The measurement site is located  
12 in a courtyard, although influences from nearby restaurants, local minor roads, and human activities  
13 (e.g., cigarette smoking) are often observed (Lanz et al., 2007; Daellenbach et al., 2017; Qi et al., 2019;  
14 Stefenelli et al., 2019; Qi et al., 2019; Qi et al., 2020). Gas-phase species, e.g., nitrogen dioxide (NO<sub>2</sub>),  
15 nitrogen oxide (NO) and sulfur dioxide (SO<sub>2</sub>) and meteorological data, e.g., temperature (T), relative  
16 humidity (RH), radiation, wind speed (~~WDWS~~) and wind direction (WD) are recorded by the  
17 monitoring station.

18  
19 During the intensive campaigns, a separate trailer was deployed to house an additional suite of gas and  
20 particle instrumentation. A PM<sub>2.5</sub> cyclone was installed ~75 cm above the trailer roof (~5 m above  
21 ground) to remove coarse particles. After passing through the cyclone, the sampled air passed through  
22 a stainless steel (~6 mm outer diameter, O.D.) tube to the particle instrumentation, which included a  
23 high-resolution time-of-flight aerosol mass spectrometer (HR-TOF-AMS, Aerodyne Research Inc.) and  
24 an extractive electrospray ionisation time-of-flight mass spectrometer (EESI-TOF) to measure the OA  
25 composition, and a scanning mobility particle sizer (SMPS) to measure the particle concentration and  
26 size distribution. The summer and winter campaign results, including OA source apportionment from  
27 the standalone AMS and EESI-TOF datasets, were previously presented in detail (Qi et al., 2019;  
28 Stefenelli et al., 2019). In this study, we focus on the OA source apportionment using positive matrix  
29 factorisation (PMF) on the combined dataset from AMS and EESI-TOF, collected during the two  
30 campaigns.

### 31 32 **2.2 Instrumentation**

#### 33 **2.2.1 High-resolution time-of-flight aerosol mass spectrometer (HR-TOF-AMS)**

34  
35 The AMS (Aerodyne Research, Inc.) provides fast, online, quantitative measurements of the size-  
36 resolved composition of non-refractory PM<sub>1</sub> (NR-PM<sub>1</sub>). A detailed description of the instrument can be  
37 found elsewhere (DecarloDeCarlo et al., 2006; Canagaratna et al., 2007), ~~while operational details and~~  
38 ~~data treatment are documented in Stefenelli et al. (2019) and~~, ~~while operational details and data~~  
39 ~~treatment are documented in Stefenelli et al. (2019) and~~ Qi et al. (2019). Briefly, in both campaigns,  
40 the organic composition of NR-PM<sub>1</sub> was measured by AMS with a time resolution of 1 min. At the  
41 beginning and ~~at the~~ end of the both campaigns, the instrument was calibrated for ionisation efficiency  
42 (IE) using 400 nm NH<sub>4</sub>NO<sub>3</sub> particles ~~by using~~ the mass-based method (Jimenez et al., 2003; Canagaratna  
43 et al., 2007; Jimenez et al., 2003). The HR-TOF-AMS data was analysed using the SQUIRREL (v.1.57)  
44 and PIKA (v.1.16) software packages in IGOR Pro 6.37 (Wavemetrics, Inc., Portland, OR, USA).  
45 Before further single-instrument and cPMF analysis, a composition-dependent collection efficiency  
46 (CDCE) was implemented to correct the measured aerosol mass (Middlebrook et al., 2012). ~~For both~~  
47 ~~single instrument PMF and cPMF analysis, the input matrices consisted of the time series of fitted OA~~  
48 ~~ions from high-resolution mass spectral analysis, together with their corresponding uncertainties~~

1 ~~estimated from ion counting statistics and detector variability according to Allan et al. (2003).~~  
2 ~~Following Ulbrich et al. (2009), a minimum error value was applied to the error matrix. For both~~  
3 ~~single-instrument PMF and cPMF analysis, the input matrices consisted of the time series of fitted OA~~  
4 ~~ions from high-resolution mass spectral analysis, together with their corresponding uncertainties~~  
5 ~~estimated from ion counting statistics and detector variability according to Allan et al. (2003).~~  
6 ~~Following Ulbrich et al. (2009), a minimum error value was applied to the error matrix. Ions with signal-~~  
7 ~~to-noise ratio (SNR) smaller than 0.2 were excluded in the further analysis, whereas ions with an SNR~~  
8 ~~between 0.2 and 2 were downweighted by a factor of 2 (Paatero and Hopke, 2003). The contribution of~~  
9 ~~nitrate ions to CO<sub>2</sub><sup>+</sup> was estimated separately in each campaign from their respective NH<sub>4</sub>NO<sub>3</sub>~~  
10 ~~calibrations (Pieber et al., 2016).~~

11  
12 The AMS PMF input matrices are identical to those used by ~~Stefenelli et al. (2019)~~Stefenelli et al. (2019)  
13 and Qi et al. (2019), with the exception that they include not only the OA ions retrieved from spectral  
14 analysis, but also NO<sup>+</sup> and NO<sub>2</sub><sup>+</sup>. These ions are added because they represent the major products  
15 measured from organonitrate fragmentation (~~Farmer et al., 2010~~Farmer et al., 2010), and standalone  
16 EESI-TOF PMF suggested a significant role for organonitrates and other nitrogen-containing species  
17 during both the summer and winter campaigns (Qi et al., 2019; Stefenelli et al., 2019). Detailed  
18 descriptions of the final input matrices from AMS (e.g., number of measurements, number of ions and  
19 time resolution) in summer and in winter are presented in Table 1.

#### 20 21 2.2.2 Extractive electrospray ionisation time-of-flight mass spectrometer (EESI-TOF)

22  
23 The EESI-TOF provides online, fast, near-molecular-level measurement (i.e., chemical formulae of  
24 molecular ions) of OA composition, without thermal decomposition or ionisation-induced  
25 fragmentation. A detailed description can be found elsewhere (Lopez-Hilfiker et al., 2019) and the  
26 operational details for the summer and winter campaigns are documented in ~~Stefenelli et al.~~  
27 ~~(2019)~~Stefenelli et al. (2019) and Qi et al. (2019), respectively. Briefly, aerosol particles were  
28 continuously sampled through a 6 mm O.D., 5 cm long multi-channel extruded carbon denuder.  
29 Particles then intersected a spray of charged droplets generated by a conventional electrospray probe  
30 and the soluble fraction was extracted into the droplets. The droplets passed through a heated stainless-  
31 steel capillary (~250 °C), wherein the electrospray solvent evaporated, and ions were ejected into the  
32 mass spectrometer. Due to the short residence time (~1 ms) in the capillary, no thermal decomposition  
33 was observed. The analyte ions were detected by a high-resolution time-of-flight mass spectrometer  
34 with an atmospheric pressure interface (API-TOF) (~~Junninen et al., 2010~~Junninen et al., 2010). In the  
35 summer campaign, the electrospray consisted of a 1:1 water/methanol (MeOH, UHPLC-MS grade,  
36 LiChrosolv) mixture doped with 100 ppm NaI (>99 %, Sigma-Aldrich). In the winter campaign, a 1:1  
37 water/acetonitrile mixture (> 99.9 %, Sigma-Aldrich) mixture with 100 ppm NaI (99 %, Sigma-Aldrich)  
38 was utilised, which reduced background signal. In both campaigns, the mass spectrometer was  
39 configured to detect positive ions. Because of NaI use, analyte ions were detected almost exclusively  
40 as [M]Na<sup>+</sup> and other ionisation pathways were suppressed (the only notable exception being nicotine,  
41 which was detected as [C<sub>10</sub>H<sub>14</sub>N<sub>2</sub>]H<sup>+</sup>). This yields a linear response to mass, avoids matrix effects, and  
42 simplifies spectral interpretation (Lopez-Hilfiker et al., 2019). Adducts of an analyte with acetonitrile  
43 or methanol molecule(s) may also be detected by the instrument, depending on the voltage settings in  
44 the ion transfer optics (i.e., collision energy), but these adducts were observed to have negligible signals  
45 with our voltage configurations in both campaigns. ~~The EESI-TOF alternates between direct sampling~~  
46 ~~(8 min) and sampling through a particle filter (3 min) to provide a measurement of instrument~~  
47 ~~background (including spray). No major changes between adjacent background measurements were~~  
48 ~~observed in either campaign (Qi et al., 2019; Stefenelli et al., 2019).~~

Formatted: English (United States)

Formatted: English (United States)

Formatted: English (United States)



1  
2 Data analysis, including high-resolution peak fitting, was performed using Tofware version 2.5.7  
3 (Tofwerk AG, Thun, Switzerland). Detailed data treatment processes can be found in [Stefenelli et al.](#)  
4 [\(2019\)](#)[Stefenelli et al. \(2019\)](#) and Qi et al. (2019). The EESI-TOF alternates between periods of direct  
5 ambient sampling ( $M_{amb}$ ) and filter sampling ( $M_{bkgd}$ ), with the filter periods interpolated to yield an  
6 estimated background spectrum during ambient measurements ( $M_{bkgd,est}$ ). The spectra corresponding to  
7 aerosol composition ( $M_{diff}$ ) are determined by the difference of  $M_{amb}$  and  $M_{bkgd,est}$  as shown in Eq. (1a).  
8 The corresponding error matrix was estimated by adding in quadrature the uncertainties of the total  
9 sampling measurement  $s_{amb}(i,j)$  and the filter sampling measurement  $s_{bkgd,est}(i,j)$  as shown in Eq. (1b),  
10 which are in turn calculated from ion counting statistics and detector variability ([Allan et al.](#),  
11 [2003](#))([Allan et al., 2003](#)):

$$12 \quad M_{diff}(i,j) = M_{amb}(i,j) - M_{bkgd,est}(i,j) \quad (1a)$$

$$13 \quad s_{diff}(i,j) = \sqrt{s_{amb}^2(i,j) + s_{bkgd,est}^2(i,j)} \quad (1b)$$

14  
15 where the unit of all quantities in both equations is counts per second (cps). Ions with a mean SNR  
16 smaller than 2 were removed from both matrices, because the signals of these ions were predominantly  
17 caused by electrospray and/or instrumental background. Input matrix dimensions are summarised in  
18 Table 1.

19  
20 In theory, EESI-TOF signal for an ion  $x$  can be converted from ion flux (cps) to mass concentration  
21 ( $\mu\text{g m}^{-3}$ ), according to Eq. (2):

$$22 \quad Mass_x = I_x \cdot \frac{MW_x}{EE_x + CE_x + IE_x + TE_{m/z}} \cdot \frac{1}{F} \quad (2)$$

23  
24 where  $Mass_x$  and  $I_x$  are the mass concentration (in  $\mu\text{g m}^{-3}$ ), and the ion flux (cps) reaching the detector  
25 for an ion  $x$ , respectively.  $MW_x$  represents the molecular weight of the measured ion (e.g.,  $[M]Na^+$ )  
26 (Lopez-Hilfiker et al., 2019; Qi et al., 2019; Stefenelli et al., 2019).  $EE_x$ ,  $CE_x$ ,  $IE_x$  and  $TE_{m/z}$  denote  
27 EESI extraction efficiency (the probability that a molecule dissolves in the spray), EESI collection  
28 efficiency (the probability that the analyte-laden droplet enters the inlet capillary), ionisation efficiency  
29 (the probability that an ion forms and subsequently survives declustering forces induced by evaporation  
30 and electric fields), and ion transmission efficiency (the probability that a generated ion is transmitted  
31 to the detector, which is independent from chemical identity but depends only on  $m/z$ ), respectively.  $F$   
32 indicates the flow rate. In practice, several of these parameters are ion-dependent and remain  
33 uncharacterised, and therefore conversion to mass concentration on an ion-by-ion basis cannot currently  
34 be achieved (Lopez-Hilfiker et al., 2019). Instead, to facilitate comparison with bulk quantities, we  
35 define an "apparent sensitivity ( $AS$ )" to describe the EESI-TOF response to a measured concentration  
36 of species  $x$ , as shown in Eq. (3):

$$37 \quad AS_x = \frac{MW_x}{EE_x \cdot CE_x \cdot IE_x \cdot TE_{m/z}} \cdot \frac{1}{F} = \frac{I_x}{Mass_x} \quad (3)$$

38 where  $I_x$  is the measured ion flux (counts per second, cps) for the ion or factor  $x$  detected by EESI-TOF,  
39  $Mass_x$  is measured mass concentration ( $\mu\text{g m}^{-3}$ ) from a reference instrument for the same ion or factor  
40  $x$ , thus the  $AS$  is in the unit of cps ( $\mu\text{g m}^{-3}$ )<sup>-1</sup>. ~~In this study, we calculated Equation (3) is used to determine~~  
41 ~~the apparent factor-specific sensitivities for different factors from the cPMF results/outputs by~~  
42 ~~utilising/defining the AMS contribution to the factor profile ( $\mu\text{g m}^{-3}$ ) as  $Mass_x$  and the EESI-TOF~~  
43 ~~contribution (cps) as  $I_x$ . Calculation of these contributions is discussed later in in Sect. 4 using these~~  
~~factor dependent sensitivities.~~

### 2.2.3 Estimation of EESI-TOF sensitivities from a multi-variate model

For comparison to the factor-dependent sensitivities determined by the cPMF analysis (see Sect. 3, Eq. 3), we also estimated sensitivities for SOA factors from molecular formulae of individual analyte ions using parameterisations developed from laboratory measurements of SOA generated from oxidation of limonene (LMN) by ozone and *o*-cresol (cresol) and 1,3,5-trimethylbenzene (TMB) by OH radicals (Wang et al., 2021). As discussed in Sect. 1, (Wang et al., 2021). As discussed in Sect. 1, the parameterisation can predict the relative sensitivities of ions measured by the EESI-TOF to within a factor of 5, provided that the SOA is derived from a single, known VOC. However, for ambient data, SOA derives from multiple precursor VOCs, increasing uncertainties. For example, SOA isomers generated from different precursors can differ by up to a factor of 20 in relative sensitivity (Wang et al., 2021). (Wang et al., 2021). This represents a significant source of uncertainty for calibration/parameterisation-based approaches for quantifying SOA factors from source apportionment, but is nonetheless a useful point of comparison.

In the present study, we utilise two well-performing models from Wang et al. (2021), namely the gradient-boosting regression and linear ridge regression models, denoted GBR and LRR, respectively. In the present study, we utilise a well-performing model from Wang et al. (2021), namely the gradient-boosting regression, denoted GBR, developed in scikit-learn packages in Spyder 4.1.4 and Python 3.8.3. The SOA parameterisation derived from LMN was used to predict the sensitivities for summer SOAs (which are predominantly terpene-derived SOAs), and SOA systems derived from cresol and TMB were used to predict the sensitivities for winter SOAs (which are characterised by aromatics from biomass burning activities). The regression models provide compound-dependent relative sensitivities ( $AS_x$ ) based only on molecular formulae. Then, the EESI-TOF signals for each factor are calculated as a signal-weighted average from the respective factor profiles, as shown in Eq. (4):

$$AS_{factor} = \frac{\sum_x I_x}{\sum_x (I_x / AS_x)} \quad (4)$$

Here  $I_x$  denotes the contribution to the factor profile of each ion  $x$ . Because the model parameterisations are based on laboratory SOA that contained only the CHO group, while the resolved OA sources in this study include both CHO and CHON, we approximate the total factor sensitivity by assuming the average EESI-TOF sensitivity to CHON ions is equal to the average sensitivity of CHO ions (on a factor-by-factor basis). Note that the ions from the CHO group contribute a major fraction in SOA mass for each factor, comprising 85.2 %, 78.1 %, 57.3 % and 76.3 % for DaySOA1, DaySOA2, NightSOA1 and NightSOA2 for summer and 77.9 % and 75.0 % to SOA1 and SOA2 for winter, reducing the uncertainties introduced by this assumption (these factors will be discussed in Sect. 3.2). The factor-specific sensitivities derived from cPMF (Eq. 3) and from the GBR model (Eq. 4) are compared in Sect. 3.2.

### 2.3 Source Apportionment Combined Positive Matrix Factorisation (cPMF) Method

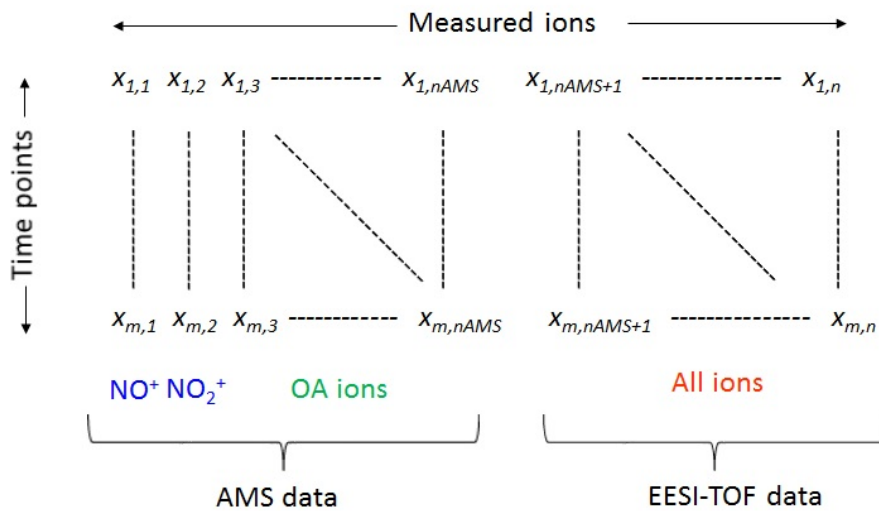
In this paper, the source apportionment was performed using the model used in this study is based on positive matrix factorisation (PMF) model on, which is widely used in the environmental studies. PMF is a bilinear receptor factor analysis model that decomposes time series of measured variables (here related to particle composition) into factor contributions and factor profiles. Different from

Formatted: English (United Kingdom)

Formatted: English (United States)



1 conventional PMF analysis, which is typically conducted on a dataset collected by a single instrument,  
 2 here PMF is applied to a single input dataset containing both AMS and EESI-TOF mass spectral data.  
 3 We A conceptual schematic of the input data matrix is shown in Fig. 1. Herein we denote the overall  
 4 method governing analysis of such a merged dataset as “combined PMF” (cPMF), while “PMF” denotes  
 5 both the general PMF model and single-run executions by the Multilinear Engine solver (see Sect.  
 6 2.3.1), 2.3.0), which are identical for PMF and cPMF.  
 7



8  
 9 **Figure 1.** Schematic of the combined EESI-TOF and AMS input data matrix ( $X$ ) for cPMF. Matrix  
 10 dimensions for the summer and winter datasets are provided in Table 1.  
 11

12 This section presents an overview of the cPMF method, with detailed descriptions of each step in the  
 13 referenced sub-sections. Section 3.1 then presents In the Text S2 in the Supplement, we present details  
 14 of its application to the test datasets, including dataset-specific decisions (e.g., which factors to constrain,  
 15 criteria for accepting/rejecting solutions) required during certain steps. The overall procedure is outlined  
 16 in Fig. 4, 2, with the main steps as follows:

- 17 1) Conventional PMF analyses are conducted on the standalone EESI-TOF and AMS  
 18 datasets with synchronised time resolution, including constraints on factor profiles as necessary.  
 19 Residuals Residual distributions from the optimised solutions are used later in step 3 as a  
 20 reference to retrieve a balanced solution (step 4) criterion for assessing relative instrument  
 21 weight.
- 22 2) The EESI-TOF and AMS datasets with synchronised time resolution are combined into  
 23 a single input matrix. This input matrix contains OA spectra from EESI-TOF and AMS, as well  
 24 as the  $\text{NO}^+$  and  $\text{NO}_2^+$  ions measured by the AMS due to the contributions of organonitrates to  
 25 these ions (Sect. 2.3.1).
- 26 3) For any factors that are to be constrained, joint AMS/EESI-TOF profiles are  
 27 constructed (Sect. 2.3.2 and 3, 2.3.2 and Text S2.2).
- 28 4) An exploratory PMF analysis is conducted on the joint AMS/EESI-TOF matrix. This  
 29 consists of a 2-D exploration of the solution space defined by the number of factors ( $p$ ) and  
 30 relative instrument weight ( $C$ ) (Sect. 2.3.3) 2.3.3). The instrument weight ensures that both  
 31 instruments are well-represented in the solution and is assessed by comparing residuals from  
 32

- Formatted: Font: Times New Roman, English (United Kingdom)
- Formatted: Normal, Justified, Level 1, Don't add space between paragraphs of the same style
- Formatted: Font: Times New Roman, English (United Kingdom)
- Formatted: Font: Times New Roman, Not Bold, English (United Kingdom)
- Formatted: English (United Kingdom)
- Formatted: Paper\_Normal, Left
- Formatted: Numbered + Level: 1 + Numbering Style: 1, 2, 3, ... + Start at: 0 + Alignment: Left + Aligned at: 0.63 cm + Indent at: 1.27 cm

Field Code Changed

cPMF and standalone PMF. For computational efficiency, the profiles of all constrained factors are not allowed to deviate from their reference profiles. Solutions in which both instruments receive approximately equal weight are evaluated for environmental interpretability, with the most interpretable solution utilised as the base case for further analysis. Note that the base case is fully defined by  $C$ ,  $p$ , and the set of constrained factor profiles.

5)4) From the selected base case, 1000 PMF runs are conducted, which combine bootstrap analysis with random selection of  $\alpha$ -values (i.e., tightness of constraint) for the constrained factors within predetermined limits that are defined on a factor-by-factor basis (Sect. 2.3.4).2.3.4). This requires the following as prerequisites:

- a. Definition of dataset-specific criteria for acceptance/rejection of individual runs (Sect. 3.4Text S2.4).
- b. Determination of the  $\alpha$ -value range on a factor-by-factor basis giving a reasonable acceptance probability, i.e., sufficient rejection rate to ensure adequate exploration while maintaining computational efficiency (Sect. 3.4Text S2.4).

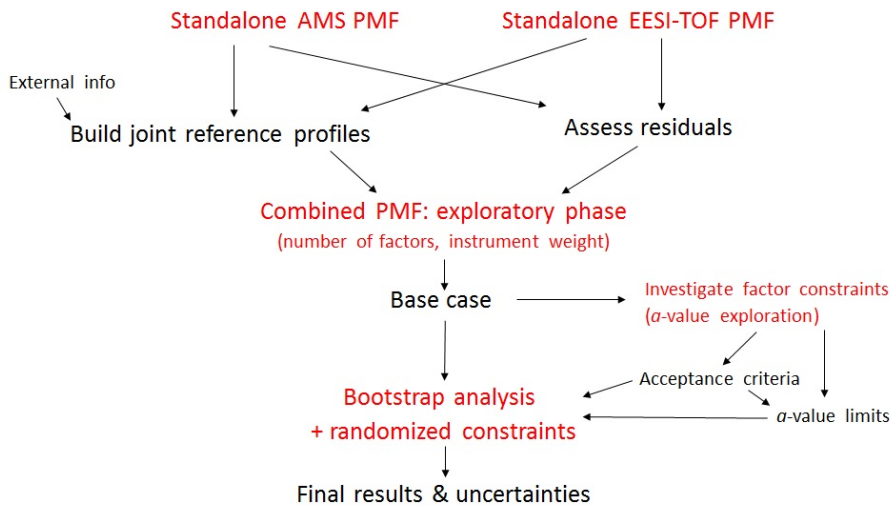
6) The final cPMF result is taken as the mean of all accepted solutions from the bootstrap/ $\alpha$ -value analysis (step 5), with uncertainties represented by the standard deviation. From this mean solution, quantitative time series and EESI-TOF factor-specific sensitivities are calculated.

Formatted: Numbered + Level: 2 + Numbering Style: a, b, c, ... + Start at: 1 + Alignment: Left + Aligned at: 1.9 cm + Indent at: 2.54 cm

Formatted: Font: 11 pt, English (United States)

Formatted: List Paragraph, Add space between paragraphs of the same style, No bullets or numbering

Formatted: Font: 11 pt, English (United States)



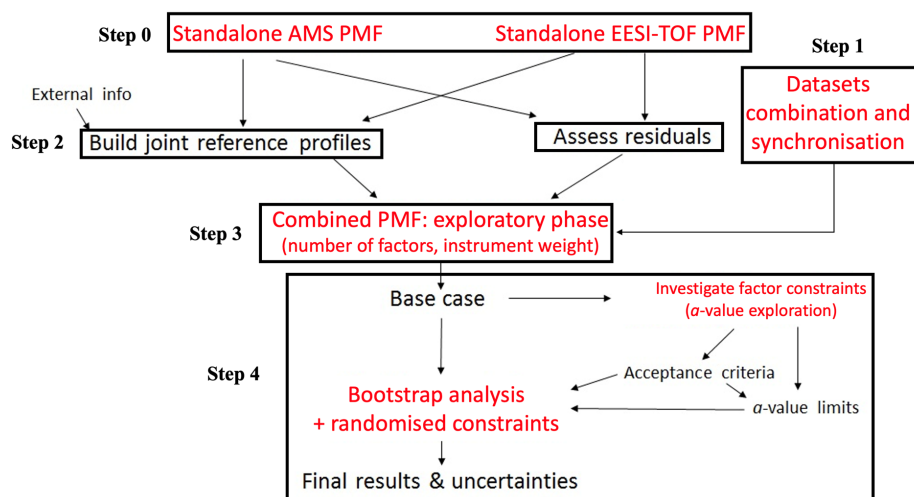


Figure 2. Flow chart summary of cPMF analysis workflow. Red text denotes PMF model operations while black text denotes inputs, outputs, and/or analysis decisions.

### 2.3.12.3.0 Positive matrix factorisation (PMF) principles

In this step, PMF analyses are conducted on the standalone EESI-TOF and AMS datasets with synchronised time resolution, including constraints on factor profiles as necessary. Residuals from these solutions are used to derive as a reference quantity to retrieve a balanced solution (procedure described in step 3). This step is a parallel step and a preparation for the cPMF, therefore, we denote this step as step 0.

Positive matrix factorisation (PMF) is implemented using the Multilinear Engine (ME-2) (Paatero, 1999)(Paatero, 1999), with model configuration and post-analysis performed with the Source Finder (SoFi, version 6B) (Canonaco et al., 2013), programmed in Igor Pro 6.39 (Wavemetrics, Inc.). PMF is a bilinear receptor model, which operates on an input data matrix  $\mathbf{X}$  (here the mass spectral time series collected by EESI-TOF and/or AMS) and uncertainty matrix  $\mathbf{S}$ , which corresponds point-by-point to  $\mathbf{X}$ . PMF describes  $\mathbf{X}$  as a linear combination of static factor profiles (in this case characteristic mass spectra, representing specific sources and/or atmospheric processes) and their corresponding time-dependent source contributions, as described in Eq. (5):

$$\mathbf{X} = \mathbf{G} \times \mathbf{F} + \mathbf{E} \quad (5)$$

Here  $\mathbf{X}$  has dimensions of  $m \times n$ , representing  $m$  measurements of  $n$  variables (here ions),  $\mathbf{G}$  and  $\mathbf{F}$  are respectively the factor time series with the dimension of  $m \times p$ , and factor profiles with the dimension of  $p \times n$ , where  $p$  is the number of factors in the PMF solution, and is determined by the user.  $\mathbf{E}$  is the residual matrix and defined by Eq. (5). Figure 2 shows a conceptual representation of the combined EESI-TOF and AMS input data matrix  $\mathbf{X}$ . The corresponding uncertainty matrix  $\mathbf{S}$  and residual matrix  $\mathbf{E}$  are constructed in the same way (Slowik et al., 2010)(Slowik et al., 2010). Note that the AMS component of  $\mathbf{X}$ ,  $\mathbf{S}$  and  $\mathbf{E}$  is in  $\mu\text{g m}^{-3}$ , and the EESI-TOF component is in cps. Also,  $\mathbf{X}$  includes not only organic ions from the AMS, but also  $\text{NO}^+$  and  $\text{NO}_2^+$ , which contain a large fraction of the AMS signal derived from organonitrates (Farmer et al., 2010)(Farmer et al., 2010).

Formatted: English (United States)

Formatted: English (United States)

Formatted: Paper\_Normal, Left, None, Add space between paragraphs of the same style

Formatted: German (Switzerland)

Formatted: English (United States)

Formatted: Outline numbered + Level: 3 + Numbering Style: 1, 2, 3, ... + Start at: 1 + Alignment: Left + Aligned at: 1.9 cm + Indent at: 3.17 cm

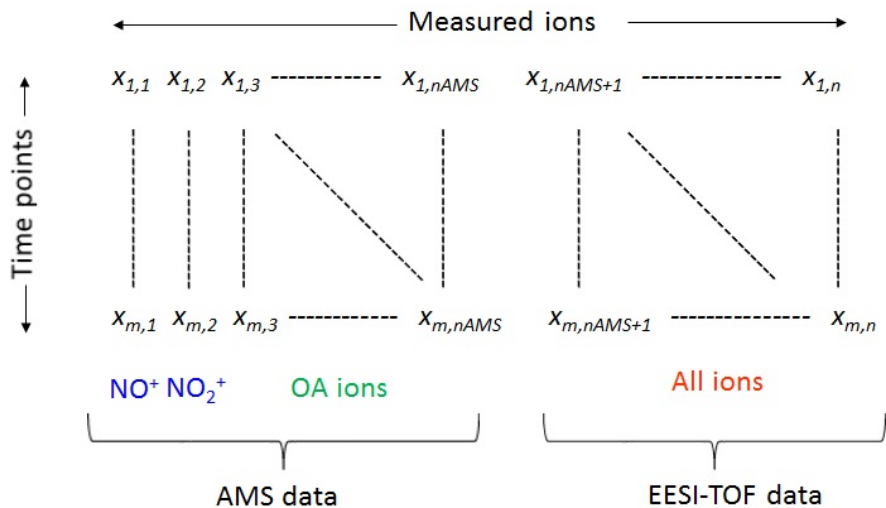


Figure 2. Schematic of the combined EESI-TOF and AMS input data matrix ( $X$ ) for cPMF. Matrix dimensions for the summer and winter datasets are provided in Table 1.

Equation (5) is solved by a least-squares algorithm that iteratively minimises the quantity  $Q$ , which is defined in Eq. (6) as the sum of the squares of the uncertainty-weighted residuals:

$$Q = \sum_i \sum_j \left( \frac{e_{ij}}{s_{ij}} \right)^2 \quad (6)$$

Here  $e_{ij}$  is an element in the residual matrix  $E$ , and  $s_{ij}$  is the corresponding element in the uncertainty matrix, where  $i$  and  $j$  are the indices representing time and ion (or  $m/z$ ), respectively. The theoretical  $Q$ , denoted as  $Q_{\text{expected}}$ , is estimated by Eq. (7):

$$(f_{k,j})_{\text{sol}} = (f_{k,j})_{\text{ref}} \pm a \times (f_{k,j})_{\text{ref}} \quad (7)$$

Here  $(f_{k,j})_{\text{ref}}$  represents the reference profile and  $(f_{k,j})_{\text{sol}}$  the final profile returned by the model. Due to the renormalisation of matrices after PMF runs, the final values in  $(f_{k,j})_{\text{sol}}$  may slightly exceed the prescribed range. This approach has been shown to significantly improve the model performance relative to unconstrained PMF

$$Q_{\text{expected}} \approx mn - p(m+n) \quad (7)$$

Formatted: Font: Times New Roman, English (United Kingdom)

Formatted: Normal, Justified, Level 1, Don't add space between paragraphs of the same style

Formatted: Font: Times New Roman, Not Bold, English (United Kingdom)

Formatted: Font: Times New Roman, English (United Kingdom)

Formatted: English (United Kingdom)

Formatted: English (United States)

1 where  $m$  and  $n$  denote the number of measurements (here time points) and the number of variables (ions  
2 or  $m/z$ ), respectively, and  $p$  denotes the number of factors in this PMF solution.

3  
4 [\(Canonaco et al., 2013; Crippa et al., 2014; Daellenbach et al., 2016; Qi et al., 2019; Stefenelli et al.,  
5 2019\)](#).

6  
7 Due to the nature of the cPMF  $X$  matrix, each retrieved factor has a single time series, which can be  
8 expressed in the concentration units of either instrument, and the factor profile contains both an AMS  
9 and an EESI-TOF component. The factor time series for a single factor  $k$  is calculated as follows:

$$(g_{i,k})_{inst} = g_{i,k} \cdot \sum_{j=inst} f_{k,j} \quad (8)$$

10  
11 Here  $(g_{i,k})_{inst}$  refers generally to the time series in the measurement units of a given instrument, which  
12 we denote  $(g_{i,k})_{AMS}$  or  $(g_{i,k})_{EESI}$ , and the  $j=inst$  formalism denotes the set of ions measured by the  
13 respective instrument. For ease of interpretation, we report the instrument contribution to each factor  
14 profile as the mass spectrum (in the respective instrument units) that would be obtained for a factor  
15 mass concentration of  $1 \mu\text{g m}^{-3}$ . This is expressed as follows, for a single factor  $k$ :

$$(f_{k,j})_{inst} = \left( \frac{f_{k,j}(\overline{g_{i,k}})_{AMS}}{g_0} \right)_{j=inst} \quad (9)$$

16  
17  
18 Here  $\overline{(g_{i,k})_{AMS}}$  denotes the mean of the factor time series in AMS units ( $\mu\text{g m}^{-3}$ ),  $g_0$  is a reference mass  
19 concentration (chosen here as  $1 \mu\text{g m}^{-3}$ ), the  $j=inst$  formulation again refers to all ions measured by a  
20 given instrument. We refer to the organic fraction of AMS profile components and EESI-TOF profile  
21 components as  $(f_{k,j})_{AMS}$  and  $(f_{k,j})_{EESI}$ , respectively. The EESI-TOF apparent sensitivity ( $AS_k$ ,  
22 defined in Eq. [\(3\)](#)) can then be calculated for a single factor  $k$  as:

$$AS_k = \left( \frac{(\overline{g_{i,k}})_{EESI}}{(\overline{g_{i,k}})_{AMS}} \right)_{j=inst} \quad (10)$$

23  
24  
25  
26 Evaluation of factor interpretability for PMF analysis of the data from a single instrument typically  
27 includes: 1) correlation of the time series with external data; 2) comparison of factor diurnal cycles with  
28 known source activity and previous measurements; 3) identification of source-specific spectral features.  
29 In addition to these three points, factors from cPMF were also interpreted by considering the consistency  
30 of spectral features between the AMS and EESI-TOF, e.g., factors originated from fresh biomass  
31 burning activities are characterised by elevated signal from  $\text{C}_2\text{H}_4\text{O}_2^+$  in the AMS spectrum and  
32 levoglucosan in the EESI-TOF spectrum.

### 33 34 [2.3.1 Dataset combination and synchronisation](#)

35  
36 [In this step, the time resolution of the EESI-TOF and AMS are synchronised and the datasets with  
37 overlap temporal coverage are combined into a single input matrix, as shown in Fig. 1. This input matrix  
38 contains OA spectra from EESI-TOF and AMS, as well as the  \$\text{NO}^+\$  and  \$\text{NO}\_2^+\$  ions measured by the  
39 AMS due to the contributions of organonitrates to these ions. The corresponding error matrix is also  
40 constructed in the same way.](#)

## 2.3.2 Constraints on factor profiles

Different combinations of the G and F matrices may result in solutions with the same or similar Q (rotational ambiguity), which in practice leads to mixed or unresolvable factors. Here we explore a subset of the possible PMF/cPMF solutions in which one or more factor profiles are constrained using the a-value approach to direct solutions towards environmentally meaningful rotations. These factors are constrained using reference profiles, with the scalar  $\alpha$  ( $0 \leq \alpha \leq 1$ ) determining the tightness of constraint as follows:

$$(f_{k,j})_{sol} = (f_{k,j})_{ref} \pm \alpha \times (f_{k,j})_{ref} \quad (11)$$

Here  $(f_{k,j})_{ref}$  represents the reference profile and  $(f_{k,j})_{sol}$  the final profile returned by the model. Due to the renormalisation of matrices after PMF runs, the final values in  $(f_{k,j})_{sol}$  may slightly exceed the prescribed range. This approach has been shown to significantly improve the model performance relative to unconstrained PMF (Crippa et al., 2014; Canonaco et al., 2013; Daellenbach et al., 2016; Stefanelli et al., 2019; Qi et al., 2019).

As shown in Eqs. (8-10), the EESI-TOF factor sensitivity is intrinsic to a given factor (via its profile). However, in

if one or more factors are constrained in the Sect. 2.3.0, these factors should also be constrained in this step, in which the principle of a-value approach in Eq. (7) applies here too. In the cPMF, it may be desirable to constrain a factor for which a single reference profile incorporating both AMS and EESI-TOF mass spectra is not available. For example, a factor may be detectable by only one instrument, or reference profiles may have been retrieved independently for each instrument (e.g., from different studies). In such cases, the cPMF reference profile,  $(f_{k,j})_{j=all,ref}$  is constructed from merged individual profiles as follows:

$$(f_{k,j})_{j=all,ref} = \begin{cases} \frac{(f_{k,j})_j}{\sum_j (f_{k,j})_j}, & j \in AMS,ref \\ AS_k \cdot \frac{(f_{k,j})_j}{\sum_j (f_{k,j})_j}, & j \in EESI,ref \end{cases} \quad (12)$$

$$\frac{(f_{k,j})_{j=all,ref}}{1 \mu\text{g m}^{-3}} = \begin{cases} \frac{(f_{k,j})_j}{\sum_j (f_{k,j})_j}, \\ AS_k \cdot \frac{(f_{k,j})_j}{\sum_j (f_{k,j})_j}, \end{cases}$$

Here  $(f_{k,j})_j$  denotes standalone reference profiles for the AMS and EESI-TOF, respectively. Note that although Eq. (12) requires an initial value of  $AS_k$  to be assumed prior to PMF execution and utilised during the exploratory phase of cPMF (Sect. 2.3.2.3, step 43), selection of a non-zero  $a$ -value during bootstrap analysis (Sect. 2.3.2.3, step 54) allows the final  $AS_k$  to be determined by the algorithm within the designated boundaries. Therefore, only a reasonable *a priori* estimate is required. In the case that a factor is undetectable by the EESI-TOF (e.g., non-oxygenated hydrocarbons comprising traffic-related factors), a value of  $AS_k$  is assumed that fixes the EESI-TOF contribution near zero, as discussed in the Supplement in Text S1. In the present study, we utilised  $AS_k = 0.01 \text{ cps } (\mu\text{g m}^{-3})^{-1}$  when this situation arose (e.g., HOA and InorgNit reference profiles are constructed using this method). For contrast,  $AS_k$  for factors detectable by both instruments ranged from approximately 100 to 1000 cps  $(\mu\text{g m}^{-3})^{-1}$ .

### 2.3.3 Instrument weighting

#### 2.3.3 Exploratory phase of cPMF



1 In this step, an exploratory PMF analysis is conducted on the joint AMS/EESI-TOF matrix. This  
 2 consists of a 2-D exploration of the solution space defined by the number of factors ( $p$ ) and relative  
 3 instrument weight ( $C$ ). For both factor interpretation and quantitative analysis, it is important that both  
 4 instruments be well-represented in any accepted PMF solution. In principle, the extent to which PMF  
 5 can explain a variable  $x_{i,j}$  is limited by the measurement uncertainty,  $s_{i,j}$ ; that is, the expectation value  
 6 of the scaled residual ( $e_{i,j}/s_{i,j}$ ) is 1 (i.e.,  $Q/Q_{expect} \sim 1$ ). In practice,  $e_{i,j}/s_{i,j}$  may be systematically above or  
 7 below 1, and differ between instruments, for several reasons. First, the accuracy of the error calculation  
 8 may be systematically different between instruments, leading to systematic differences in the effect of  
 9 residuals from a given instrument on  $Q$ . Second, the extent of internal correlations in the dataset may  
 10 differ between instruments. For example, fragmentation/thermal decomposition in the AMS can lead to  
 11 sequences of correlated ions (e.g.,  $C_nH_{2n+1}^+$  for alkanes). In contrast, for the EESI-TOF measurement of  
 12 individual molecular ions, ion-to-ion correlations depend solely on particle composition. Finally, even  
 13 for a case where ion-by-ion signal-to-noise and the extent of internal correlations is equal between  
 14 instruments, the relative number of variables (ions) included in the dataset may affect the weight due to  
 15 small drifts in instrument performance, modelling errors in PMF, and the prevalence of  
 16 transient/variable sources not fully captured by PMF. Therefore, it is important to assess the relative  
 17 weight of the two instruments and rebalance if necessary. We define a balanced solution as one in which  
 18 there are no systematic differences between quality of fit for different instruments (Crippa et al., 2013b;  
 19 Slowik et al., 2010; Crippa et al., 2013a). However, note that variable-to-variable differences in the  
 20  $e_{i,j}/s_{i,j}$  within the dataset of a single instrument are permitted (as in standalone PMF).

21  
 22 The instrument weighting process follows the method previously proposed by Slowik et al., (2010), in  
 23 which weighting is performed by applying a weighting factor  $C$  to the uncertainties and evaluated by  
 24 comparison of the AMS vs. EESI-TOF residuals. Here we utilise the same weighting method, but  
 25 propose an improved evaluation metric. Instrument weighting is performed by applying a weighting  
 26 factor  $C$  to the components of the uncertainty matrix  $S$  corresponding to one of the two instruments.  
 27 This increases/decreases the contribution of that instrument's residuals to  $Q$ , thereby changing its  
 28 weight within the PMF solver. In this paper, we applied the weighting factor, denoted  $C_{EESI}$ , to the  
 29 columns of  $S$  corresponding to ions measured by the EESI-TOF, according to Eq. (12):

$$30 \quad \frac{(s'_{i,j})_{j=EESI} = \frac{(s_{i,j})_{j=EESI}}{C_{EESI}}}{(s'_{i,j})_{j=AMS} = (s_{i,j})_{j=AMS}} \quad (13)$$

$$31 \quad \begin{cases} (s'_{i,j})_{j=EESI} = \frac{(s_{i,j})_{j=EESI}}{C_{EESI}} \\ (s'_{i,j})_{j=AMS} = (s_{i,j})_{j=AMS} \end{cases} \quad (12)$$

32  
 33 Note that  $C_{EESI} = 1$  is equivalent to an unweighted solution; and  $C_{EESI} > 1$  means the uncertainty matrix  
 34 of EESI-TOF decreases, which upweights the EESI-TOF.

35  
 36 As noted above, a balanced solution is defined as one in which the quality of fit to a given ion (assessed  
 37 via scaled residuals,  $e_{ij}/s_{ij}$ ) is independent of the instrument performing the measurement. In previous  
 38 work (Slowik et al., 2010; Crippa et al., 2013), the metric used to assess this was the mean of the  
 39 absolute scaled residuals. This metric assumes that the optimised solution for each individual instrument  
 40 yields approximately the same  $Q/Q_{exp}$ . In practice, this may vary between instruments for the reasons  
 41 described above. Further, this metric can be unduly influenced by a few large outliers. Therefore, we  
 42 employ a new approach which references the residuals from the combined dataset to those obtained  
 43 from the final solutions from single-instrument PMF, which having been selected as the optimal

1 representation of environmental data are assumed to likewise provide the optimised distributions of  
 2 single-instrument residuals. The new method is as follows:

3 1) From the result of each single instrument PMF (here AMS PMF, EESI-TOF PMF), calculate  
 4 the scaled residual ( $e_{ij}/s_{ij}$ ) probability distribution over the entire (single instrument) dataset. Here we  
 5 denote the scaled residual probability distribution function in the scaled residual ( $e_{ij}/s_{ij}$ ) space for EESI-  
 6 TOF and AMS as  $P_{\text{EESI}}(e_{ij}/s_{ij})$  and  $P_{\text{AMS}}(e_{ij}/s_{ij})$ , respectively.

7 2) Calculate the overlap fraction  $F_{\text{Overlap}}$  between the AMS and EESI-TOF scaled residual  
 8 probability distributions from the single instrument solutions, according to Eq. (13):  
 9

$$10 \quad F_{\text{Overlap}} = \int \min \left( P_{\text{EESI}} \left( \frac{e_{ij}}{s_{ij}} \right), P_{\text{AMS}} \left( \frac{e_{ij}}{s_{ij}} \right) \right) \quad (14)$$

$$11 \quad F_{\text{Overlap}} = \int \min \left( P_{\text{EESI}} \left( \frac{e_{ij}}{s_{ij}} \right), P_{\text{AMS}} \left( \frac{e_{ij}}{s_{ij}} \right) \right) \quad (13)$$

12 where  $P_{\text{EESI}}(e_{ij}/s_{ij})$  and  $P_{\text{AMS}}(e_{ij}/s_{ij})$  indicates the probability of occurrence of AMS and EESI-TOF at the  
 13 point  $e_{ij}/s_{ij}$  in scaled residual space, respectively. Given the previously mentioned assumption that the  
 14 single-instrument solutions represent the optimal representation of the data for the individual  
 15 instruments, the  $F_{\text{Overlap}}$  calculated at this step is the value that should likewise be obtained from a  
 16 balanced solution to the combined dataset. Therefore, we define the quantity  $F_{\text{Overlap}}^*$  as the  $F_{\text{Overlap}}$  of  
 17 the final single-instrument PMF solutions.

18 3) For the combined dataset, calculate  $F_{\text{Overlap}}$  as a function of a two-dimensional exploration  
 19 of the space defined by weighing factor ( $C_{\text{EESI}}$ ) and the number of factors ( $p$ ). This exploration is  
 20 necessary because the scaled residuals have been empirically observed to depend not only on  $C$  but also  
 21  $p$  (Crippa et al., 2013b; Slowik et al., 2010; Crippa et al., 2013a), likely because  $p$  affects the degrees  
 22 of freedom in the solution. We select for further analysis the set of solutions in which  $F_{\text{Overlap}}$  does not  
 23 greatly differ from  $F_{\text{Overlap}}^*$ , as given by Eq. (14):  
 24

$$25 \quad |F_{\text{Overlap}}(C, p) - F_{\text{Overlap}}^*| < \beta \quad (15)$$

$$26 \quad |F_{\text{Overlap}}(C, p) - F_{\text{Overlap}}^*| < \beta \quad (14)$$

27 where the threshold of absolute difference is defined as  $\beta$ . Here  $\beta$  is a subjective parameter chosen to  
 28 allow a manageable number of solutions to be selected for detailed inspection. For computational  
 29 efficiency, if one or more factors are constrained, we choose  $a = 0$  for all constrained factors at this  
 30 preliminary exploration stage and will explore the  $a$ -value range(s) for constraint(s) for further  
 31 bootstrapping analysis once the  $C$  and  $p$  are determined.  
 32

33 The balanced solutions satisfying Eq. (14) are then evaluated using the same metrics as in standard  
 34 PMF analysis to select the solution with the greatest explanatory power. This solution is used as the  
 35 base case for bootstrap analysis and, if one or more factors are constrained, simultaneous randomised  
 36  $a$ -value trials.  
 37

### 38 2.3.4 Bootstrap/constraint sensitivity analysis on the combined dataset

39 Bootstrap analysis (Davison and Hinkley, 1997) Bootstrap analysis (Davison and Hinkley, 1997) is  
 40 frequently used to characterise solution stability, reproducibility and estimate uncertainties. In typical  
 41 bootstrap analysis, a set of new input and error matrices are created by random resampling of rows from  
 42 the original input data and error matrices. The resulting resampled matrices preserve the original  
 43 dimensions of the input data matrix, but randomly duplicate some time points while excluding others  
 44 (Paatero et al., 2014)(Paatero et al., 2014). In the present analysis, we combined bootstrap analysis with

1 randomised selection of  $a$ -values for all constrained factors within predetermined limits defined on a  
2 factor-by-factor basis. Since the constrained factors use reference profiles constructed with an estimated  
3  $AS_k$  (see Eq. (4211)), this combined bootstrap/constraint analysis allows recalculation of  $AS_k$  within  
4 PMF for any factor with a non-zero  $a$  value. As a result, the final reported solution is the average of all  
5 accepted bootstrap runs, with uncertainties in factor profiles and time series taken as the standard  
6 deviation. To minimise the effect of estimated  $AS_k$  on constrained factors, we suggest that in the future  
7 this method could be improved by initialisation of constrained factor profiles with randomised  $AS_k$   
8 within a predefined range, in conjunction with the existing  $a$ -value/bootstrap routine.  
9

10 Within this analysis, the range of  $a$ -values explored for a given factor may have a significant effect on  
11 the acceptance probability. A very low acceptance probability is undesirable because it is  
12 computationally inefficient, while a very high acceptance probability is also undesirable because it  
13 implies the solution space is inadequately explored due to excessively restrictive  $a$ -values (Canonaco  
14 et al., 2021); values (Canonaco et al., 2021). Therefore, we conduct pre-tests to estimate the  $a$ -value  
15 range leading to a reasonable acceptance probability. This is done by a set of 2-dimensional  $a$ -value  
16 (“multi-2D”) scans in which the  $a$ -values of two constrained factors are varied stepwise from 0 to 1  
17 with a step size of 0.1 (i.e., 121 runs), while the  $a$ -values of other constrained factors are held at 0. The  
18 results of all multi-2D runs for a given factor are combined to determine the acceptance probability as  
19 a function of  $a$ -value, and upper and lower  $a$ -value boundaries are assessed. The acceptance criteria  
20 are dataset-specific and discussed later (Sect. 3.4 in the Text S2.4). When the number of constrained  
21 factors ( $p_{ref}$ ) = 2, the multi-2D algorithm is equivalent to an explicit exploration of all possible  $a$ -value  
22 combinations. However, for  $p_{ref} > 2$ , multi-2D is much more computationally efficient, because it  
23 increases as  $p_{ref}(p_{ref}-1)/2$ , whereas the explicit method increases as the factorial of  $p_{ref}$ . For the datasets  
24 used here, in which  $p_{ref}$  is 3 (summer) and 4 (winter), the multi-2D approach decreases the number of  
25 runs required for  $a$ -value pre-scans by factors of ~4 and ~20, respectively.

26  
27 Acceptance criteria consist of both the assessment of specific features of selected factor profiles/time  
28 series (see Sect. 3.4 Text S2.4), as well as a general evaluation of whether the solution is qualitatively  
29 similar to the base case. That is, we require that the time series of each factor from a PMF run to be  
30 unambiguously related to the corresponding base case factor (Stefenelli et al., 2019; Vlachou et al.,  
31 2019; Tong et al., 2021). The key steps of this method are summarised below: 1) identify a base case,  
32 which as discussed above is defined by a weighting factor  $C$ , number of factors  $p$ , and set of constrained  
33 factors with the  $a$ -value set to 0; 2) calculate the Spearman correlation between the time series of base  
34 case and the multi-2D scans, which yields a correlation matrix with the highest correlation values on  
35 the diagonal; 3) each correlation coefficient on the matrix diagonal must be by a statistically significant  
36 margin (using different confidence levels from a  $t$  test) than any value on the intersecting row or column.  
37 In the current study, we selected a confidence level of 0 for this base case/bootstrap correlation test,  
38 representing the most permissive application of this criterion. That is, we require only that the diagonal  
39 matrix mentioned above can be constructed, i.e., that there is a unique 1:1 correspondence between base  
40 case factors and factors from the bootstrap/ $a$ -value analysis.

41  
42 The final set of PMF runs consisted of 1000 bootstrap runs, conducted at a single combination of  $C_{EESI}$   
43 and  $p$ , with  $a$ -values randomly selected with a step size of 0.05 for summer and 0.1 for winter within  
44 the factor-specific limits determined via the multi-2D pre-scans. The same acceptance criteria utilised  
45 for the multi-2D pre-scans were also used for the bootstrap runs. As a final solution, we report the mean  
46 factor profiles and time series determined from all accepted bootstrap runs, with the standard deviation  
47 taken to represent the uncertainty of the analysis procedure. Although not currently implemented within  
48 the analysis software used, we note that in theory it would be possible to additionally include random

1  $C_{EESI}$  selection (within a predefined range corresponding to balanced solutions) and randomised  $AS_k$  for  
2 constrained profiles (within a user-defined range) in this stage of the analysis and in calculation of the  
3 final model outputs.

### 7 3. Results

9 We have conducted cPMF analysis on datasets collected from the summer and winter campaigns. The  
10 parameters for the PMF analysis of the combined dataset and the re-analysed summer and winter  
11 datasets are summarised in Table 1. We re-ran the conventional PMF on the summer and the winter  
12 data, obtaining results similar to Stefenelli et al. (2019) and Qi et al. (2019), as discussed in Text S2 in  
13 the Supplement. Other technical details of method validation and solution selections are also explained  
14 in the Supplement (from the Text S2.2 to Text S2.4), including reference profile construction, the  
15 determination of  $C_{EESI}$  and number of factors  $p$ , and the determination of case-specific  $a$  value range  
16 and acceptance criteria for bootstrap analysis. Table 2 summarises these case-specific facts for summer  
17 and winter datasets, including  $a$  value range for constrained factors, criteria for  $a$  value range and  
18 accepted bootstrap run selection, and the number of accepted runs from the final combined bootstrap.

20 Here we present final results from the cPMF analysis of the summer and winter campaigns in Sect 3.1.1  
21 and Sect 3.1.2, respectively. The final solutions are reported as the average of all accepted bootstrap/ $a$ -  
22 value randomisation runs (764 for summer, 308 for winter), with uncertainties corresponding to the  
23 standard deviation. As the  $NO^+$  and  $NO_2^+$  signals are included in these two datasets and they can result  
24 from either organic or inorganic nitrate, we estimate the organic and inorganic contributions to the  $NO^+$   
25 and  $NO_2^+$  signal in each factor using the method of Kiendler-Scharr et al. (2016) (see Text S3). We  
26 compare the cPMF factors to their counterparts from the standalone AMS and EESI-TOF solutions, for  
27 cases where a clear factor-to-factor correspondence exists. The further exploration on EESI-TOF  
28 sensitivities to resolved factors are discussed in Sect 3.2.

30 Due to the complexity of the analysed datasets (2 seasons  $\times$  3 PMF methods), we use the following  
31 convention for identifying factors: factorName<sub>season,method</sub>, where “factorName” is the name of the factor  
32 (e.g., COA for cooking-related organic aerosol), “season” denotes either the summer (“S”) or winter  
33 (“W”) dataset, and “method” refers to PMF on standalone AMS dataset (“A”), standalone EESI-TOF  
34 dataset (“E”), or combined dataset (“C”). For example, COA<sub>S,C</sub> stands for the cooking-related factor  
35 retrieved from cPMF applied to the summer dataset.

#### 37 3.1 Method validation and solution selection

##### 39 3.1.1 PMF analysis of single instrument datasets

40 Single instrument AMS and EESI TOF PMF analysis was previously conducted and validated for both  
41 the summer and winter datasets (Qi et al., 2019; Stefenelli et al., 2019). To determine the  $F_{\text{overlap}}^*$ , the  
42 EESI TOF only PMF was re-run on only the period when both AMS and EESI TOF were operating.  
43 In addition, the AMS PMF analysis was re-run on the same period, but with the  $NO^+$  and  $NO_2^+$  ions  
44 included. As discussed above, these ions contain a large fraction of the AMS signal deriving from  
45 organonitrates. For EESI TOF only PMF analysis in both datasets, we used the same constraints as in  
46 the referenced studies, that is, cooking-influenced OA (COA<sub>S,E</sub>) was constrained for the summer dataset  
47 and cigarette-smoking OA (CSOA<sub>W,E</sub>) was constrained for the winter dataset. For AMS-only PMF

Formatted: Normal, Level 1

Formatted: Font: Times New Roman

Formatted: Font: Times New Roman

Formatted: Font: Times New Roman

Formatted: Font: Not Bold

Formatted: Add space between paragraphs of the same style, Line spacing: Multiple 1.15 li

Formatted: Font: Not Bold

Formatted: None, Space After: 10 pt, Add space between paragraphs of the same style, Line spacing: Multiple 1.15 li

1 analysis, the only constrained factor in the original studies was hydrocarbon-like OA during winter  
2 ( $\text{HOA}_{w,A}$ ). We additionally constrained inorganic nitrate (InorgNit) in both the summer and winter  
3 datasets, by including 1) the  $\text{CO}_2^+ / (\text{NO}^+ + \text{NO}_2^+)$  ratio, where the  $\text{CO}_2^+$  signal was produced by reaction  
4 of nitrate on the vaporiser (Pieber et al., 2016), as well as minor organic contaminants, and 2)  $\text{NO}^+ / \text{NO}_2^+$   
5 ratio. In summer, we took the mass spectrum acquired from the  $\text{NH}_4\text{NO}_3$  calibration period during the  
6 campaign to calculate the ratios in 1) and 2), whereas in winter, we constructed the reference using the  
7 two ratios from the ambient measurements (2.54) during periods of high nitrate to organic ratios.

8 Fig. S1 and Fig. S2 show the results from these single instrument AMS and EESI TOF PMF analyses  
9 for summer and winter, respectively, as well as a comparison with the factor time series from the  
10 original studies. Because the results are very similar to the single instrument studies, they are discussed  
11 only briefly here. The AMS only PMF yielded five OA factors consistent with those of Stefenelli et al.  
12 (2019), namely hydrocarbon-like OA ( $\text{HOA}_{s,A}$ ), cooking-influenced OA ( $\text{COA}_{s,A}$ ), cigarette smoking  
13 OA ( $\text{CSOA}_{s,A}$ ), more oxygenated OA,  $\text{MO-OOA}_{s,A}$ , and less oxygenated OA ( $\text{LO-OOA}_{s,A}$ ), and  
14 additionally a factor dominated by  $\text{NO}^+$  and  $\text{NO}_2^+$  in a ratio consistent with that of ammonium nitrate,  
15 denoted  $\text{InorgNit}_{s,A}$ . The main difference between these results and those reported by Stefenelli et al.  
16 (2019) is some exchange of signal between  $\text{MO-OOA}_{s,A}$  and  $\text{LO-OOA}_{s,A}$ . In addition, the contribution  
17 from  $\text{NO}^+$  and  $\text{NO}_2^+$  is not solely apportioned to  $\text{InorgNit}_{s,A}$  but also to factors such as  $\text{LO-OOA}_{s,A}$ ;  
18 however, this does not affect the identity and interpretation of these factors.

19 Similarly, for the winter dataset, seven factors were resolved consistent with the OA factors determined  
20 by Qi et al. (2019), namely  $\text{HOA}_{w,A}$ ,  $\text{COA}_{w,A}$ ,  $\text{LO-OOA}_{w,A}$ ,  $\text{MO-OOA}_{w,A}$ , biomass burning OA  
21 ( $\text{BBOA}_{w,A}$ ), event specific OA ( $\text{EVENT}_{w,A}$ ) and nitrogen rich OA ( $\text{NitrogenOA}_{w,A}$ ), as well as a new  
22 factor consistent with  $\text{InorgNit}_{w,A}$ . Apart from being apportioned to  $\text{InorgNit}$ ,  $\text{NO}^+$  and  $\text{NO}_2^+$  were also  
23 apportioned to non  $\text{InorgNit}$  factors, indicating organonitrate content and/or imperfect attribution of  
24 inorganic  $\text{NO}^+$  and  $\text{NO}_2^+$  to these factors. Although the  $\text{NO}^+$  and  $\text{NO}_2^+$  contributions in some non-  
25  $\text{InorgNit}$  factors are significant, causing some changes in the factor time series compared to those in Qi  
26 et al. (2019), the main features of the spectra from other OA components (i.e., ions other than  $\text{NO}^+$  and  
27  $\text{NO}_2^+$ ) in these factors are retained.

28 As discussed in Sect. 2.3.3, scaled residual probability distributions, i.e.,  $P(e_{ij}/s_{ij})$ , for the selected  
29 single instrument solutions were calculated and are shown in Fig. 3. As discussed in Eq. (14), this yields  
30 values for  $F_{\text{overlap}}^*$ , which are calculated to be 0.769 in summer and 0.899 in winter.

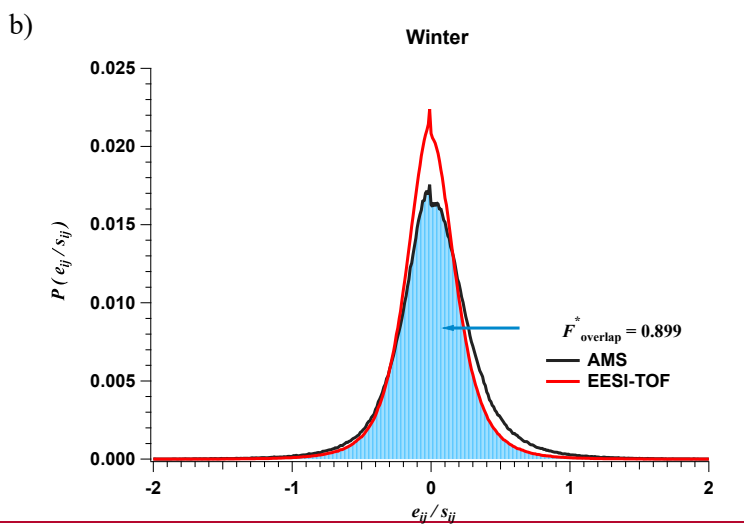
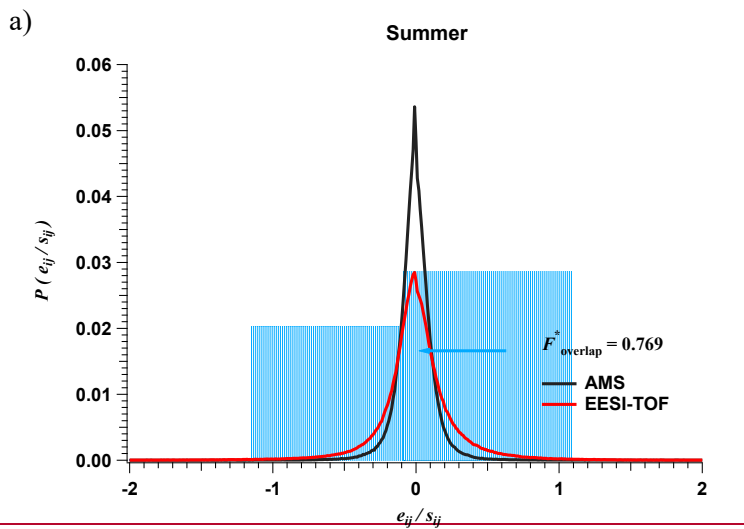


Figure 3. Scaled residual probability distributions and region of overlap from individual AMS PMF solution and EESI TOF PMF solutions for the summer (a) and winter (b) datasets. Red and black lines show the residual distributions for the EESI TOF and AMS, respectively; shading denotes the region of overlap.



1 **Table 1** Summary of parameters for the PMF analysis of re-analysed summer and winter datasets, and  
 2 the combined dataset. There are 257 ions that are found in PMF input matrices for both the summer and  
 3 winter datasets (common ions are listed in the Table S1). All datasets include AMS measurements of  
 4  $\text{NO}^+$  and  $\text{NO}_2^+$ .

		EESI-TOF	AMS	Combined
Summer	Matrix dimensions (time points $\times$ $m/z$ )	1779 $\times$ 507	1779 $\times$ 287	1779 $\times$ 794
	Time period	20 to 26 June 2016	20 to 26 June 2016	20 to 26 June 2016
	Time resolution (min)	5	5	5
	Range of $p$ analysed	6	6	5-10
Winter	Matrix dimensions (time points $\times$ $m/z$ )	6142 $\times$ 892	6142 $\times$ 258	6142 $\times$ 1150
	Time period	25 Jan to 4 Feb 2017	25 Jan to 4 Feb 2017	25 Jan to 4 Feb 2017
	Time resolution (min)	1	1	1
	Range of $p$ analysed	12	8	7-14

5

### 6 **3.1.2 Construction of reference profiles**

7

8 In the cPMF analysis, the factor profiles for HOA, COA, and InorgNit were constrained in both the  
 9 summer and winter datasets, while CSOA was constrained in winter only. All reference profiles were  
 10 constructed according to Eq. (12). Here we discuss the methods used to determine  $(f_{k,j})_{j=AMS,ref}$ ,  
 11  $(f_{k,j})_{j=EESI,ref}$ , and the estimated  $AS_k$  used to synthesise the reference profile. Note that COA and  
 12 CSOA are retrieved by both AMS and EESI-TOF, while HOA and InorgNit are not retrieved by the  
 13 EESI-TOF in the configuration used for these campaigns. Specifically, no HOA-sensitive EESI-TOF  
 14 extraction/ionisation scheme has yet been developed, while the measurable ion corresponding to  
 15 inorganic nitrate,  $[\text{NaNO}_2]\text{Na}^+$ , has been detected in other studies (Tong et al., 2021) but falls below the  
 16  $m/z$  transmission window used here.

17 For summer  $\text{COA}_{S,C}$ ,  $(f_{k,j})_{j=AMS,ref}$  and  $(f_{k,j})_{j=EESI,ref}$  were taken from the factor profiles for  
 18  $\text{COA}_{S,A}$  and  $\text{COA}_{S,E}$ , respectively.  $AS_{\text{COA}_S}$  was calculated as the ratio of the mean signals of  $\text{COA}_{S,E}$   
 19 (eps) to  $\text{COA}_{S,A}$  ( $\mu\text{g m}^{-3}$ ). For  $\text{HOA}_{S,C}$ ,  $(f_{k,j})_{j=AMS,ref}$  the HOA profile of Crippa et al. (2013b) was  
 20 used, and for  $\text{InorgNit}_{S,C}$ , it was taken to be the mass spectrum acquired from the  $\text{NH}_4\text{NO}_3$  calibration  
 21 period during the campaign. The latter included the  $\text{CO}_2^+$  signal produced by reaction of nitrate on the  
 22 vaporiser (Pieber et al., 2016), here observed with a  $\text{CO}_2^+(\text{NO}^+ + \text{NO}_2^+)$  ratio of 0.0345, as well as  
 23 minor organic contaminants. For both  $\text{HOA}_{S,C}$  and  $\text{InorgNit}_{S,C}$  all ions in  $(f_{k,j})_{j=EESI,ref}$  were set at  
 24 the same intensity, and  $AS_k$  was selected to be  $0.01 \text{ eps } (\mu\text{g m}^{-3})^{-1}$ .

25 The  $\text{COA}_{W,C}$  reference profile was constructed using the identical method as for  $\text{COA}_{S,C}$ , with  $\text{COA}_{W,A}$   
 26 and  $\text{COA}_{W,E}$  as references. For  $\text{CSOA}_{W,C}$ ,  $(f_{k,j})_{j=EESI,ref}$  was taken to be the  $\text{CSOA}_{W,E}$  profile.  
 27 However, because the AMS did not resolve CSOA in the winter, we used the  $\text{CSOA}_{S,A}$  profile for  
 28  $(f_{k,j})_{j=AMS,ref}$  and estimated  $AS_{\text{CSOA}_W}$  as follows:

$$AS_{CSOA,w} = \frac{AS_{COA,w}}{AS_{COA,s}} \cdot AS_{CSOA,s} \quad (16)$$

where  $AS_{COA,s}$ ,  $AS_{CSOA,s}$ , and  $AS_{COA,w}$  are the EESI-TOF apparent sensitivities of the corresponding factors, calculated assuming direct correspondence between the AMS and EESI-TOF factors sharing the same name (Stefenelli et al., 2019; Qi et al., 2019).

The reference profile for  $HOA_{w,C}$  is identical to  $HOA_{s,C}$  and constructed in the same way using the same profile as in the summer dataset. Unlike summer, the calibration mass spectrum of  $NH_4NO_3$  was not used as the reference profile for  $InorgNit_{w,C}$  because the  $NO^+/NO_2^+$  in the  $NH_4NO_3$  calibration period (1.58) was not consistent with that observed from ambient measurements (2.54) during periods of high nitrate to organic ratios, possibly indicating contributions from non- $NH_4^+$  cations. Instead, the  $InorgNit$  reference profile of AMS ions was constructed based on these features: 1) the  $NO^+/NO_2^+$  ratio (2.54) from 26 Jan 2016 to 31 Jan 2016, when the instrument remained stable and the ratio of nitrate to OA was high, suggesting the contribution from organonitrates to  $NO^+$  and  $NO_2^+$  was low, 2) the  $CO_2^+/(NO^+ + NO_2^+)$  ratio (0.00026) was assumed to be the same as during the calibration period in the Zurich winter campaign and 3) the ratio of intensity of each organic ion to  $CO_2^+$  was kept the same as during the calibration period in the Zurich winter campaign. Then  $(f_{w,j})_{j=EESI,ref}$  and  $AS_{InorgNit,w}$  were determined using the same method as in summer.

17

### 3.1.3 Determination of $C_{EESI}$ and number of solutions

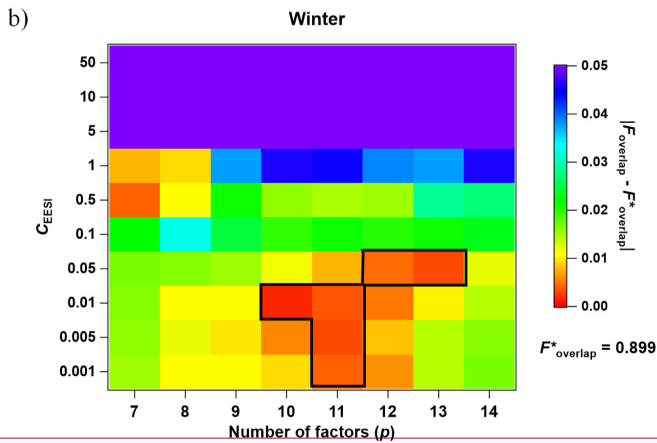
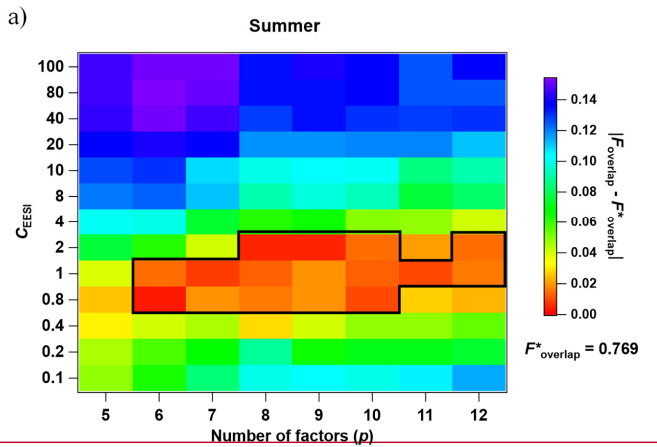
Because  $F_{overlap}$  depends on both the weighting factor  $C_{EESI}$  and the number of factors  $p$ , an exploration of this two dimensional space is required. As discussed earlier, for computational efficiency the  $\alpha$  values of all constrained factor profiles were set to zero during this initial exploration. For the summer dataset, in which both the AMS only and EESI-TOF only PMF analyses yielded 6 factors, the cPMF was explored from 5 to 12 factors with  $HOA_{s,C}$ ,  $COA_{s,C}$  and  $InorgNit_{s,C}$  constrained. For the winter dataset, in which the AMS only and EESI-TOF only PMF analyses yielded 8 and 11 factors, respectively, the cPMF was explored from 7 to 15 factors with  $HOA_{w,C}$ ,  $COA_{w,C}$ ,  $CSOA_{w,C}$  and  $InorgNit_{w,C}$  constrained. For the summer dataset,  $C_{EESI}$  was explored from 0.1 to 100, and in winter from 0.001 to 50. The results of this exploration are shown in Fig. 4a and Fig. 4b, which present  $|F_{overlap} - F_{overlap}^*|$  as a function of  $C_{EESI}$  and  $p$  for the summer and winter datasets, respectively.

29

The Zurich summer dataset displays the expected trend of  $|F_{overlap} - F_{overlap}^*|$  with respect to  $C_{EESI}$ . Balanced solutions are found at intermediate values of  $C_{EESI}$ , with lower and higher values yielding solutions in which the AMS and EESI-TOF, respectively, are overweighted. Examples of scaled residual distributions for these three cases (AMS overweighted, balanced, and EESI-TOF overweighted) are shown in Fig. S3. The black box in Fig. 4a denotes a set of solutions satisfying the criterion in Eq. (15), which are selected for further inspection. The value of  $\beta$  is selected empirically to yield a practical number of solutions for manual inspection, with 0.02 chosen for summer and 0.005 for winter. Factor profiles and time series for solutions satisfying the  $\beta$  criterion, comprising solutions with 6 to 9 factors (black box in the figure) are shown in Figs S4 to Fig. S13. An 8 factor solution was chosen as the best representation of the data, and included  $HOA_{s,C}$ ,  $COA_{s,C}$ ,  $CSOA_{s,C}$ ,  $InorgNit_{s,C}$ , two daytime SOAs ( $DaySOA1_{s,C}$  and  $DaySOA2_{s,C}$ ) and two nighttime SOAs ( $NightSOA1_{s,C}$  and  $NightSOA2_{s,C}$ ), discussed in detail in Sect. 3.2.1. Solutions with higher numbers of factors yielded uninterpretable splits in the SOA or CSOA factors. Among the balanced 8 factor solutions, we selected the solution with  $C_{EESI} = 2$ , which has the minimum value of  $|F_{overlap} - F_{overlap}^*|$ . This solution serves as the base case for further analysis. The other 8 factor solutions exhibit time series and profiles that are similar to the selected solutions. Therefore, we simply select the 8 factor solution with minimum  $|F_{overlap} - F_{overlap}^*|$ .

46

1 For the winter dataset, solutions with 12 or more factors are similar to the summer in which balanced  
 2 solutions (i.e.,  $\beta < 0.005$ ) are clustered narrowly around a single value of  $C_{EESI}$  (in this case 0.05), as  
 3 shown in the right black box in Fig. 4b. However, in addition, solutions with 10 to 11 factors show  
 4 balanced solutions over a relatively broad range,  $C_{EESI} = 0.001$  to 0.01, as shown in the left black box  
 5 in Fig. 4b. This complex behaviour highlights the importance of fully exploring the two dimensional  
 6 space. Solutions from the left black box (e.g., a 10 factor solution with  $C_{EESI} = 0.01$ , and 11 factor  
 7 solutions with  $C_{EESI} = 0.001$ , 0.005, and 0.001 which are shown in Fig. S14 to Fig. S17) exhibited mixed  
 8 factors, in which biomass burning was not clearly separable from other sources. In contrast, the 12-  
 9 factor solution (see Fig. S18) and 13 factor solution (see Fig. S19) in the narrow band successfully  
 10 resolves these factors. The 12-factor and 13-factor solutions differ in that the 13-factor solution includes  
 11 uninterpretable splitting of biomass-burning-related factors. Similarly, higher-order solutions also result  
 12 in uninterpretable factor splitting. Therefore, the 12-factor solution with  $C_{EESI}$  of 0.05 is selected as the  
 13 best representation of the combined dataset.



17 Figure 4. Identification of balanced solutions in the combined dataset (i.e.,  $|F_{\text{overlap}} - F_{\text{overlap}}^*|$  as a  
 18 function of  $C_{EESI}$  and  $p$ ) for summer (a) and winter (b) datasets. Note that  $|F_{\text{overlap}} - F_{\text{overlap}}^*| = 0$  defines  
 19 a balanced solution. Solutions within the black box satisfied the  $|F_{\text{overlap}} - F_{\text{overlap}}^*| < \beta$  criterion  
 20 defined in Eq. (15) ( $\beta$  is set to be 0.02 and 0.005 for summer and winter, respectively) and were selected

1 as base case candidates, from which the base case that can best represent the combined data was selected  
2 by manual inspection.

### 3 3.1.4— Acceptance criteria and factor specific $\alpha$ value boundaries

4 As discussed in Sect. 2.3.4, the combined bootstrap/ $\alpha$  value randomisation analysis requires (1) a set of  
5 criteria for solution acceptance/rejection and (2) factor specific boundaries for randomised  $\alpha$  value  
6 selection to maintain computational efficiency. The final set of acceptance criteria and  $\alpha$  value  
7 boundaries are presented in Table 2. Here we discuss their selection, which is determined synergistically  
8 by consideration of 1) unique correlations of factor time series with the base case (see Sect. 2.3.4), 2)  
9 factor-based acceptance criteria, which are here based on selected key mass spectral features (see Sect.  
10 3.2.1 and Sect. 3.2.2 for a complete discussion of factor characteristics). Both (1) and (2) are evaluated  
11 as a function of changing  $\alpha$  values within the multi-2D scanning algorithm (see Sect. 2.3.4). For  
12 assessing the solution/base case correlations, we utilise a confidence level of 0, meaning that the only  
13 requirement is the ability to construct a correlation matrix with the values on the diagonal being higher  
14 than any vertical or horizontal transect. This accepts the largest possible number of solutions while  
15 requiring an unambiguous relationship between base case and bootstrapped factors. Recall that the  
16 multi-2D algorithm consists of two dimensional  $\alpha$  value scans in which the  $\alpha$  values of constrained  
17 factors are scanned from 0 to 1 with a step size of 0.1, the  $\alpha$  values of other constrained factors are set  
18 to zero, and the remaining factors are left free.

19 Here we describe the general steps to determine acceptance criteria and  $\alpha$  value boundaries. A factor-  
20 based acceptance criterion is defined by the combination of a diagnostic quantity relating to one or more  
21 factors and a corresponding acceptance/rejection threshold ( $\theta$ ). Solutions that fulfil all criteria  
22 simultaneously are classified as accepted solutions. We calculate the acceptance probability as a  
23 function of  $\alpha$  value for a given factor (this is calculated independently for each factor). For a given  
24 factor, the acceptance probability is defined as the ratio of the number of accepted solutions to the total  
25 number of solutions, for which the factor has the selected  $\alpha$  value and the  $\alpha$  value of at most one other  
26 constrained factor is non zero (that is, we consider only multi-2D runs where the factor in question is  
27 being scanned against a single other factor, while discarding runs for which the factor in question is  
28 fixed at  $\alpha=0$  while two other factors are scanned; this is relevant only for analyses with at least 3  
29 constrained factors). The acceptance probability is not only a function of the  $\alpha$  value of the target  
30 constraint but also a function of the threshold  $\theta$ . When an appropriate value of  $\theta$  cannot be defined *a*  
31 *priori*, it is selected via sensitivity tests. The final selection of the threshold  $\theta$  and  $\alpha$  value ranges is a  
32 compromise between (1) maintaining a reasonably high acceptance probability, thereby providing  
33 sufficient statistics without an excessive number of bootstrap runs; and (2) ensuring a sufficiently broad  
34 exploration of the solution space to encompass most environmentally reasonable solutions and thus  
35 accurately assess errors. Therefore, we determine the threshold  $\theta$  and  $\alpha$  value upper limit for each  
36 constrained factor at which a steep drop-off from high to low probability of acceptance occurs.

37 For the summer dataset, three factors are constrained: HOA<sub>s,c</sub>, COA<sub>s,c</sub>, and InorgNits<sub>s,c</sub>, yielding three  
38 pairs ( $C(3,2) = 3$ ) of two dimensional  $\alpha$  value scans. Two factor based diagnostic quantities with  
39 acceptance/rejection thresholds ( $\theta$ ) were selected: 1) the ratio of C<sub>3</sub>H<sub>3</sub>O<sup>+</sup> to C<sub>3</sub>H<sub>2</sub>O<sup>+</sup> for COA<sub>s,c</sub> should  
40 be higher than the threshold  $\theta_{\text{COA}_{s,c}}$  (Mohr et al., 2012), and 2) the ratio of CO<sub>2</sub><sup>+</sup>/(NO<sup>+</sup>+NO<sub>2</sub><sup>+</sup>) for  
41 InorgNits<sub>s,c</sub> should not be higher than  $\theta_{\text{InorgNits}_{s,c}}$  because the CO<sub>2</sub><sup>+</sup> signal in InorgNits<sub>s,c</sub> should not  
42 greatly exceed the CO<sub>2</sub><sup>+</sup> signal produced by reaction of nitrate on the vaporiser (Pieber et al., 2016);  
43 excessively high values would indicate mixing with OA. To explore the sensitivity of the acceptance  
44 probability to the threshold  $\theta$ , we varied  $\theta_{\text{COA}_{s,c}}$  from 4.5 to 5.1 with a step of 0.1 (note that 5.0 is the

ratio of  $C_3H_3O^+ / C_3H_5O^+$  in the reference profile) and  $\theta_{\text{InorgNit}_{s,c}}$  from 0.034 to 0.040 with a step of 0.01, (note that 0.0345 is the ratio of  $CO_2^+ / (NO^+ + NO_2^+)$  in the reference profile):

The acceptance probability as a function of  $a$  value and the various thresholds ( $\theta$ 's) for  $COA_{s,c}$ ,  $InorgNit_{s,c}$ , and  $HOA_{s,c}$  are shown in Fig. S22. Vertical dashed lines denote the final selected  $a$  values, while the thicker traces denote the selected  $\theta$  values (both of which are also given in Table 2). For  $\theta_{COA_{s,c}} > 5.0$ , very few runs are accepted. Within the range  $4.5 \leq \theta_{COA_{s,c}} \leq 5.0$ ,  $\theta_{COA_{s,c}}$  does not affect the relationship between acceptance probability and  $a$  value for  $InorgNit_{s,c}$  (Fig. S22b), but has a considerable effect for  $COA_{s,c}$  and  $HOA_{s,c}$ , with a decreasing  $\theta_{COA_{s,c}}$  leading to the acceptance probability remaining high at larger  $a$  values. Visual inspection of the solutions suggests that this is due to increased mixing, mostly between  $COA_{s,c}$  and  $HOA_{s,c}$ . Therefore, we select a value of  $\theta_{COA_{s,c}} = 5.0$ , corresponding to the  $C_3H_3O_3^+ / C_3H_5O_3^+$  in the factor profile. For  $\theta_{InorgNit_{s,c}}$ , values smaller than 0.0345 (i.e., reference profile) result in a very low acceptance probability, whereas choice of  $\theta_{InorgNit_{s,c}}$  results in similar acceptance probabilities as a function of  $a$  value. Therefore, we select 0.0345, as the acceptance probability for  $\theta_{InorgNit_{s,c}}$  of 0.035 is not substantially different from 0.0345. Having selected these  $\theta$  values, we set  $a$  value limits at the point where an incremental increase/decrease in  $a$  yields a large change in acceptance probability (i.e. transition from high probability to low probability). For the current dataset, constrained factors, and selected  $\theta$ 's, there is no such transition at low  $a$  values, and we therefore select only an upper limit for the  $a$  values. For  $COA_{s,c}$ , there is a clear decrease for both criteria between  $a_{COA_{s,c}} = 0.1$  and  $a_{COA_{s,c}} = 0.2$ , and we therefore set the  $a$  value boundaries as  $0 \leq a_{COA_{s,c}} \leq 0.2$ .  $InorgNit_{s,c}$  maintains an acceptance probability of ~50 % for  $a_{InorgNit_{s,c}} \leq 0.4$ , before decreasing to ~20 % at  $a_{InorgNit_{s,c}} = 0.5$  and ~0 for  $a_{InorgNit_{s,c}} > 0.5$ ; therefore the range  $0 \leq a_{InorgNit_{s,c}} \leq 0.5$  is chosen. Finally, for  $HOA_{s,c}$ , the acceptance probability decreases from ~55 % at  $a_{HOA_{s,c}} \leq 0.1$  to ~35 % at  $a_{HOA_{s,c}} \leq 0.2$ , so the  $a$  value range for  $HOA_{s,c}$  is selected as  $0 \leq a_{HOA_{s,c}} \leq 0.2$ . The  $a$  values selected for constraints for the further summer bootstrap analysis are summarised in Table 2. However, we also see that for  $HOA_{s,c}$  the acceptance probability increases and stays high again for the  $a$  value of 0.4 to 0.8. Therefore, we made an additional bootstrap analysis to explore the result when the  $a$  value of  $HOA_{s,c}$  randomises from 0 to 0.8, as discussed in the last paragraph in this section.

In the winter dataset, four factors ( $HOA_{w,c}$ ,  $COA_{w,c}$ ,  $CSOA_{w,c}$ , and  $InorgNit_{w,c}$ ) are constrained, yielding six pairs ( $C(4,2) = 6$ ) of two-dimensional  $a$  value scans. Compared to the summer dataset, the unique base case/bootstrap correlation requirement yields a much smaller number of accepted solutions, probably due to the more complicated aerosol sources and/or evolution conditions in winter (e.g., multiple biomass burning related factors). Three factor based diagnostic quantities were selected: 1) the fraction of the nicotine signal ( $[C_{10}H_{14}N_2]H^+$ ) apportioned to  $CSOA_{w,c}$ , 2) the relative intensity of the AMS primary biomass burning tracer  $C_2H_4O_2^+$  (Alfarra et al., 2007; Cubison and Jimenez, 2015) in the factor profiles (AMS part) of less aged biomass burning ( $LABB_{w,c}$ ) vs. more aged biomass burning ( $MABB_{w,c}$ ), and 3) the relative intensity of the EESI-TOF primary biomass burning tracer levoglucosan ( $[C_6H_{10}O_5]Na^+$ ) (Qi et al., 2019; Stefenelli et al., 2019; Lopez Hilfiker et al., 2019) in the factor profiles of  $LABB_{w,c}$  vs.  $MABB_{w,c}$ . For 2) and 3), we require that the contribution of the primary tracer is higher for the profile of  $LABB_{w,c}$  than  $MABB_{w,c}$  as follows:

$$\frac{LABB_{w,c,10n} - MABB_{w,c,10n}}{(LABB_{w,c,10n} + MABB_{w,c,10n})/2} > \theta_{10n} \quad (17)$$

1 where  $LABB_{w,c,ion}$  and  $MABB_{w,c,ion}$  are the "ion" intensity in the  $LABB_{w,c}$  and  $MABB_{w,c}$  factor  
2 profiles, and "ion" in Eq. (17) denotes either AMS  $C_2H_4O_2^+$  (criterion 2) or EESI-TOF levoglucosan  
3 ( $[C_6H_{10}O_5]Na^+$ ) (criterion 3), and  $\theta_{ion}$  denotes the acceptance threshold.

4 For criterion 1), we select the threshold  $\theta_{CSOA_{w,c}}$  from investigation of Fig. S23, which shows the  
5 frequency distribution of the fraction of total nicotine signal apportioned to  $CSOA_{w,c}$ , derived from the  
6 multi-2D scans used to assess criteria 2 and 3 (see below). The figure shows that for nearly all runs, the  
7 fraction of total nicotine mass apportioned to this factor is higher than 0.96. The exceptions are clear  
8 outliers, and we therefore select  $\theta_{CSOA_{w,c}} = 0.96$  which was therefore chosen as the criterion threshold.

9 The acceptance probability as a function of  $a$ -value is shown in Fig. S24 for  $HOA_{w,c}$ ,  $COA_{w,c}$ ,  
10  $InorgNit_{w,c}$  and  $CSOA_{w,c}$ . For criteria 2 and 3, sensitivity tests are conducted using  $\theta_{C_2H_4O_2^+}$  and  
11  $\theta_{levoglucosan}$ , which were varied from 0 to 1 with a step of 0.1, and the final selected values are shown  
12 as a thicker line. The acceptance probability decreases to near zero for  $\theta_{C_2H_4O_2^+} \geq 0.1$  and  $\theta_{levoglucosan}$   
13  $\geq 0.2$ . We select 0 for both thresholds, which is the most permissive value, requiring only that  $MABB_{w,c}$   
14 appear more aged than  $LABB_{w,c}$  (i.e., reduced contribution from POA tracers). Similar to the summer  
15 dataset, there is no major decrease in acceptance probability at low  $a$  values, and we therefore impose  
16 only an upper limit. For  $HOA_{w,c}$ , we set the upper  $a$  value boundary at 0.9, due to the large decrease in  
17 acceptance probability at  $a_{HOA_{w,c}} = 1.0$ . However, for the other constrained factors, the acceptance  
18 probability decreases steadily without a steep drop off. We target an acceptance probability of 0.4 (by  
19 considering the unmixing status) as a subjective compromise between exploration and computational  
20 efficiency, and select as an upper boundary the largest  $a$  value that achieves this. This results in upper  
21  $a$  value limits of 0.3 for  $COA_{w,c}$  and 0.5 for  $InorgNit_{w,c}$ . For  $CSOA_{w,c}$ , the high acceptance probability  
22 is kept high from the  $a$  value of 0 to 0.6. Therefore, we chose the  $a$  value range of  $CSOA_{w,c}$  to be 0 to  
23 0.6. However, it is also observed that the acceptance probability for this factor dips at 0.7 and stays high  
24 again at  $a$  values of 0.8 and 0.9, so we made an additional bootstrap analysis with the  $a$  value range for  
25  $CSOA_{w,c}$  of 0 to 0.9 to explore the influence of the  $a$  value of this factor on overall result, as discussed  
26 in the following paragraph. The  $a$  values selected for the four constraints for the further winter bootstrap  
27 analysis are summarised in Table 2.

28 After  $a$  value selection, 1000 bootstrap runs were performed for summer and winter, respectively, and  
29 in each bootstrap run, an  $a$  value was randomly selected for each constrained factor, with a step size of  
30 0.05 for summer and 0.1 for winter within the corresponding range. The criteria for accepted solutions  
31 in the bootstrap analysis are exactly the same as the criteria and  $\theta$  in Sect. 3.1.4, and are given in Table  
32 2. As noted above, accepted solutions must simultaneously satisfy all criteria including the time series-  
33 based mixing status exploration and mass spectral based criteria. Note that we also did an additional  
34 bootstrap analysis for summer and winter, respectively, as mentioned in previous paragraphs, to explore  
35 the bootstrap result with larger  $a$  value range of  $HOA_{s,c}$  and  $CSOA_{w,c}$ . In the additional bootstrap  
36 analysis for summer,  $a$  value range for  $HOA_{s,c}$  was set to be  $0 \leq a_{HOA_{s,c}} \leq 0.8$ , while the  $a$  value ranges  
37 of the other two constraints were kept the same as indicated in Table 2. Likewise, we only changed the  
38  $a$  value range of  $CSOA_{w,c}$  to be  $0 \leq a_{CSOA_{w,c}} \leq 0.9$ , while keeping the  $a$  value ranges of the other  
39 three constraints the same as in Table 2. Since the results of these additional bootstrap analysis are not  
40 qualitatively different from the bootstrap analysis with  $a$  value ranges in Table 2, we only present the  
41 bootstrap results with  $a$  value ranges in Table 2.



1 **Table 2** Summary of  $a$ -value range for constrained factors, criteria for  $a$ -**Table 2** Summary of  $a$  value  
 2 range for constrained factors, criteria for  $a$  value range and accepted bootstrap run selection and the  
 3 number of accepted runs from the final combined bootstrap/ $a$ -value analysis for the summer and winter  
 4 datasets.  
 5

Dataset	Constrained factor	$a$ -value range	Criteria	Accepted runs
Zurich summer	HOA <sub>S,C</sub>	$0 \leq a \leq 0.2$	1). COA <sub>S,C</sub> : $\frac{C_3H_3O^+}{C_3H_5O^+} \geq 5$ 2). InorgNit <sub>S,C</sub> : $\frac{CO_2^+}{NO^+ + NO_2^+} \leq 0.035$ 3). Base case vs. Bootstrap correlation test at confidence level = 0	764 (76.4 %)
	COA <sub>S,C</sub>	$0 \leq a \leq 0.2$		
	Inorganic nitrate (InorgNit <sub>S,C</sub> )	$0 \leq a \leq 0.5$		
Zurich winter	HOA <sub>W,C</sub>	$0 \leq a \leq 0.9$	1). CSOA <sub>W,C</sub> : $f_{mass}(\text{nicotine}) \geq 0.96$ 2). C <sub>2</sub> H <sub>4</sub> O <sub>2</sub> <sup>+</sup> intensity: LABB <sub>W,C</sub> - MABB <sub>W,C</sub> > 0 3). C <sub>6</sub> H <sub>10</sub> O <sub>5</sub> intensity: LABB <sub>W,C</sub> - MABB <sub>W,C</sub> > 0 4). Base case vs. Bootstrap correlation test at confidence level = 0	308 (30.8 %)
	COA <sub>W,C</sub>	$0 \leq a \leq 0.3$		
	Inorganic nitrate (InorgNit <sub>W,C</sub> )	$0 \leq a \leq 0.5$		
	CSOA <sub>W,C</sub>	$0 \leq a \leq 0.6$		

Formatted: Centered

Formatted: Centered

Formatted: Centered

### 3.2.3.1 cPMF results

~~Here we present final results from the cPMF analysis of the summer and winter campaigns. The final solutions are reported as the average of all accepted bootstrap/ $a$  value randomisation runs (764 for summer, 308 for winter), with uncertainties corresponding to the standard deviation. We compare the cPMF factors to their counterparts from the standalone AMS and EESI-TOF solutions, for cases where a clear factor-to-factor correspondence exists.~~

~~A complication in this analysis is that the NO<sup>+</sup> and NO<sub>2</sub><sup>+</sup> signal can result from either organic or inorganic nitrate. Ideally, all inorganic NO<sup>+</sup> and NO<sub>2</sub><sup>+</sup> would apportion to the InorgNit<sub>S,C</sub> and InorgNit<sub>W,C</sub> factors, however inspection of the solutions reveals that this is not the case, as discussed in the factor presentations (Sect. 3.2.1 and Sect. 3.2.2). Therefore, we estimate the organic and inorganic contributions to these ions by the method of Kiendler-Scharr et al. (2016), as follows:~~

$$\frac{frac_{ON,k}}{frac_{ON,k}} = \frac{(1 + R_{ON})(R_k - R_{eai})}{(1 + R_k)(R_{ON} - R_{eai})} \quad (18)$$

~~Here we apply this analysis on a factor by factor basis, where  $frac_{ON,k}$ , defined in Eq. (19a), represents the fraction of ON apportioned to the  $k$ th factor, and  $R_k$  denotes the intensity ratio of NO<sub>2</sub><sup>+</sup> to NO<sup>+</sup> in the factor profile.  $R_{eai}$  is the reference NO<sub>2</sub><sup>+</sup>/NO<sup>+</sup> ratio for inorganic nitrate, taken as that of the InorgNit<sub>W,C</sub> and InorgNit<sub>S,C</sub> reference profiles for their respective datasets.  $R_{ON}$ , defined in Eq. (19b), is the intensity ratio of NO<sub>2</sub><sup>+</sup> to NO<sup>+</sup> for organonitrate, which ranges from 0.08 to 0.20 (Boyd et al., 2015; Bruns et al., 2010; Fry et al., 2011; Fry et al., 2009; Rollins et al., 2009).~~

$$frac_{ON,k} = \frac{(f_{ON,k,NO^+} + f_{ON,k,NO_2^+})}{(f_{k,NO^+} + f_{k,NO_2^+})} \quad (19a)$$

Formatted: Normal, Level 1

$$R_{\text{ON}} = \frac{f_{\text{ON},k,\text{NO}_2^+}}{f_{\text{ON},k,\text{NO}_2^+}} \quad (19b)$$

Here  $f_{k,\text{NO}_2^+}$  and  $f_{k,\text{NO}_3^+}$  denote the total  $\text{NO}_2^+$  and  $\text{NO}_3^+$  signal, respectively in the  $k$ th factor profile, while  $f_{\text{ON},k,\text{NO}_2^+}$  and  $f_{\text{ON},k,\text{NO}_3^+}$  denote the organonitrate contribution to these ions. Because  $f_{k,\text{NO}_2^+}$  and  $f_{k,\text{NO}_3^+}$  are directly available from the factor profile,  $\text{frac}_{\text{ON},k}$  is independently calculated via Eq. (18); and  $R_{\text{ON}}$  is assumed, Eqs. (19a) and (19b) constitute a system of 2 equations with 2 unknowns, which can be solved algebraically for  $f_{\text{ON},k,\text{NO}_2^+}$  and  $f_{\text{ON},k,\text{NO}_3^+}$ , yielding:

$$f_{\text{ON},k,\text{NO}_2^+} = \frac{(R_k - R_{\text{cat}})(f_{k,\text{NO}_2^+} + f_{k,\text{NO}_3^+})}{(1 + R_k)(R_{\text{ON}} - R_{\text{cat}})} \quad (20a)$$

$$f_{\text{ON},k,\text{NO}_3^+} = \frac{(R_k - R_{\text{cat}})(f_{k,\text{NO}_2^+} + f_{k,\text{NO}_3^+})}{(1 + R_k)(R_{\text{ON}} - R_{\text{cat}})} R_{\text{ON}} \quad (20b)$$

These calculations are important not only for profile interpretation, but also for quantitative apportionment of OA. Specifically, as noted earlier, calculations of the OA contribution to the factor time series,  $(g_{t,k})_{\text{AMS}}$ , and the EESI-TOF sensitivity to a given factor,  $AS_k$ , should consider only the organic contribution to  $\text{NO}_2^+$  and  $\text{NO}_3^+$ . In this study, we estimated the contribution from organonitrates for all factors in summer and winter assuming the midpoint of the  $R_{\text{ON}}$  range ( $R_{\text{ON}} = 0.14$ ). Organonitrate contributions ( $\text{frac}_{\text{ON},k}$ ) to the total nitrate signal for each factor and the corresponding OA fraction  $\sum_j (f_{k,j})_{\text{AMS}}$  are shown in Table S1. We also include the same calculations performed assuming an  $R_{\text{ON}}$  of 0.08 or 0.20, which as discussed above constitute the lower and upper estimates from previous studies. For  $R_{\text{ON}} = 0.14$ , the  $\text{frac}_{\text{ON},k}$  for all SOAs in summer are higher than 75 %, and for winter, this fraction  $\text{frac}_{\text{ON},k}$  varies by factor from 0 to 100 %, with four factors having  $\text{frac}_{\text{ON},k} = 100$  % (SOA1<sub>w,C</sub>, MABB<sub>w,C</sub>, LABB<sub>w,C</sub> and NitOA1<sub>w,C</sub>), suggesting the  $\text{NO}_2^+$  and  $\text{NO}_3^+$  signals are strongly influenced by ON. If  $R_{\text{ON}} = 0.08$  is assumed, the estimated  $\text{frac}_{\text{ON},k}$  decreases by ~12 % for the summer SOA factors and by 10 % to 20 % for the winter SOA factors, whereas assuming  $R_{\text{ON}} = 0.20$  increases  $\text{frac}_{\text{ON},k}$  by ~15 % in the summer and 16 % in the winter OA factors. The effect of this assumption on the factor OA concentration and thus  $AS_k$  is much smaller, with all factors below ±2 % except for one wintertime SOA factor (SOA1<sub>w,C</sub>; ±6 %).

### 3.2.13.1.1 cPMF analysis: Zurich summer

Eight factors were resolved from the Zurich summer campaign: HOA<sub>s,C</sub>, COA<sub>s,C</sub>, CSOA<sub>s,C</sub>, InorgNits<sub>s,C</sub>, two daytime SOA factors (DaySOA1<sub>s,C</sub> and DaySOA2<sub>s,C</sub>), and two nighttime SOA factors (NightSOA1<sub>s,C</sub> and NightSOA2<sub>s,C</sub>). The mean time series, diurnal eyelecycles, and the mass spectra of these factors over 764 accepted runs are shown in Fig. 53, together with the time series from AMS-only PMF and/or EESI-TOF-only PMF when the corresponding standalone factor(s) exist. An estimate of campaign-average percent uncertainty in the mass concentration of each factor, calculated as the median of the standard deviation across all accepted runs, is given in Table S2. Many factor characteristics from cPMF resemble those previously discussed in detail for single-instrument AMS PMF and/or EESI-TOF PMF (Stefenelli et al., 2019); (Stefenelli et al., 2019). Therefore, only a summary discussion of these characteristics areis presented here, and we focus on new information and/or differences obtained by the cPMF analysis. Recall that factor profiles for HOA<sub>s,C</sub>, COA<sub>s,C</sub>, and InorgNits<sub>s,C</sub> are constrained as discussed above.

1 **HOA<sub>S,C</sub>** --- The AMS mass spectrum is dominated by the C<sub>n</sub>H<sub>2n+1</sub><sup>+</sup>, and C<sub>n</sub>H<sub>2n-1</sub><sup>+</sup> series, consistent with  
2 *n*-alkanes and branched alkanes (NgZhang et al., 2011a; Lanz et al., 2007; Ulbrich et al., 2009;  
3 LanzNg et al., 2007; Zhang et al., 2005; 2011a; Qi et al., 2019; Stefenelli et al., 2019). The diurnal cycle  
4 of HOA<sub>S,C</sub> has three clear peaks (see Fig. 5b3b), however, compared to HOA<sub>S,A</sub> from Stefenelli et al.  
5 (2019)Stefenelli et al. (2019), their intensities are weaker. Specifically, the morning peak intensity ratio  
6 to the evening peak intensity is almost 1 in the HOA<sub>S,A</sub> factor, whereas in HOA<sub>S,C</sub>, the morning peak is  
7 ~1/3 of the evening peak. In terms of contribution to total OA, the HOA<sub>S,A</sub> factor contributes 5.8 %  
8 (0.177 μg m<sup>-3</sup>) of the total OA, whereas in the cPMF analysis, this factor only contributes 3.1 % (0.092  
9 μg m<sup>-3</sup>) of the total OA.

10  
11 **COA<sub>S,C</sub>** --- This factor is characterised by long-chain fatty acids and alcohols, e.g., coronaric acid and/or  
12 its isomers at *m/z* 319.2 ([C<sub>18</sub>H<sub>32</sub>O<sub>3</sub>]<sup>Na</sup>), oleic acid and/or its isomers at *m/z* 305.2 ([C<sub>18</sub>H<sub>34</sub>O<sub>2</sub>]<sup>Na</sup>),  
13 and 2-oxo-tetradecanoic acid and/or its isomers at *m/z* 293.2 ([C<sub>16</sub>H<sub>30</sub>O<sub>3</sub>]<sup>Na</sup>). Similar to previous work,  
14 the AMS profile shows both alkyl fragments and slightly oxygenated ions, consistent with aliphatic  
15 acids from cooking oils (Hu et al., 2016). The AMS profile is characterised by a high ratio of C<sub>3</sub>H<sub>3</sub>O<sup>+</sup>  
16 to C<sub>3</sub>H<sub>5</sub>O<sup>+</sup> (~5 here), slightly higher than in other studies (Xu et al., 2019; Zhao et al., 2019; Sun et al.,  
17 2016a; Sun et al., 2016b; Xu et al., 2019; Zhao et al., 2019), as well as high contributions from C<sub>5</sub>H<sub>8</sub>O<sup>+</sup>,  
18 C<sub>6</sub>H<sub>10</sub>O<sup>+</sup> and C<sub>7</sub>H<sub>12</sub>O<sup>+</sup>. Both cPMF and single instrument PMF analyses yield peaks during lunch  
19 (~11:30 to 13:30) and dinner (~18:30 to 20:30). The time series of COA<sub>S,C</sub> is strongly correlated with  
20 those of the single instrument solutions, with Pearson's *r*<sup>2</sup> of 0.846 and 0.634 against COA<sub>S,A</sub> and  
21 COA<sub>S,E</sub>, respectively.

22  
23 **CSOA<sub>S,C</sub>** --- The EESI-TOF factor profile is dominated by nicotine (detected as [C<sub>10</sub>H<sub>13</sub>N<sub>2</sub>]<sup>H</sup>) at *m/z*  
24 163.12 and levoglucosan at *m/z* 185.042 ([C<sub>6</sub>H<sub>10</sub>O<sub>5</sub>]<sup>Na</sup>), which derives from pyrolysis of the cellulose  
25 present in tobacco (Falhout et al., 2006)(Talhout et al., 2006). In the AMS profile, this factor accounts  
26 for 79.3 % of the signal from C<sub>5</sub>H<sub>10</sub>N<sup>+</sup> at *m/z* 84.081, which is attributed to a fragment of *n*-methyl  
27 pyrrolidine and previously identified as a tracer for cigarette smoke (Struckmeier et al.,  
28 2016)(Struckmeier et al., 2016). The time series of CSOA<sub>S,C</sub> correlates with that of the AMS-only and  
29 EESI-TOF solutions, with *r*<sup>2</sup> of 0.922 and 0.965, respectively. The diurnal cycles from the combined  
30 and single-instrument solutions are likewise correlated, showing high concentrations at night and low  
31 concentration during daytime.

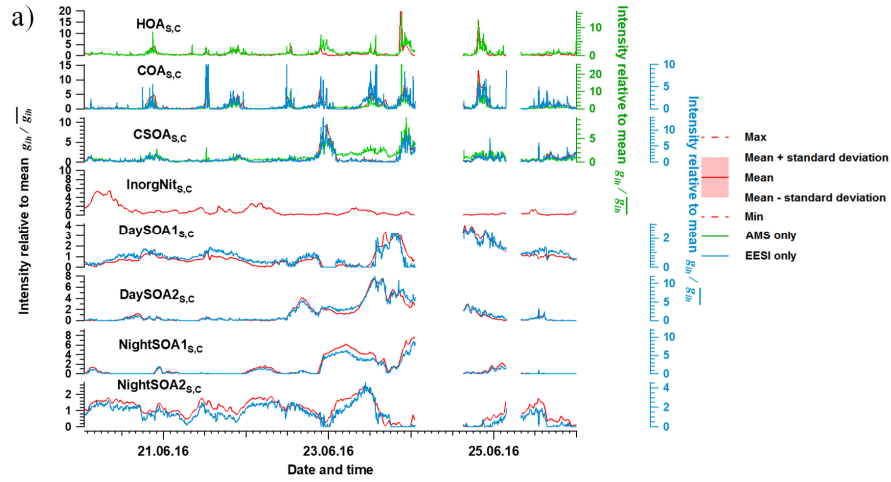
32  
33 **InorgNits<sub>S,C</sub>** --- Among the accepted bootstrap runs, the mean CO<sub>2</sub><sup>+</sup>/(NO<sup>+</sup>+NO<sub>2</sub><sup>+</sup>) ratio is 0.0346, slightly  
34 higher than the ratio of 0.0345 observed during the NH<sub>4</sub>NO<sub>3</sub> calibration period, probably due to 1)  
35 uncertainties in the constrained profile, and/or 2) a small amount of OA apportioned to this factor. The  
36 time series of this factor correlates with AMS nitrate (NO<sub>3</sub><sup>-</sup>), NO<sup>+</sup> and NO<sub>2</sub><sup>+</sup> time series, with *r*<sup>2</sup> of 0.654,  
37 0.645 and 0.956, respectively. Regarding the mass fraction, approximately 48.5 % of the NO<sup>+</sup> signal  
38 and 78.0 % of the NO<sub>2</sub><sup>+</sup> signal are apportioned to this factor, followed by the two NightSOA<sub>S,C</sub> factors.  
39 This is consistent with the overall NO<sup>+</sup> and NO<sub>2</sub><sup>+</sup> signals deriving not only from inorganic nitrate, but  
40 also from organonitrates (in other factors).

41  
42 **DaySOA1<sub>S,C</sub> and DaySOA2<sub>S,C</sub>** --- The cPMF analysis yields two SOA factors elevated during daytime,  
43 denoted DaySOA1<sub>S,C</sub> and DaySOA2<sub>S,C</sub>. The EESI-TOF spectra are similar to two factors retrieved from  
44 EESI-TOF-only PMF analysis by Stefenelli et al. (2019)Stefenelli et al. (2019), but were not resolved  
45 in AMS-only PMF, where only more- and less-oxygenated SOA factors (MO-OOA<sub>S,A</sub> and LO-OOA<sub>S,A</sub>)  
46 were obtained. These factors contain strong signatures from terpene oxidation products, e.g.,  
47 monoterpene-derived ions (C<sub>10</sub>H<sub>16</sub>O<sub>x</sub>, *x*=5, 6, 7) and sesquiterpene oxidation products (C<sub>15</sub>H<sub>24</sub>O<sub>x</sub>, *x*=3,  
48 4, 5). A detailed comparison of the two DaySOA factors from the cPMF analysis to the LO-OOA<sub>S,A</sub>

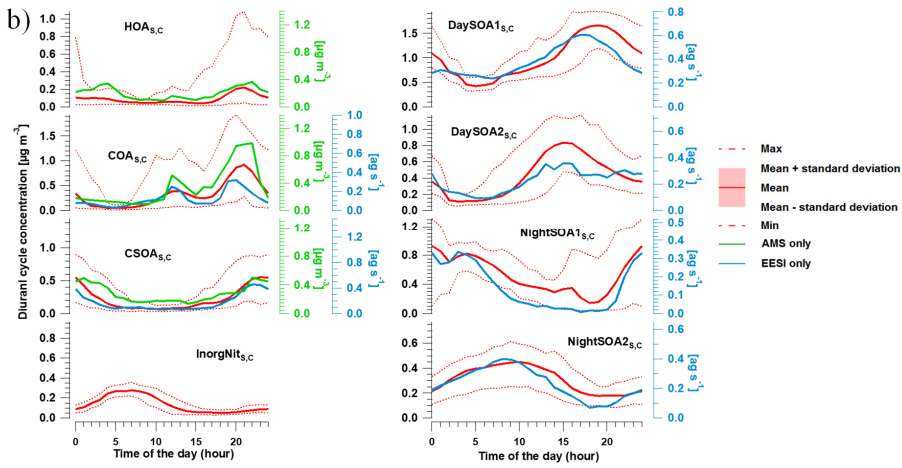
1 and MO-OOA<sub>S,A</sub> factors from AMS-only PMF is shown in Fig. S28S31, and a comparison between the  
2 two DaySOA<sub>S,C</sub> factors and DaySOA<sub>S,E</sub> factors are shown in Figs. S29S32 a) and b), respectively. The  
3 AMS ions in these two factors are characterised by a strong CO<sub>2</sub><sup>+</sup> signal, similar to the LO-OOA<sub>S,A</sub> and  
4 MO-OOA<sub>S,A</sub> factors, indicating they largely consist of oxygenated OA, consistent with the EESI-TOF  
5 spectra. We calculate *frac*<sub>ON</sub> for DaySOA1<sub>S,C</sub> and DaySOA2<sub>S,C</sub> to be 0.869 and 1.000, respectively,  
6 demonstrating that the NO<sup>+</sup> and NO<sub>2</sub><sup>+</sup> signal in these factors is dominated by organonitrates. Regarding  
7 the time series, DaySOA1<sub>S,C</sub> and DaySOA2<sub>S,C</sub> correlate strongly with DaySOA1<sub>S,E</sub> and DaySOA2<sub>S,E</sub>,  
8 with *r*<sup>2</sup> of 0.883 and 0.977, respectively. The diurnal patterns of DaySOA1<sub>S,C</sub> and DaySOA2<sub>S,C</sub> are  
9 consistent with the diurnal patterns of DaySOA1<sub>S,E</sub> and DaySOA2<sub>S,E</sub>. The diurnal patterns of both  
10 factors show an enhancement in the afternoon and the evening, which distinguish these SOAs from  
11 other SOAs: DaySOA1<sub>S,C</sub> exhibits almost a factor of 2 enhancement in signal between 15:00 and 21:00  
12 compared to the morning, whereas the DaySOA2<sub>S,C</sub> exhibits the same magnitude of enhancement in  
13 signal around 12:00 to 17:00.

14  
15 **NightSOA1<sub>S,C</sub> and NightSOA2<sub>S,C</sub>** --- We retrieve two SOA factors that are enhanced overnight and in  
16 the early morning, denoted NightSOA1<sub>S,C</sub> and NightSOA2<sub>S,C</sub>. Their factor profiles and time  
17 series/diurnals closely resemble those of NightSOA1<sub>S,E</sub> and NightSOA2<sub>S,E</sub> (see Figs. S29eS32c and  
18 S29dS32d). Similar to the DaySOA<sub>S,C</sub> factors, terpene oxidation products are evident. However, the  
19 composition is weighted towards less oxygenated and more volatile terpene oxidation products, e.g.,  
20 C<sub>10</sub>H<sub>16</sub>O<sub>2</sub> and C<sub>10</sub>H<sub>16</sub>O<sub>3</sub>, which likely partition to the particle phase at night when temperature decreases.  
21 In addition, signals consistent with monoterpene-derived organonitrates are also evident, e.g., the  
22 C<sub>10</sub>H<sub>17</sub>O<sub>6-8</sub>N and C<sub>10</sub>H<sub>15</sub>O<sub>6-9</sub>N series, which are consistent with night time oxidation of monoterpenes  
23 by NO<sub>3</sub> radicals (Xu et al., 2015; Faxon et al., 2018; Zhang et al., 2018; Xu et al., 2015). The AMS ions  
24 in these two factors are characterised by a strong CO<sub>2</sub><sup>+</sup> signal and also a relatively high NO<sup>+</sup> signal  
25 compared to *sum-Σ*DaySOA<sub>S,C</sub>. The ratio of NO<sup>+</sup>/NO<sub>2</sub><sup>+</sup>-ratio is 4.55 and 8.24 for NightSOA1<sub>S,C</sub> and  
26 NightSOA2<sub>S,C</sub>, respectively, yielding *frac*<sub>ON</sub> for NightSOA1<sub>S,C</sub> and NightSOA2<sub>S,C</sub> of 0.798 and 1,  
27 indicating high organonitrate content. These two factors correlate well with *sum-Σ*NightSOA<sub>S,E</sub>,  
28 reaching *r*<sup>2</sup> of 0.975 and 0.897, following in general the same diurnal patterns, with NightSOA1<sub>S,C</sub>  
29 peaking from 22:00 to 05:00 and NightSOA1<sub>S,C</sub> peaking from 04:00 to 12:00.

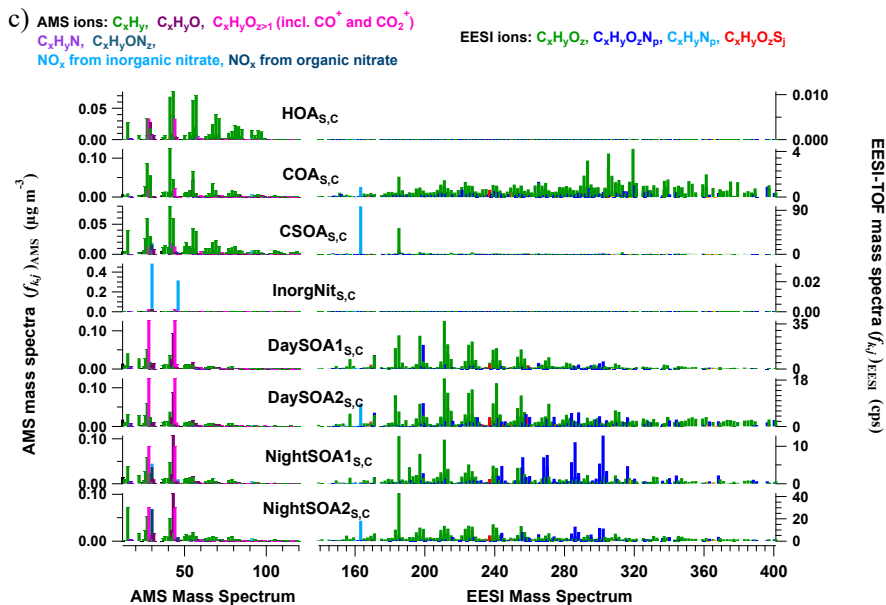
1



2



3



1  
2 Figure 3. Mean factor time series (a), diurnal cycles (b) and factor profiles (c) from the 764 accepted  
3 bootstrap runs from cPMF analysis. In a), the average factor time series are shown in red, and  
4 corresponding AMS and/or EESI-TOF factors from standalone PMF are shown in green and blue,  
5 respectively. Shaded areas represent the standard deviation across all accepted runs and are summarised  
6 in Table S2. In b), the average diurnal cycles are displayed as red solid lines. Shaded areas denote the  
7 standard deviation over the average diurnal from individual solutions over all 764 accepted runs.  
8 Dashed lines denote the maximum and minimum mean diurnal observed within these 764 runs. For  
9 comparison, the AMS and EESI-TOF PMF factor time series and diurnal cycles from the individual  
10 dataset in [Stefenelli et al. \(2019\)](#) are shown in green and blue respectively for  
11 related factors. In c), the average factor profiles are coloured by different ion families. Here, the AMS  
12 factor profiles are in the unit of  $\mu\text{g m}^{-3}$  (each factor sums to  $1 \mu\text{g m}^{-3}$ ), whereas the EESI-TOF spectra  
13 are in the unit of cps (each factor sums to the total signal derived from  $1 \mu\text{g m}^{-3}$  of the factor). Note that  
14 the  $NO^+$  and  $NO_2^+$  signal is divided into inorganic and organic contributions.

### 15 16 3.2.23.1.2 cPMF analysis: Zurich winter

17  
18 Twelve factors were resolved from cPMF analysis of the Zurich winter campaign:  $HOA_{w,c}$ ,  $COA_{w,c}$ ,  
19  $InorgNit_{w,c}$ ,  $CSOA_{w,c}$ ,  $SOA1_{w,c}$ ,  $SOA2_{w,c}$ , a more-aged biomass burning OA ( $MABB_{w,c}$ ), two less-  
20 aged biomass burning OAs ( $LABB1_{w,c}$  and  $LABB2_{w,c}$ ), two nitrogen-containing OA factors  
21 ( $NitOA1_{w,c}$  and  $NitOA2_{w,c}$ ), and a factor related to a specific local event ( $EVENT_{w,c}$ ). Because no  
22 significant chemical differences are apparent between  $LABB1_{w,c}$  and  $LABB2_{w,c}$  (see Figs. [S30S33](#) and  
23 [S34S34](#)), they are aggregated to a single  $LABB_{w,c}$  factor for presentation. Therefore, there are 11  
24 factors presented below. The average time series and mass spectra of these factors among 308 accepted  
25 runs are shown in Fig. 64. The factor profiles for  $HOA_{w,c}$ ,  $COA_{w,c}$ ,  $InorgNit_{w,c}$ , and  $CSOA_{w,c}$  are  
26 constrained as described previously. Similar to the summer dataset, uncertainties in the factor mass  
27 concentrations are summarised in Table S2.

Formatted: Font: Times New Roman



1 **HOA<sub>w,c</sub>** --- This factor ~~has a qualitatively a profile similar to~~ is dominated by the summer  
2 campaign, ~~C<sub>n</sub>H<sub>2n+1</sub><sup>+</sup>, and the discussion of C<sub>n</sub>H<sub>2n-1</sub><sup>+</sup> series, consistent with *n*-alkanes and branched alkanes,~~  
3 ~~with lower CO<sup>+</sup> and CO<sub>2</sub><sup>+</sup> content than~~ the HOA<sub>s,c</sub> profile applies here as well. The HOA<sub>w,c</sub> time series  
4 correlates strongly with HOA<sub>w,A</sub> (*r*<sup>2</sup> of 0.913).

5 **COA<sub>w,c</sub>** --- The COA<sub>w,c</sub> profile is characterised by long-chain fatty acids and alcohols e.g., coronaric  
6 acid and/or its isomers at *m/z* 319.2 ([C<sub>18</sub>H<sub>32</sub>O<sub>3</sub>]<sup>+</sup>Na<sup>+</sup>), oleic acid and/or its isomers at *m/z* 305.2  
7 ([C<sub>18</sub>H<sub>34</sub>O<sub>2</sub>]<sup>+</sup>Na<sup>+</sup>), and 2-oxo-tetradecanoic acid and/or its isomers at *m/z* 293.2 ([C<sub>16</sub>H<sub>30</sub>O<sub>3</sub>]<sup>+</sup>Na<sup>+</sup>), and in  
8 the AMS, a combination of alkyl fragments and slightly oxygenated ions from aliphatic acids from  
9 cooking oils, including C<sub>5</sub>H<sub>8</sub>O<sup>+</sup>, C<sub>6</sub>H<sub>10</sub>O<sup>+</sup> and C<sub>7</sub>H<sub>12</sub>O<sup>+</sup>. These are key features ~~are consistent with~~  
10 ~~features of the constrained reference profile (0 < *a* < 0.3) (Qi et al., 2019) and COA factors found by~~  
11 other studies (Qi et al., 2019; Stefenelli et al., 2019; Tong et al., 2021). The COA<sub>w,c</sub> time series  
12 correlates with the corresponding single instrument analyses, exhibiting *r*<sup>2</sup> of 0.894, and 0.798, with  
13 COA<sub>w,A</sub> and COA<sub>w,E</sub>, respectively.

14 **InorgNit<sub>w,c</sub>** --- As noted in Sect. 3.1 Text S2.2, the NO<sup>+</sup>/NO<sub>2</sub><sup>+</sup> ratio of this factor (2.42) is higher than  
15 that of pure NH<sub>4</sub>NO<sub>3</sub> measured onsite (1.58), consistent with the presence of other inorganic nitrate  
16 sources such as KNO<sub>3</sub>. Also, the mean CO<sub>2</sub><sup>+</sup>/(NO<sup>+</sup>+NO<sub>2</sub><sup>+</sup>) ratio is 0.0371, higher than the ratio of 0.0261  
17 from the constructed InorgNit<sub>w,c</sub> profile, probably due to 1) uncertainties in the constrained profile,  
18 and/or 2) a small amount of OA apportioned to this factor. The time series of this factor shows high  
19 correlations with the AMS nitrate (NO<sub>3</sub><sup>-</sup>), NO<sup>+</sup> and NO<sub>2</sub><sup>+</sup> time series, with *r*<sup>2</sup> of 0.739, 0.792 and 0.754,  
20 respectively. Regarding the mass fraction, only 13.7% of the NO<sup>+</sup> signal and 13.2 % of the NO<sub>2</sub><sup>+</sup> signal  
21 are apportioned to this factor. The considerable fractions of the NO<sup>+</sup> and NO<sub>2</sub><sup>+</sup> signal from inorganic  
22 nitrate and organonitrates in other factors are estimated as discussed above (Kiendler-Scharr et al., 2016)  
23 and will be interpreted later for the relevant factors (as summarised in Table S1).

24  
25 **CSOA<sub>w,c</sub>** --- Similar to CSOA<sub>s,c</sub>, nicotine at *m/z* 163.12 and levoglucosan at *m/z* 185.042 were found  
26 to be the two highest peaks in the EESI-TOF mass spectra, contributing 8.75 % and 4.56 % of the EESI-  
27 TOF signal. The time series of this factor resolved from cPMF analysis correlates with CSOA<sub>w,E</sub> (*r*<sup>2</sup> =  
28 0.662). Similar to CSOA<sub>w,c</sub>, the fragment of cigarette smoke tracer *n*-methyl pyrrolidine C<sub>5</sub>H<sub>10</sub>N<sup>+</sup> at  
29 *m/z* 84.081 is also found here. This is a minor factor, comprising 2.4 % of OA.

30  
31 **SOA1<sub>w,c</sub> and SOA2<sub>w,c</sub>** --- these two factors have ~~qualitatively similar spectra but~~ different temporal  
32 patterns. SOA1<sub>w,c</sub> decreased gradually from 26 to 30 January, whereas SOA2<sub>w,c</sub> increased from 26  
33 January and fluctuated at high level from 28 to 31 January and then decreased from 1 February on.  
34 From the AMS perspective, both factors are characterised by high NO<sup>+</sup>, NO<sub>2</sub><sup>+</sup> and CO<sub>2</sub><sup>+</sup> signal compared  
35 to other organic ions. Organonitrates account for all NO<sup>+</sup> and NO<sub>2</sub><sup>+</sup> signals in SOA1<sub>w,c</sub>, but contribute  
36 nothing in SOA2<sub>w,c</sub>. Aside from the NO<sup>+</sup> and NO<sub>2</sub><sup>+</sup> ions, these AMS spectra are similar to the profiles  
37 of MO-OOA<sub>w,A</sub> and LO-OOA<sub>w,A</sub> which are characterised by high CO<sub>2</sub><sup>+</sup> signal. Major ions in the EESI-  
38 TOF profile include C<sub>10</sub>H<sub>16</sub>O<sub>x</sub> (*x* = 3, 4, 5), C<sub>9</sub>H<sub>14</sub>O<sub>x</sub> (*x* = 3, 4), C<sub>8</sub>H<sub>12</sub>O<sub>x</sub> (*x* = 4, 5), C<sub>10</sub>H<sub>18</sub>O<sub>4</sub>, and  
39 C<sub>10</sub>H<sub>14</sub>O<sub>5</sub>, which are also found in secondary biomass burning (three MABB<sub>w,E</sub> factors) and/or terpene  
40 oxidation factors (SOA1<sub>w,E</sub> and SOA2<sub>w,E</sub>) from Qi et al. (2019). However, the H:C ratio of these two  
41 factors from the EESI-TOF component (1.578 and 1.588 for SOA1<sub>w,c</sub> and SOA2<sub>w,c</sub>, respectively) is  
42 less than that of DaySOA1<sub>s,c</sub> (1.650) and DaySOA2<sub>s,c</sub> (1.672), suggesting an increased contribution  
43 from aromatic precursors.

44  
45 **Biomass burning factors (LABB<sub>w,c</sub> and MABB<sub>w,c</sub>)** --- We resolve a less-aged biomass burning  
46 factor (LABB<sub>w,c</sub>, which, as mentioned above, is the aggregate of two similar LABB factors), and a

Formatted: English (United States)

Formatted: English (United States)

Formatted: English (United States)

Formatted: English (United States)

Formatted: English (United States)

1 more-aged biomass burning factor (MABB<sub>w,c</sub>). Consistent with Qi et al. (2019), the EESI-TOF  
2 component of LABB<sub>w,c</sub> is characterised by a large signal from [C<sub>6</sub>H<sub>10</sub>O<sub>5</sub>]Na<sup>+</sup> (mainly levoglucosan)  
3 (20.4 %), and MABB<sub>w,c</sub> by a smaller but notably non-zero one (6.21 %). In addition, 76.7 % and 11.9 %  
4 of the total levoglucosan signal is apportioned to LABB<sub>w,c</sub>, and MABB<sub>w,c</sub>, respectively. The difference  
5 in the fraction of total levoglucosan apportioned to these two factors suggests different degrees of ageing  
6 of biomass burning-emitted OA. The AMS spectrum of the BBOA<sub>w,A</sub> factor is characterised by  
7 C<sub>2</sub>H<sub>4</sub>O<sub>2</sub><sup>+</sup> and C<sub>3</sub>H<sub>5</sub>O<sub>2</sub><sup>+</sup>, which are typical fragments of anhydrosugars, such as levoglucosan (Alfarra et  
8 al., 2007; Lanz et al., 2007; Sun et al., 2011). These ions are also present in LABB<sub>w,c</sub> and MABB<sub>w,c</sub>  
9 and are higher in LABB<sub>w,c</sub> (1.91 % vs 0.879 % for C<sub>2</sub>H<sub>4</sub>O<sub>2</sub><sup>+</sup> and 0.978 % vs 0.323 % for C<sub>3</sub>H<sub>5</sub>O<sub>2</sub><sup>+</sup>). In  
10 addition, the ratio of C<sub>2</sub>H<sub>4</sub>O<sub>2</sub><sup>+</sup> to CO<sub>2</sub><sup>+</sup> is 0.396 and 0.092 for LABB<sub>w,c</sub> and MABB<sub>w,c</sub>, respectively,  
11 supporting the separation of these factors based on different degrees of ageing.  
12

13 **EVENT<sub>w,c</sub>** --- This factor is low throughout the campaign except for the nights of 28 and 29 January  
14 from 00.00 to 07.00 UTC+2, where large peaks are observed. Therefore, it likely corresponds to a  
15 specific event near the sampling location. The mass spectrum features ions at *m/z* 174.08, 185.04 and  
16 195.06, tentatively assigned to [C<sub>8</sub>H<sub>11</sub>N<sub>2</sub>O]Na<sup>+</sup>, [C<sub>6</sub>H<sub>10</sub>O<sub>5</sub>]Na<sup>+</sup> and [C<sub>8</sub>H<sub>12</sub>O<sub>4</sub>]Na<sup>+</sup> from the EESI-TOF  
17 part and at *m/z* 15.024 (CH<sub>3</sub><sup>+</sup>), 27.027 (C<sub>2</sub>H<sub>3</sub><sup>+</sup>), 31.018 (CH<sub>3</sub>O<sup>+</sup>), and 43.018 (C<sub>2</sub>H<sub>3</sub>O<sup>+</sup>) from the AMS  
18 part. Qi et al. (2019) observed a very similar factor in standalone EESI-TOF PMF, which was tentatively  
19 attributed to the Zurich gaming festival and/or plastic burning in a nearby restaurant. The factor includes  
20 large contributions from C<sub>8</sub>H<sub>12</sub>O<sub>4</sub>, which likely represents 1,2-cyclohexane dicarboxylic acid diisononyl  
21 ester, a plasticiser for the manufacture of food packaging. In the AMS spectrum, large signals from NO<sup>+</sup>  
22 (7.36%) and NO<sub>2</sub><sup>+</sup> (2.03 %) are also observed, with 46.6 % of the NO<sup>+</sup> signal and 23.6% of the NO<sub>2</sub><sup>+</sup>  
23 signal assigned to organonitrates. Similar to Qi et al. (2019), the AMS spectrum is also dominated by  
24 the ions in the C<sub>x</sub>H<sub>y</sub>O<sub>z</sub><sup>+</sup> group.

25  
26 **NitOA1<sub>w,c</sub>**--- this factor is characterised by a high signal of C<sub>5</sub>H<sub>10</sub>N<sup>+</sup> at *m/z* 84.081, contributing 4.02 %  
27 to the AMS intensity in this factor (no other factor exceeds 0.16 %) while 97.0 % of the C<sub>5</sub>H<sub>10</sub>N<sup>+</sup> mass  
28 is apportioned to this factor. This ion is considered to be a tracer of cigarette smoking (Struckmeier et  
29 al., 2016)(Struckmeier et al., 2016), however, different from typical CSOA mass spectra, this factor  
30 also has high signal from CO<sub>2</sub><sup>+</sup>, suggesting a contribution from secondary formation processes. Similar  
31 to other OA factors, this factor also has a considerable fraction of NO<sup>+</sup> and NO<sub>2</sub><sup>+</sup> signal, attributed  
32 entirely to organonitrates. For the EESI-TOF component, this factor is characterised by [C<sub>8</sub>H<sub>11</sub>N<sub>2</sub>O]Na<sup>+</sup>,  
33 levoglucosan and [C<sub>8</sub>H<sub>11</sub>N<sub>2</sub>O]Na<sup>+</sup>, [C<sub>6</sub>H<sub>10</sub>O<sub>5</sub>]Na<sup>+</sup> and [C<sub>9</sub>H<sub>12</sub>O<sub>4</sub>]Na<sup>+</sup> and [C<sub>11</sub>H<sub>14</sub>O<sub>4</sub>]Na<sup>+</sup>, suggesting this  
34 factor may also be influenced by fresh biomass burning.  
35

36 **NitOA2<sub>w,c</sub>** --- this factor is characterised by a high fraction of total signal from the CHON group in the  
37 EESI-TOF analysis (38.5 %). Among these ions, [C<sub>7</sub>H<sub>11</sub>O<sub>6</sub>N]Na<sup>+</sup> at *m/z* 228.048, [C<sub>10</sub>H<sub>15</sub>O<sub>6</sub>N]Na<sup>+</sup> at  
38 *m/z* 268.079, and [C<sub>10</sub>H<sub>17</sub>O<sub>7</sub>N]Na<sup>+</sup> at *m/z* 286.090 are the three highest ions, contributing 1.65 %, 1.99 %,  
39 and 1.98 %, respectively. There are also some typical ions with high intensity from biomass burning  
40 ageing (Qi et al., 2019; Stefanelli et al., 2019), e.g., [C<sub>9</sub>H<sub>14</sub>O<sub>4</sub>]Na<sup>+</sup> at *m/z* 209.078, [C<sub>10</sub>H<sub>14</sub>O<sub>6</sub>]Na<sup>+</sup> at *m/z*  
41 253.068, and [C<sub>10</sub>H<sub>16</sub>O<sub>6</sub>]Na<sup>+</sup> at *m/z* 255.084, contributing 6.47 %, 2.85 %, and 4.39 %, respectively.  
42 This may suggest a contribution from biomass burning activities. From the AMS perspective, this factor  
43 is characterised by high NO<sup>+</sup> and NO<sub>2</sub><sup>+</sup> signal, in which all of the NO<sup>+</sup> and NO<sub>2</sub><sup>+</sup> signals are produced  
44 from inorganic nitrates (see Table S1), with the other ions being qualitatively similar to OOA-type  
45 spectra.

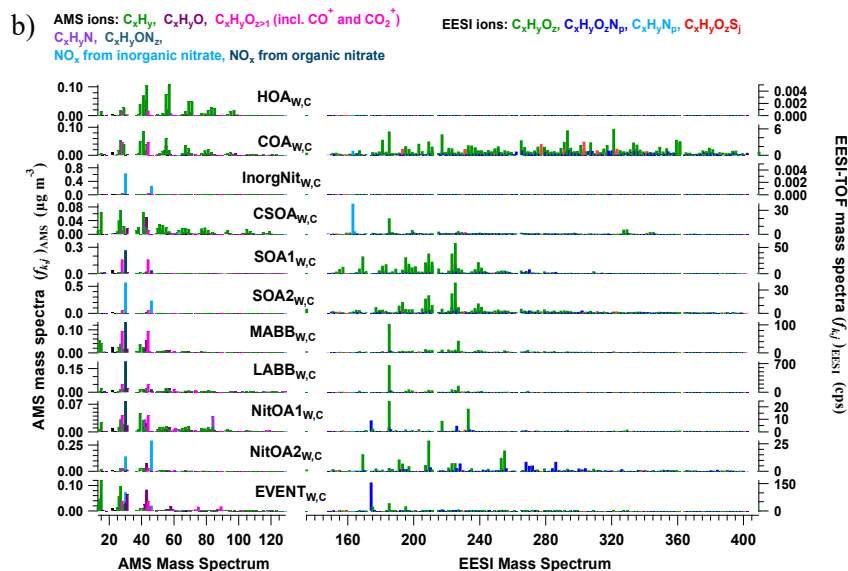
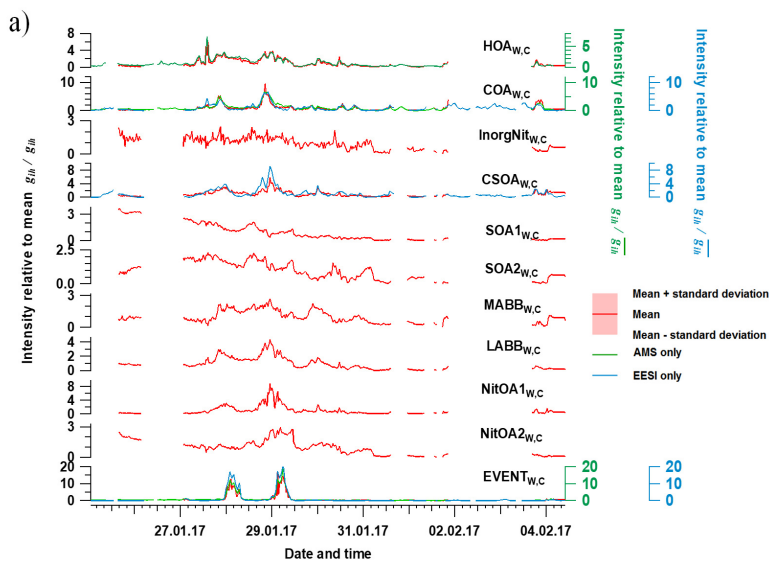


Figure 4. Average factor time series (a) and factor profiles (b), which are calculated as the mean of all accepted bootstrap runs (308 runs in total). In a), the average factor time series are shown in red, and corresponding AMS and/or EESI-TOF factors from standalone PMF are shown in green and blue, respectively. Shaded areas represent the standard deviation across all accepted runs, and are summarised in Table S2. In b), the average factor profiles are coloured by different ion families. Here, the AMS factor profiles are in the unit of  $\mu\text{g m}^{-3}$  (each factor sums to  $1 \mu\text{g m}^{-3}$ ), whereas the EESI-TOF spectra are in the unit of cps (each factor sums to total signal derived from  $1 \mu\text{g m}^{-3}$  of the factor). Note that the  $\text{NO}^+$  and  $\text{NO}_2^+$  signal is divided into inorganic and organic contributions.

### 3.3.2 EESI-TOF sensitivity to resolved factors

AMS and EESI-TOF contributions to the factor profiles are intrinsically linked by cPMF. That is, for each individual factor the two instrument profiles by definition describe the same OA fraction. Therefore, the EESI-TOF sensitivity to a factor  $AS_k$  can be calculated according to Eq. (10). Note that this calculation depends on the assumptions that (1) both instruments are well-represented in the solution; (2) the PMF solution is of high quality (i.e., factors are all meaningful and well-separated, without significant mixing or splitting); (3) solution uncertainties are not so high as to preclude quantitative interpretation of the results. Assumption (1) was discussed earlier in the context of instrument weighting, and assumption (2) is supported by the interpretability of the factors as presented in the previous section. By performing the cPMF analysis on a large number of runs combining bootstrap analysis and  $a$ -value exploration, we can estimate uncertainties in the calculated sensitivities imposed by the analysis model, as presented below, thereby addressing assumptions (2) and (3).

The datasets analysed here were taken from the first field deployments of the EESI-TOF. As a result, operational protocols were not yet fully standardised across campaigns. Specifically, we lack reliable on-site calibration with a chemical standard common to the two campaigns (this was attempted but the measurements were evaluated to be unreliable during post-analysis due to operational problems). Therefore, to enable comparison of relative factor sensitivities between the summer and winter campaigns, we select COA as a reference. That is, we assume  $AS_{COA} = AS_{COA_{s,c}} = AS_{COA_{w,c}}$ . We choose COA because it is the only factor that both (1) appears in all four single-instrument datasets (i.e., summer and winter, AMS and EESI-TOF) and (2) compared to other factors, is less likely to significantly change in composition between the campaigns (in contrast to, e.g., SOA in Zurich, which is known to have significantly different precursors in summer and winter). Therefore, all sensitivities below are reported as  $(AS_k / \overline{AS_{COA}})$ , in which  $AS_k$  is calculated in every bootstrap run, and then referenced to  $\overline{AS_{COA}}$  (the mean  $AS_{COA}$  calculated over all bootstrap runs). Here  $k$  denotes a given factor from the (summer or winter) cPMF solutions. Note that EESI-TOF sensitivities to HOA and InorgNit are not discussed here, since they are undetectable by the EESI-TOF (as configured for these campaigns; see Sect. 2.2.2) and therefore constrained to be  $\sim 0.01$  cps / ( $\mu\text{g m}^{-3}$ ). The mean and standard deviation of factor-dependent  $AS_k / \overline{AS_{COA}}$  for the summer and winter datasets are shown in Fig. 5, with histograms summarising all accepted runs shown in Fig. S35 and Fig. S36.

For ease of viewing, the factors in Fig. 75 are collected into related groups. We also calculate the  $AS_k$ 's for several factor aggregations. First, five factors that are likely related to biomass burning (LABB<sub>w,c</sub>, MABB<sub>w,c</sub>, NitOA1<sub>w,c</sub>, NitOA2<sub>w,c</sub> and EVENT<sub>w,c</sub>), are denoted as the “Sum-ΣBB” factor. Additionally, we separately aggregate the two DaySOA<sub>s,c</sub> and two NightSOA<sub>s,c</sub> factors, denoted “sum-ΣDaySOA<sub>s,c</sub>” and “sum-ΣNightSOA<sub>s,c</sub>”, respectively. As seen in Fig. 5 (as well as Fig. S34 in Figs. S35 and S36 and Table S3), the relative uncertainty from the summer factors is systematically lower than for the winter factors within the accepted solutions. This may indicate higher source apportionment quality and solution stability for the former, but is also related to the sub-division of factors related to primary biomass burning-related factors, as discussed later.

For COA<sub>s,c</sub> and COA<sub>w,c</sub>, the mean relative sensitivities are 1 by definition, though uncertainties are still calculated due to non-zero  $a$ -values, while the reference profile utilised for CSOA<sub>w,c</sub>, ensures that CSOA<sub>w,c</sub> CSOA<sub>s,c</sub> will have similar sensitivities. Interestingly, the distribution of the sensitivities of COA<sub>s,c</sub>, COA<sub>w,c</sub>, and CSOA<sub>w,c</sub> in Figs. S32 and Fig. S33 is clearly multi-modal despite  $a$ -value constraints, (although the overall COA<sub>s,c</sub> and COA<sub>w,c</sub> distributions remain relatively narrow), but the reason for this remains to be explored is unknown.

Formatted: English (United States)

Formatted: English (United States)

Formatted: English (United States)

Formatted: English (United States)

Formatted: English (United States)

Formatted: English (United States)

Formatted: English (United States)

1 The next group of factors (LABB<sub>w,c</sub>, MABB<sub>w,c</sub>, NitOA1<sub>w,c</sub>, NitOA2<sub>w,c</sub> and EVENT<sub>w,c</sub>) includes non-  
2 negligible contributions from levoglucosan (C<sub>6</sub>H<sub>10</sub>O<sub>5</sub>), produced typically from biomass-burning(BB)-  
3 related activities. Previous work has demonstrated that the EESI-TOF sensitivity to levoglucosan is  
4 higher than that of many other compounds and bulk SOA from representative precursors (Lopez-  
5 Hilfiker et al., 2019; Brown et al., 2021). Indeed, although the set of studied compounds is far from  
6 comprehensive, the relative sensitivity of the EESI-TOF to levoglucosan is among the highest yet  
7 recorded. Therefore, ~~although despite the variation in composition of the POA-influenced factors varies~~  
8 ~~considerably, it is possible that, the levoglucosan effect of the C<sub>6</sub>H<sub>10</sub>O<sub>5</sub> content may have significant~~  
9 ~~predictive value with respect to on the overall factor sensitivity; is often considerable for cases where~~  
10 ~~this ion is strongly influenced by levoglucosan.~~ Figure 6 shows  $AS_k$  as a function of the C<sub>6</sub>H<sub>10</sub>O<sub>5</sub> fraction  
11 for all factors for which the C<sub>6</sub>H<sub>10</sub>O<sub>5</sub> signal is believed to result largely from levoglucosan. This analysis  
12 accounts for all factors resolved from the cPMF of the winter dataset except CSOA<sub>w,c</sub>, because  
13 CSOA<sub>w,c</sub> is dominated by the signal from the protonated nicotine ([C<sub>10</sub>H<sub>14</sub>N<sub>2</sub>]H<sup>+</sup>) ion, which is both  
14 chemically different (reduced nitrogen) and has a different ionisation pathway than other measured ions.  
15 The four summer SOA factors are excluded as well, because the contribution from C<sub>6</sub>H<sub>10</sub>O<sub>5</sub> in these  
16 factors was previously attributed to terpene and/or aromatic oxidation products (Stefenelli et al.,  
17 2019)(Stefenelli et al., 2019). An obvious qualitative trend of increasing sensitivity with increasing  
18 levoglucosan fraction is evident with Pearson  $r^2$  of 0.676, indicating the overwhelming influence of the  
19 high sensitivity species levoglucosan on the factor apparent sensitivity.

20 For the primary BB-related factors, the uncertainties are generally higher than for the other factors (see  
21 Fig. S33 and Fig. S34bS36). In contrast, the aggregated BB factor (~~Sum-Σ~~BB<sub>w,c</sub>, and ~~Sum-Σ~~BB<sub>w,c</sub> =  
22 MABB<sub>w,c</sub> + LABB<sub>w,c</sub> + NitOA1<sub>w,c</sub> + NitOA2<sub>w,c</sub> + EVENT<sub>w,c</sub>) is less uncertain and has a narrower  
23 sensitivity distribution. This suggests that the overall classification of signal as biomass burning-related  
24 is robust, but the subdivision into more specific BB-related sources carries higher uncertainties.  
25 Likewise, the relative sensitivities of ~~sum-Σ~~DaySOAs<sub>s,c</sub> and ~~sum-Σ~~NightSOAs<sub>s,c</sub> are less uncertain  
26 compared to individual corresponding SOA factors in summer (as shown in Fig. S32 and Fig. S34aS35).  
27 This contrast suggests that coarse classifications of factors may have higher precision, but provide less  
28 information, whereas fine classifications of factors may have higher uncertainties, but potentially  
29 provide more information from each factor. It also suggests that, at least for these datasets, factor mixing  
30 occurs primarily between factors with closely related sources. Despite their higher uncertainties, the  
31 finest classification levels explored here still appear to be meaningful. We also note that both datasets  
32 investigated here are of relatively short duration, and factor separation may improve in longer datasets.

33 The final group of factors in Fig. 75 corresponds to SOA. The relative sensitivities of the SOA factors  
34 in winter are shown to be lower than any of the SOA factors resolved during summer. This is consistent  
35 with expectations regarding the seasonal differences in the dominant SOA precursors and the expected  
36  $AS_k$  of the resulting SOA. At this site, SOA precursors are expected to be dominated by monoterpenes  
37 in summer, and biomass burning (increasing the contribution of phenols, naphthalenes, and other  
38 aromatics) in winter, with traffic making a lesser contribution in both seasons (Daellenbach et al., 2016;  
39 Qi et al., 2020). This is supported by analysis of the characteristics of the retrieved factors as discussed  
40 above (Qi et al., 2019; Stefenelli et al., 2019). Previous studies have shown differences in the EESI-  
41 TOF bulk sensitivity to SOA from different precursors, with terpene-derived SOA generally exhibiting  
42 higher sensitivity than SOA from light aromatics (Lopez-Hilfiker et al., 2019; Wang et al., 2021). Figure  
43 7 shows the  $AS/\overline{AS}_{COA}$  for two DaySOAs<sub>s,c</sub> and NightSOAs<sub>s,c</sub> factors in summer, as well as the  
44 ~~sum-Σ~~DaySOAs<sub>s,c</sub> and ~~sum-Σ~~NightSOAs<sub>s,c</sub>, which are the aggregates of the individual DaySOAs<sub>s,c</sub>  
45 and NightSOAs<sub>s,c</sub> factors (~~sum-Σ~~DaySOAs<sub>s,c</sub> = DaySOA1<sub>s,c</sub> + DaySOA2<sub>s,c</sub>; and  
46 ~~sum-Σ~~NightSOAs<sub>s,c</sub> = NightSOA1<sub>s,c</sub> + NightSOA2<sub>s,c</sub>), respectively, and two SOA<sub>w,c</sub> factors in winter

Formatted: English (United States)

Formatted: English (United States)

Formatted: English (United States)

Formatted: English (United States)

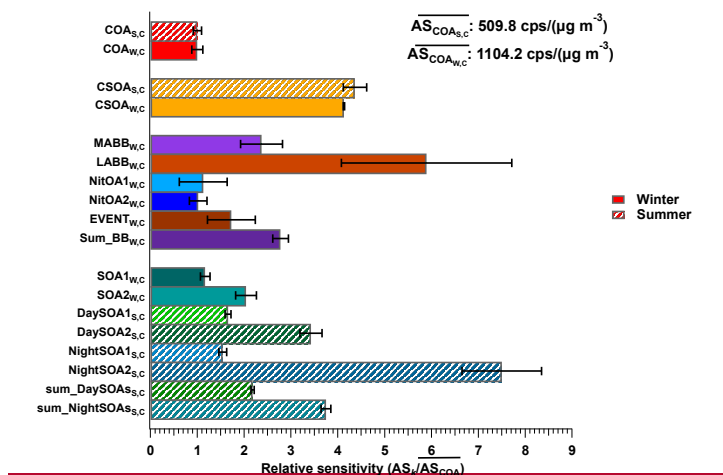
Formatted: English (United States)

Formatted: English (United States)

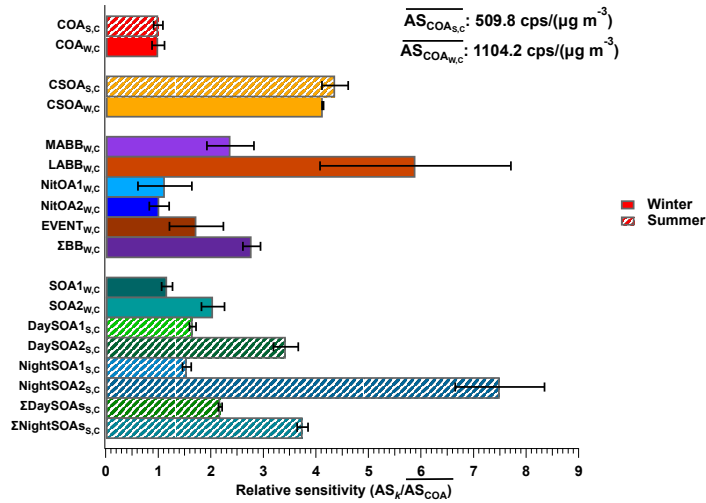
Formatted: English (United States)

1 as a function of their H:C ratio calculated from the EESI-TOF component. A trend of increasing  
 2 sensitivity with increasing H:C ratio is observed for the summer SOAs, ~~as well as the winter SOAs~~  
 3 ~~(SOA1<sub>w,c</sub> and SOA2<sub>w,c</sub>)~~ and winter SOAs (SOA1<sub>w,c</sub> and SOA2<sub>w,c</sub>), with an overall Spearman's rank  
 4 correlation of 0.833. Consistent with Wang et al. (2021), H:C is found to be a better predictor of  $AS_k$   
 5 than either O:C or OSc, yielding Spearman's rank correlation of 0.833 for  $AS_k$  vs. H:C, -0.167 for  $AS_k$   
 6 vs. O:C, and -0.452 for  $AS_k$  vs. OSc (Fig. S37a and Fig. S37b).

7 For the SOA factors, we compare  $AS_k$  retrieved to  $AS_k$  predicted using a molecular formula-based  
 8 parameterisation trained with laboratory SOA measurements, as described in Sect. 2.2.3 (Wang et al.,  
 9 2021). No parameterisations presently exist for POA factors, so these are  
 10 excluded from the comparison, although to allow comparison between campaigns the model is used to  
 11 calculate a reference value for  $AS_{COA}$ . Figure 108 compares the  $AS_k$  values based on model predictions  
 12 against values determined from cPMF. For summer SOAs, the LMN (limonene)-based parameterisation  
 13 is applied as a surrogate for terpene oxidation products. Regarding the winter SOAs, three scenarios  
 14 (cresol, LMN and TMB) are applied, as the winter SOAs in Zurich are mainly related to oxidation of  
 15 biomass burning emissions, which include monoterpenes, phenols, naphthalenes, and other aromatics  
 16 (Rouvière et al., 2006; Bruns et al., 2016; Kelly et al., 2018; Rouvière et al., 2006). In Fig. 108, 1:1, 1:2,  
 17 1:4, and 1:8 lines are provided to guide the eye, although a 1:1 correspondence is not expected because  
 18 the models are not trained on primary COA. The figure shows a monotonic increase in model sensitivity  
 19 predictions with increasing cPMF-derived sensitivities, with the sole exception of SOA2<sub>w,c</sub>.  
 20 Specifically, the summer-derived points fall mainly between the 1:1 and 1:2 lines, while for SOA1<sub>w,c</sub>,  
 21 the model predictions are roughly a factor of 2 lower relative to the cPMF results. This offset may  
 22 reflect differences in the appropriateness of the selected precursor surrogate. The SOA2<sub>w,c</sub> factor is a  
 23 slight outlier, probably because the  $AS_k$  for this factor is more uncertain than the others (and not fully  
 24 captured by the error bars in Fig. 75) due to the high contribution from inorganic nitrate (~80 % of mass)  
 25 in its factor profile. Given the limitations of the multi-variate parameterisation (see Sect. 2.2.3) and the  
 26 several orders of magnitude variation in EESI-TOF sensitivities to individual compounds, the  
 27 qualitative agreement between  $AS_k$  values independently retrieved from multivariate parameterisation  
 28 and cPMF provide support for both methods.

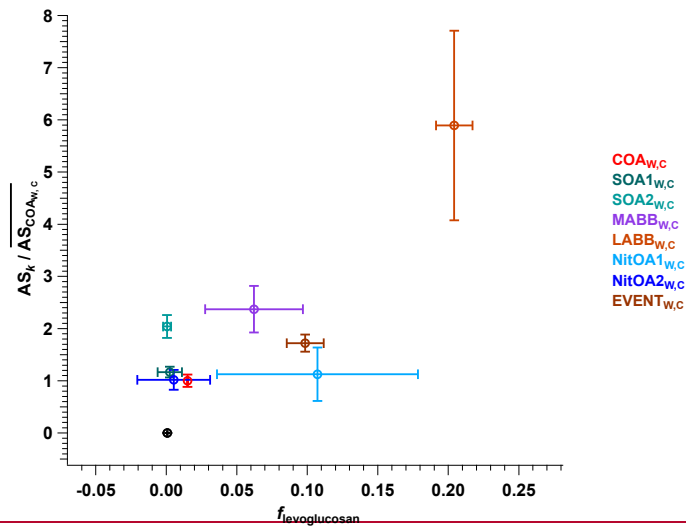


29



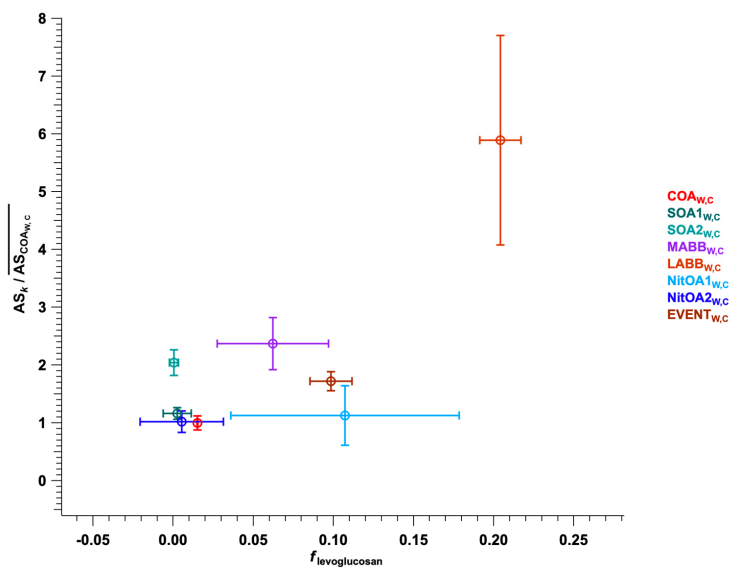
1

2 Figure 5. Comparison of  $AS_k / \overline{AS_{COA_c}}$  of different factors resolved from the cPMF on the summer and  
 3 winter datasets. Mean values are shown as bars, and error bars indicate the standard deviation over all  
 4 accepted bootstrap runs. The following factor aggregations are also shown:  $\sum ZBB_{w,c} = MABB_{w,c}$   
 5 +  $LABB_{w,c} + NitOA1_{w,c} + NitOA2_{w,c} + EVENT_{w,c}$ ;  $\sum DaySOAs_{s,c} = DaySOA1_{s,c} +$   
 6  $DaySOA2_{s,c}$ ; and  $\sum NightSOAs_{s,c} = NightSOA1_{s,c} + NightSOA2_{s,c}$ .

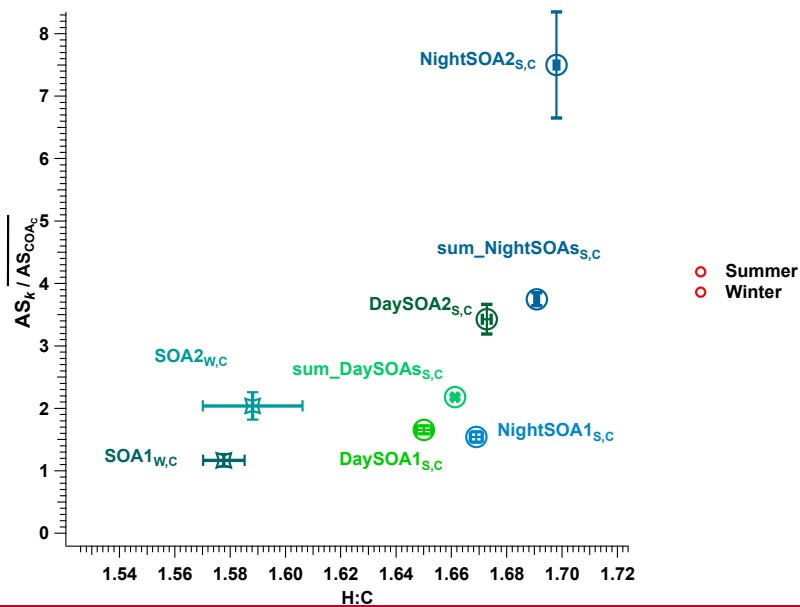


7



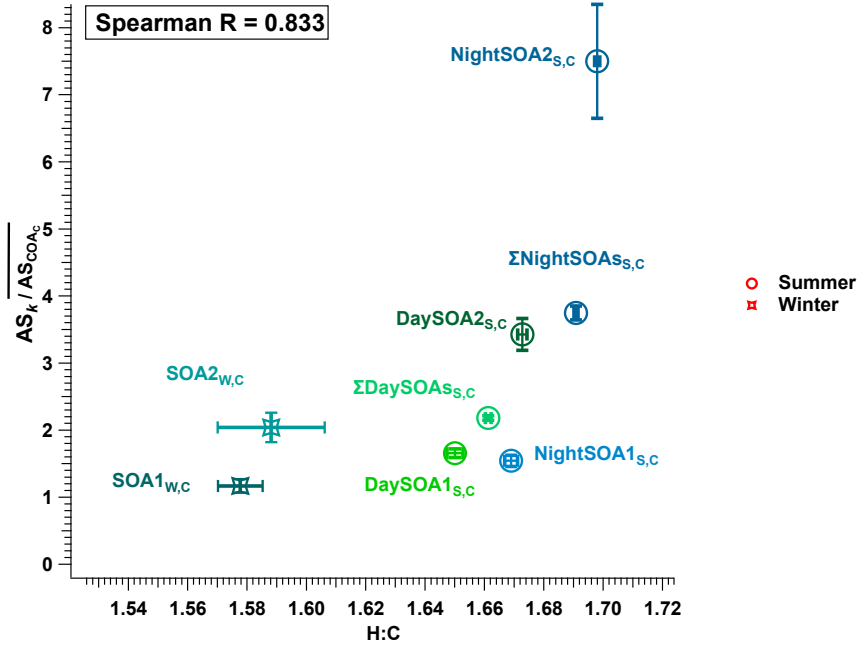


1  
 2 Figure 6. Relative apparent sensitivity  $AS_k / \overline{AS_{COA_{W,C}}}$  as a function of levoglucosan fraction for all  
 3 factors resolved from the cPMF of the winter dataset except  $COA_{W,C}$ . Error bars denote standard  
 4 deviation.



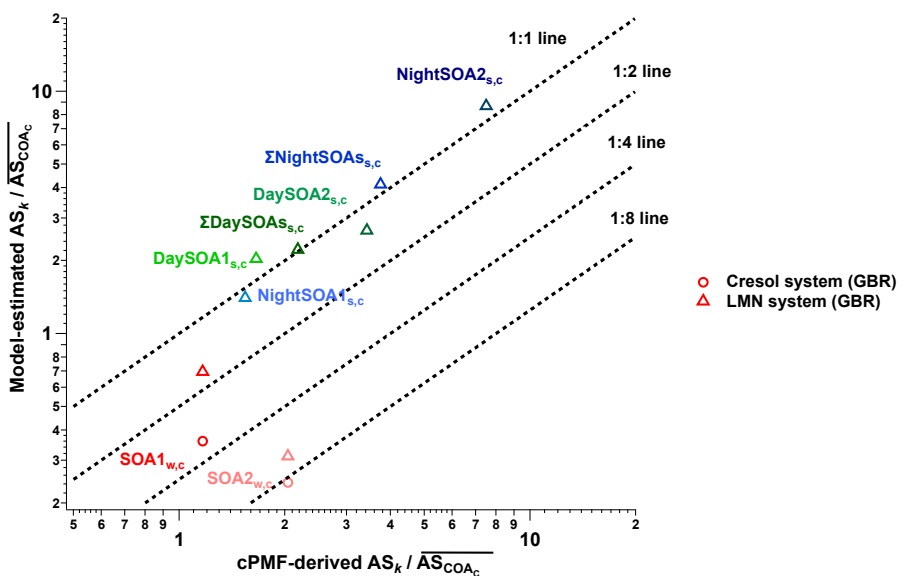
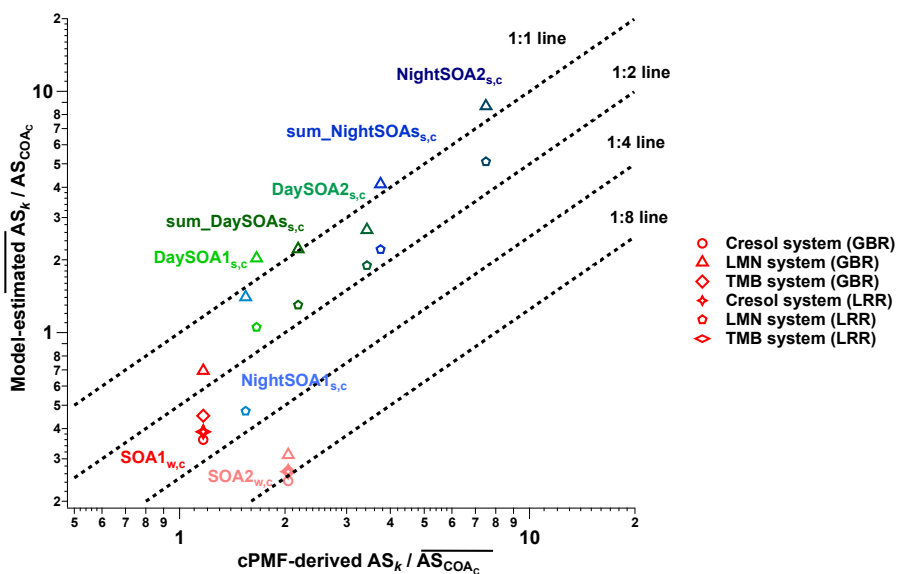
5

1



2

3 Figure 7.  $AS_k / \overline{AS_{COAc}}$  of SOA factors retrieved from the summer and winter datasets as a function of  
4 the H:C ratio. Error bars denote standard deviation across all accepted runs. Spearman correlation is  
5 0.833, as indicated in the top-left corner.



4 Figure 8. The estimated relative apparent sensitivity to COA ( $AS_k / \overline{AS_{COAc}}$ ) from the gradient boosting  
 5 regression (GBR) and linear ridge regression (LRR) models as a function of cPMF-derived  
 6  $AS_k / \overline{AS_{COAc}}$ . The symbols indicate the different oxidation-precursor system (LMN for SOA produced  
 7 from oxidation of limonene by ozone, cresol and TMB for SOA produced from oxidation of *o*-cresol  
 8 and 1,3,5-trimethylbenzene by OH radicals, respectively).

#### 4. Atmospheric implications

The application of factor-dependent sensitivities can qualitatively and quantitatively affect the source apportionment results. Figures 9a and 9b compare the source apportionment results from cPMF on the summer and winter datasets using the calculated factor sensitivities ( $AS_k$ ) (i.e., direct outputs of the cPMF analysis) vs. using a single bulk sensitivity ( $AS_{bulk}$ ) for all factors, where the latter is calculated as the ratio of the total OA measured by the EESI-TOF (cps) to that measured by the AMS ( $\mu\text{g m}^{-3}$ ). Figures 10a and 10b compare the total OA concentrations returned from the cPMF using  $AS_k$  and  $AS_{bulk}$  to the total OA measured by the AMS. Table S3 summarises the retrieved  $AS_k$  values for each factor (note that although the relative  $AS_k$  are believed to be intrinsic properties of the factors, the absolute sensitivities are instrument- and tuning-dependent, and will vary between campaigns).

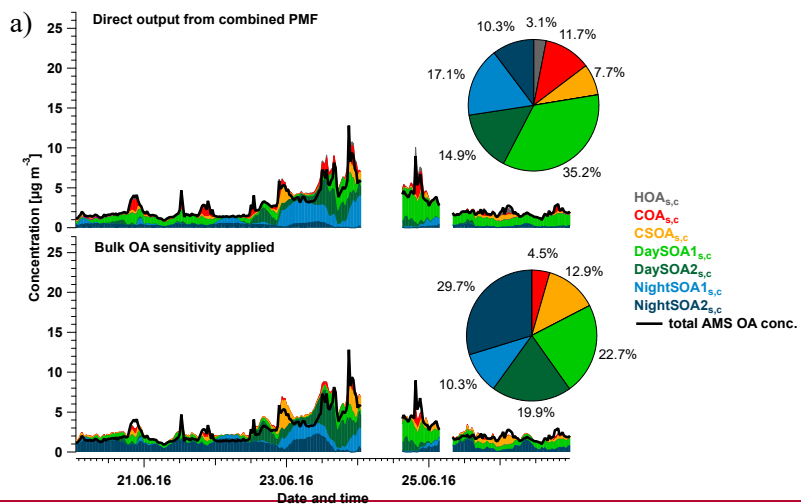
In the Zurich summer campaign, the bulk OA sensitivity  $AS_{bulk,s,c}$  ( $1254.0 \text{ cps } (\mu\text{g m}^{-3})^{-1}$ ) is higher than that of  $AS_{COA,s,c}$  ( $509.8 \text{ cps } (\mu\text{g m}^{-3})^{-1}$ ). Four factors ( $HOA_{s,c}$ ,  $COA_{s,c}$ ,  $DaySOA1_{s,c}$  and  $NightSOA1_{s,c}$ ) are underestimated, whereas three factors ( $CSOA_{s,c}$ ,  $DaySOA2_{s,c}$  and  $NightSOA2_{s,c}$ ) are overestimated when  $AS_{bulk,s,c}$  is used. Using the calculated  $AS_k$ , the contribution of  $COA_{s,c}$  to total OA more than doubles, from 4.5 % to 11.7 % as shown in Fig. 9a). Similarly, the application of  $AS_k$  increases the contributions of  $DaySOA1_{s,c}$  and  $NightSOA1_{s,c}$  from 22.7 % to 35.2 %, and from 10.3 % to 17.1 %, respectively. Among the overestimated factors, the largest decrease post-correction is found for  $NightSOA2_{s,c}$ , the contribution of which decreases by approximately a factor of three (from 29.7 % to 10.3%). Smaller post-correction decreases are observed for the contributions of  $CSOA_{s,c}$  (12.9 % to 7.7 %) and  $DaySOA2_{s,c}$  (19.9 % to 14.9 %). If factor-dependent sensitivities were ignored,  $NightSOA2_{s,c}$  would be the largest contributor to total OA, followed by  $DaySOA1_{s,c}$  whereas the full analysis indicates that  $DaySOA1_{s,c}$  is the largest contributor.

Similar to the summer campaign, application of  $AS_k$  significantly affects the source apportionment results in winter.  $CSOA_{w,c}$ ,  $MABB_{w,c}$ , and  $LABB_{w,c}$  are shown to be overestimated, while  $HOA_{w,c}$ ,  $COA_{w,c}$ ,  $SOA1_{w,c}$ ,  $NitOA1_{w,c}$ ,  $NitOA2_{w,c}$  and  $EVENT_{w,c}$  are underestimated. If factor-dependent sensitivities were not considered,  $LABB_{w,c}$  and  $MABB_{w,c}$  would appear to be the dominant contributors to total OA (35.7 % and 18.2 % respectively) due to their high levoglucosan content. However, the full cPMF analysis indicates the  $LABB_{w,c}$  and  $MABB_{w,c}$  contributions to be 14.9 % and 14.4 %, respectively, whereas accounting for  $AS_k$  increases the contribution of  $SOA1_{w,c}$  from 12.7 % to 22.0 %, making it the largest contributor.

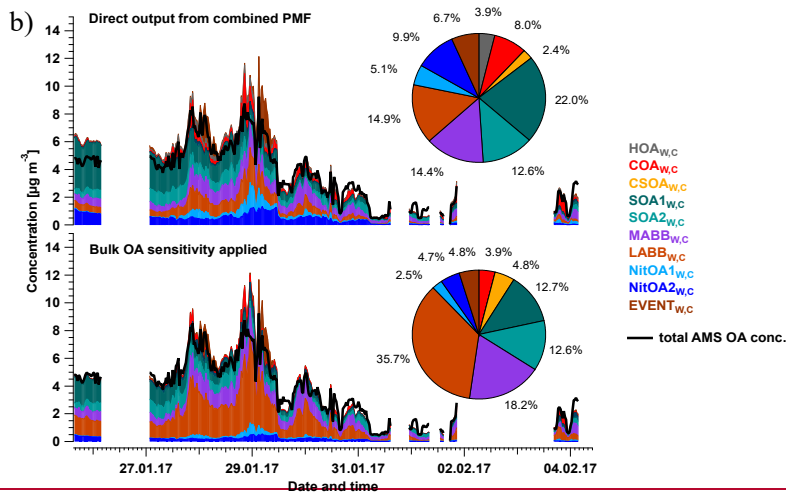
For both the summer and winter datasets, calculation of total OA from cPMF results using factor-specific  $AS_k$  significantly outperforms that using a single  $AS_{bulk}$ . This is evident from an increased  $r^2$  (0.966 vs 0.821) for summer. However, the  $r^2$  is similar between the two approaches in winter (0.947 vs 0.943). The difference after applying  $AS_k$  and  $AS_{bulk}$  in  $r^2$  might be related to the extent to which the contribution from factors with high  $AS_k$  and low  $AS_k$  to total OA changes over the time during the campaign, which can vary in different datasets.

Box-and-whisker diagrams of factor contributions to total OA with/without applying  $AS_k$  values for summer and winter are presented in Fig. 11. In the Zurich summer campaign, the box plots of the corrected contributions of all six factors fall completely outside of the interquartile range (IQR) of the uncorrected results, suggesting that the use of a single  $AS_{bulk}$  would lead to significant biases. In contrast, the winter campaign exhibits a lack of overlap between the  $AS_k$  and  $AS_{bulk}$ -derived results for eight

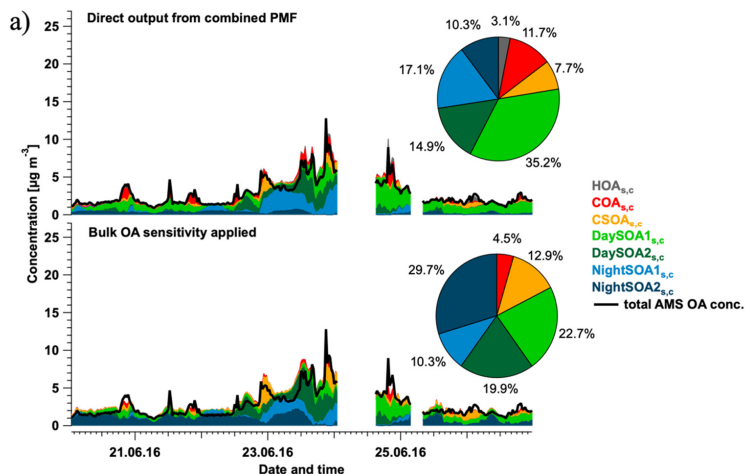
- 1 factors ( $HOA_{w,c}$ ,  $COA_{w,c}$ ,  $CSOA_{w,c}$ ,  $SOA1_{w,c}$ ,  $SOA2_{w,c}$ ,  $NitOA1_{w,c}$ ,  $NitOA2_{w,c}$  and  $EVENT_{w,c}$ ),
- 2 whereas two factors overlap ( $SOA2_{w,c}$  and  $MABB_{w,c}$ ). This may result from statistical uncertainties
- 3 in bootstrap analysis coupled with a less robust division between certain factors, yielding a wide
- 4 distribution, e.g.,  $MABB_{w,c}$ , and/or  $AS_k$  values that are similar to  $AS_{bulk}$  ( $2271.1 \text{ cps } (\mu\text{g m}^{-3})^{-1}$ ), e.g.,
- 5  $SOA2_{w,c}$  ( $2253.2 \text{ cps } (\mu\text{g m}^{-3})^{-1}$ ) and  $MABB_{w,c}$  ( $2619.0 \text{ cps } (\mu\text{g m}^{-3})^{-1}$ ).



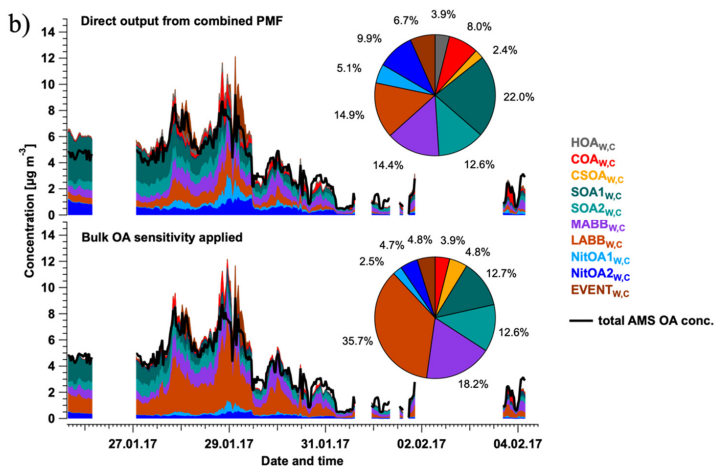
6



7

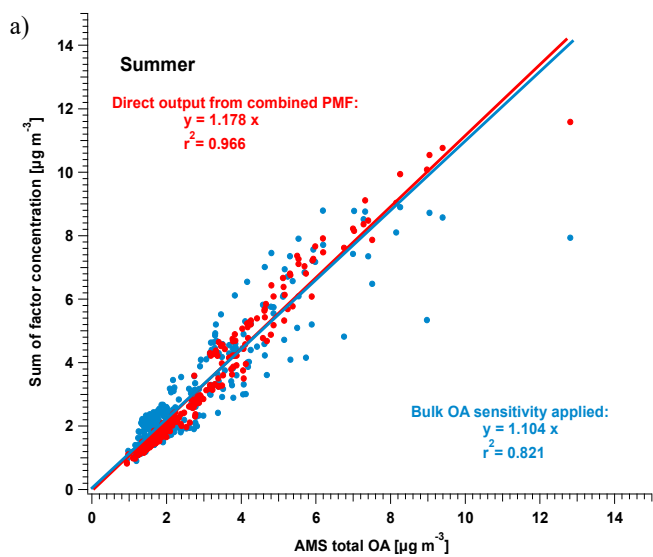


1

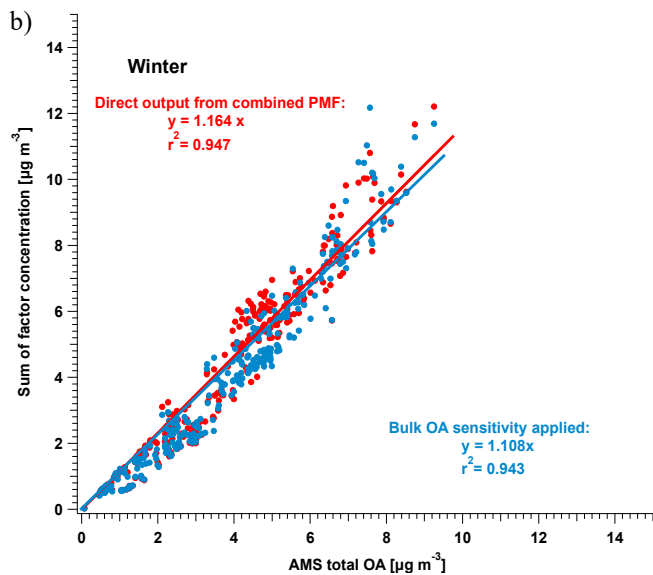


2

3 Figure 9. Comparison of source apportionment results between direct output from cPMF (i.e.,  
 4 accounting for factor-dependent sensitivities) and application of a single bulk OA sensitivity, applied  
 5 to the Zurich summer (a) and winter (b) datasets. Stack plots of factor time series directly from  
 6 combined PMF and factor time series calculated from bulk OA sensitivity compared with total AMS  
 7 OA concentration are shown in the upper and lower panel, respectively in each subfigure, together with  
 8 the corresponding factor contribution shown in the pie chart. Note that here the contribution of the  
 9 InorgNit factor and the contributions of  $\text{NO}^+$  and  $\text{NO}_2^+$  from inorganic nitrate in each factor are excluded  
 10 to account only for the total OA.



1

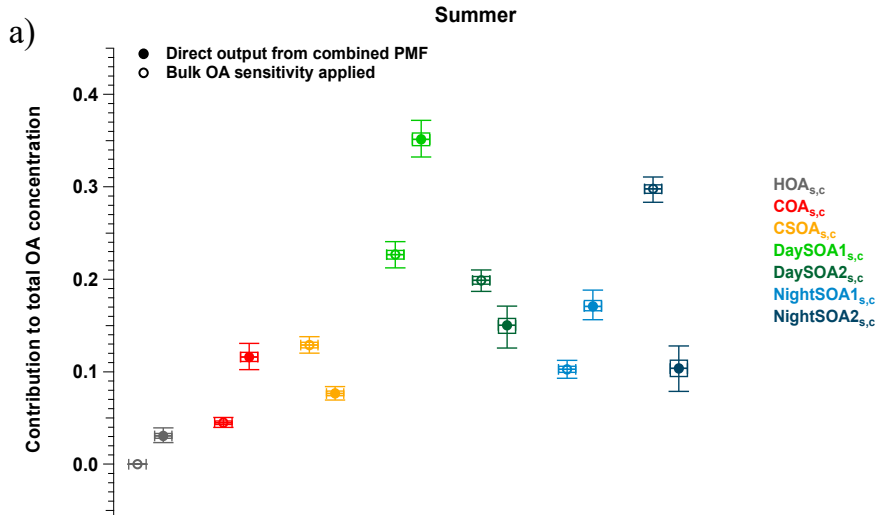


2

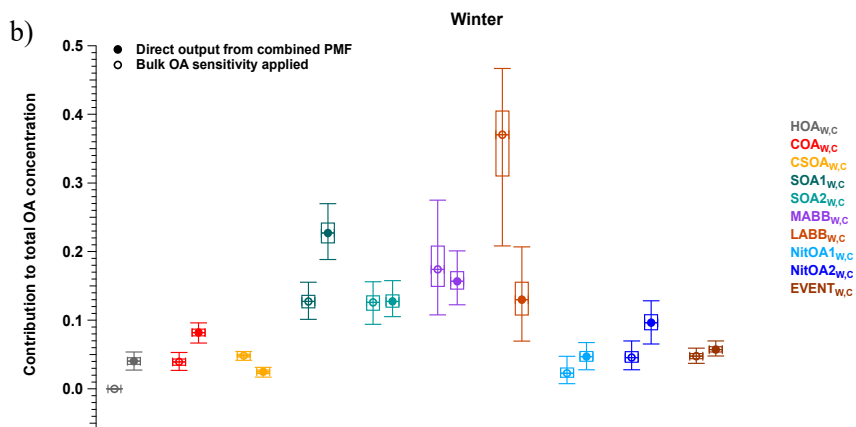
3 Figure 10. Comparison between the sum of factor concentrations in each time point with (in red) and  
 4 without (in blue) taking the factor-dependent sensitivity into account and total OA measured by AMS  
 5 for summer in a) and winter in b). A linear fit is conducted based on the Levenberg-Marquardt least  
 6 orthogonal distance method. Note that here the contribution of the InorgNit factor and the contributions  
 7 of  $\text{NO}^+$  and  $\text{NO}_2^+$  from inorganic nitrate in each factor are excluded.

8

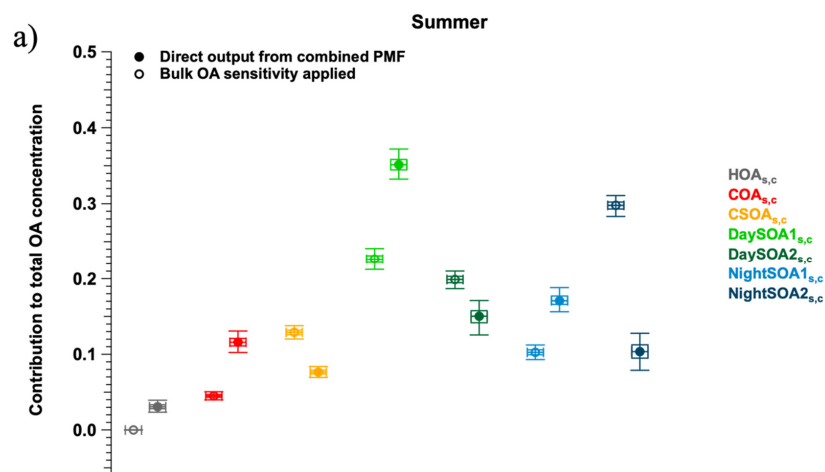




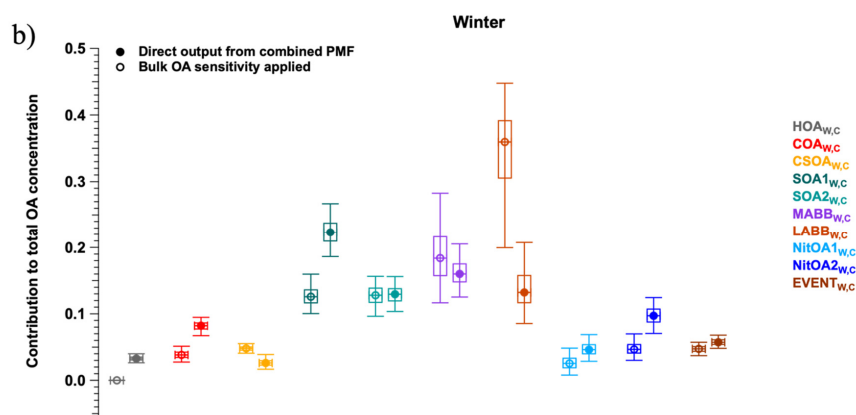
1



2  
3



1



2

3

4 Figure 11. Box-and-whisker diagrams of factor ~~contribution~~ contributions to total OA with/without  
 5 applying the factor dependent sensitivities, for summer in a) and winter in b) within accepted solutions.  
 6 For each pair of factors, the contribution without factor-dependent sensitivity applied is shown in the  
 7 left box (open symbols), whereas the contribution corrected by factor-dependent sensitivity is shown in  
 8 the right box (filled symbols). The plot box-and-whisker diagram shows the mean (open/filled circle),  
 9 median (horizontal bar), interquartile range (rectangle, the 25<sup>th</sup> percentile is the lower edge and the 75<sup>th</sup>  
 10 is the upper edge), and minimum/maximum values (whiskers). Note that here the contribution of  
 11 InorgNit factor and contribution of NO<sup>+</sup> and NO<sub>2</sub><sup>+</sup> from inorganic nitrate in each factor are excluded.  
 12

1 ~~5. Conclusion~~  
2 5. Conclusions  
3

4 We address the longstanding challenges in achieving quantitative source apportionment of SOA sources  
5 by conducting a positive matrix factorisation (PMF) analysis of a dataset combining measurements from  
6 an aerosol mass spectrometer (AMS) and an extractive electrospray ionisation time-of-flight mass  
7 spectrometer (EESI-TOF). This approach combines the strengths of the two instruments, namely the  
8 quantification ability of the AMS and the chemical resolution of the EESI-TOF. We demonstrate the  
9 utility of this approach by PMF analysis of combined EESI-TOF/AMS datasets collected during  
10 summer and winter in Zurich, Switzerland. The results retain the chemical resolution of the standalone  
11 EESI-TOF PMF, while additionally providing quantitative factor time series and the EESI-TOF bulk  
12 sensitivity to different OA factors.

13 ~~We present a general procedure to conduct source apportionment on a combined dataset, including a  
14 new metric for ensuring both instruments are well-represented in the solution, a method for optionally  
15 constraining factor profiles for one or both instruments, and a protocol for uncertainty analysis. The  
16 balancing metric references residual distributions obtained from cPMF to those of optimised single-  
17 instrument PMF solutions to avoid bias due to differing instrument characteristics or error models.  
18 Factor profile constraints require the construction of a reference profile, which may be challenging in a  
19 multi-instrument dataset. We therefore provide methods for reference profile construction for cases  
20 when (1) a single reference profile exists combining data from both instruments; (2) reference profile  
21 exist independently for each instrument; and (3) a factor is detectable by one instrument but not the  
22 other. To explore the solution stability and the uncertainties, a protocol for combined bootstrap  
23 analysis/constraint exploration is developed.~~

24 ~~Note that while these methods provide a general procedure for cPMF analysis, the specific parameters  
25 employed (i.e., the number of factors ( $p$ ), instrument weighting parameter ( $C_{inst}$ ), and the factors to be  
26 constrained and the tightness of constraints ( $a$  value ranges)) are dataset-specific and should be  
27 determined independently for each new analysis.~~

28 The cPMF method intrinsically provides factor-dependent sensitivities ( $\text{cps } / (\mu\text{g}/\text{m}^3 (\mu\text{g } \text{m}^{-3})^{-1})$ ) for the  
29 EESI-TOF. To account for organonitrate content, the AMS ions  $\text{NO}^+$  and  $\text{NO}_2^+$  are included in the  
30 cPMF analysis. Organic and inorganic contributions to these ions are estimated on a factor-by-factor  
31 basis using the method of Kiendler-Scharr et al. (2016).

32 For practical reasons, sensitivities between winter and summer campaigns are compared using cooking-  
33 related OA (COA) as a common reference. The retrieved factor sensitivities range from approximately  
34 1.3 to 7.5 times the sensitivity of COA. The relative sensitivities of SOA factors are precursor-  
35 dependent, and qualitatively consistent with trends observed in lab measurements of SOA from single  
36 precursors (Lopez-Hilfiker et al., 2019). The SOA sensitivities estimated using our cPMF approach also  
37 agree with the sensitivities predicted by multi-variate regression models (~~Wang et al., 2021~~), which  
38 ~~further demonstrates that SOA sensitivities are precursor- and/or source-dependent.~~ (Wang et al., 2021),  
39 ~~which further demonstrates that SOA sensitivities are precursor- and/or source-dependent.~~ Comparison  
40 of source apportionment results using factor-dependent sensitivities to uncorrected results show  
41 substantial differences, highlighting the importance of quantitative analysis. For example, before  
42 applying factor-dependent sensitivities, the contribution of a daytime SOA factor is underestimated by  
43 about 30 % (22.7 % before vs 35.2 % after), whereas the contribution of a nighttime SOA factor is  
44 almost overestimated by a factor of 3 in the summer campaign (29.7 % before vs 10.3 % after). As for

1 the winter campaign, the contribution of less-aged biomass burning factor to total OA in Zurich winter  
2 dataset is 35.7 %, making it a major factor in winter without considering its factor-dependent sensitivity.  
3 However, this factor is significantly overestimated by more than a factor of 2 (35.7 %, before vs 14.9 %  
4 after). In contrast, the SOA1 factor in winter is underestimated, with its contribution increasing from  
5 12.7% to 22.0 %.

6 These considerable differences in the source contributions between the uncorrected EESI-TOF and  
7 cPMF results highlight the challenges in interpreting standalone source apportionment results for  
8 instruments where ion-specific sensitivity information is not readily available, such as EESI-TOF or  
9 FIGAERO-CIMS. Although the time trends of such analyses are likely robust, interpretation of the  
10 relative composition requires caution. Therefore, if such interpretation is desired, it is advised to employ  
11 analysis strategies such as cPMF that are capable of integrating quantitative measurements from  
12 reference instruments.

13 The cPMF method presented herein ~~is~~ can be utilised as-is not only for the AMS/EESI-TOF  
14 combination, but to any dataset comprising data from multiple instruments. As such, it provides a  
15 promising strategy for utilising instruments with high chemical resolution but semi-quantitative  
16 performance (i.e., a linear but hard-to-calibrate response to mass) within the framework of a quantitative  
17 source apportionment.

18

19

20 *Data Availability.* The data presented in the text and figures will be available at the Zenodo Online repository  
21 (<https://zenodo.org>) upon final publication.

22 *Competing interests.* The authors declare that they have no conflict of interest.

23 *Author contributions.* GS and LQ conducted the campaigns in summer and winter in Zurich, respectively. YT  
24 performed the whole analysis. DSW performed the multi-variate model for machine learning parameterisation of  
25 sensitivities. FC developed the weighting and constraining functions in SoFi. JGS conceived and supervised the  
26 project. All authors currently working at PSI contributed to the data interpretation. All authors contributed to the  
27 manuscript revision.

28 *Acknowledgements.* We gratefully acknowledge the contribution from Dr. Anna Tobler and Mr. Gang Chen for  
29 coordinating the workstation for the computationally-intensive bootstrap analysis.

30 *Financial support.* This project has received funding from the Swiss National Science Foundation (grant no.  
31 BSSGI0\_155846) and the European Union's Horizon 2020 Research and Innovation Program under the Marie  
32 Skłodowska-Curie grant agreement no. 701647.

33

34

35

1

2 **Reference**

3 Alfara, M. R., Prevot, A. S. H., Szidat, S., Sandradewi, J., Weimer, S., Lanz, V. A., Schreiber, D.,  
4 Mohr, M., and Baltensperger, U.: Identification of the mass spectral signature of organic aerosols  
5 from wood burning emissions, *Environ. Sci. Technol.*, 41, 5770-5777,  
6 <https://doi.org/10.1021/es062289b>, 2007.

7 Allan, J. D., Jimenez, J. L., Williams, P. I., Alfara, M. R., Bower, K. N., Jayne, J. T., Coe, H., and  
8 Worsnop, D. R.: Quantitative sampling using an Aerodyne aerosol mass spectrometer: I. Techniques  
9 of data interpretation and error analysis (vol 108, art no 4090, 2003), *J. Geophys. Res. Atmos.*, 108,  
10 4090, <https://doi.org/10.1029/2002JD002358>, 2003.

11 Beelen, R., Raaschou-Nielsen, O., Stafoggia, M., Andersen, Z. J., Weinmayr, G., Hoffmann, B., Wolf,  
12 K., Samoli, E., Fischer, P., Nieuwenhuijsen, M., Vineis, P., Xun, W. W., Katsouyanni, K.,  
13 Dimakopoulou, K., Oudin, A., Forsberg, B., Modig, L., Havulinna, A. S., Lanki, T., Turunen, A.,  
14 Oftedal, B., Nystad, W., Nafstad, P., De Faire, U., Pedersen, N. L., Ostenson, C. G., Fratiglioni, L.,  
15 Penell, J., Korek, M., Pershagen, G., Eriksen, K. T., Overvad, K., Ellermann, T., Eeftens, M., Peeters,  
16 P. H., Meliefste, K., Wang, M., Bueno-de-Mesquita, B., Sugiri, D., Kramer, U., Heinrich, J., de  
17 Hoogh, K., Key, T., Peters, A., Hampel, R., Concin, H., Nagel, G., Ineichen, A., Schaffner, E., Probst-  
18 Hensch, N., Kunzli, N., Schindler, C., Schikowski, T., Adam, M., Phuleria, H., Vilier, A., Clavel-  
19 Chapelon, F., Declercq, C., Grioni, S., Krogh, V., Tsai, M. Y., Ricceri, F., Sacerdote, C., Galassi, C.,  
20 Migliore, E., Ranzi, A., Cesaroni, G., Badaloni, C., Forastiere, F., Tamayo, I., Amiano, P.,  
21 Dorransoro, M., Katsoulis, M., Trichopoulou, A., Brunekreef, B., and Hoek, G.: Effects of long-term  
22 exposure to air pollution on natural-cause mortality: an analysis of 22 European cohorts within the  
23 multicentre ESCAPE project, *Lancet*, 383, 785-795, [https://doi.org/10.1016/S0140-6736\(13\)62158-3](https://doi.org/10.1016/S0140-6736(13)62158-3),  
24 2014.

25 Bi, C., Krechmer, J. E., Frazier, G. O., Xu, W., Lambe, A. T., Claflin, M. S., Lerner, B. M., Jayne, J.  
26 T., Worsnop, D. R., Canagaratna, M. R., and Isaacman-VanWertz, G.: Quantification of isomer-  
27 resolved iodide chemical ionization mass spectrometry sensitivity and uncertainty using a voltage-  
28 scanning approach, *Atmos. Meas. Tech.*, 14, 6835-6850, <https://doi.org/10.5194/amt-14-6835-2021>,  
29 2021.

30 ~~Boyd, C. M., Sanchez, J., Xu, L., Eugene, A. J., Nah, T., Tuet, W. Y., Guzman, M. I., and Ng, N. L.:  
31 Secondary organic aerosol formation from the  $\beta$ -pinene-NO<sub>3</sub> system: effect of humidity  
32 and peroxy radical fate, *Atmos. Chem. Phys.*, 15, 7497-7522, [https://doi.org/10.5194/acp-15-7497-](https://doi.org/10.5194/acp-15-7497-2015)  
33 [2015](https://doi.org/10.5194/acp-15-7497-2015), 2015.~~

34 Brown, W. L., Day, D. A., Stark, H., Pagonis, D., Krechmer, J. E., Liu, X., Price, D. J., Katz, E. F.,  
35 DeCarlo, P. F., Masoud, C. G., Wang, D. S., Hildebrandt Ruiz, L., Arata, C., Lunderberg, D. M.,  
36 Goldstein, A. H., Farmer, D. K., Vance, M. E., and Jimenez, J. L.: Real-time organic aerosol chemical  
37 speciation in the indoor environment using extractive electrospray ionization mass spectrometry,  
38 *Indoor Air*, 31, 141-155, <https://doi.org/10.1111/ina.12721>, 2021.

39 Bruns, E. A., El Haddad, I., Slowik, J. G., Kilic, D., Klein, F., Baltensperger, U., and Prévôt, A. S. H.:  
40 Identification of significant precursor gases of secondary organic aerosols from residential wood  
41 combustion, *Scientific Reports*, 6, 27881, <https://doi.org/10.1038/srep27881>, 2016.

42 ~~Bruns, E. A., Perraud, V., Zelenyuk, A., Ezell, M. J., Johnson, S. N., Yu, Y., Imre, D., Finlayson-  
43 Pitts, B. J., and Alexander, M. L.: Comparison of FTIR and Particle Mass Spectrometry for the  
44 Measurement of Particulate Organic Nitrates, *Environ. Sci. Technol.*, 44, 1056-1061,  
45 <https://doi.org/10.1021/es9029864>, 2010.~~

46 Canagaratna, M. R., Jayne, J. T., Jimenez, J. L., Allan, J. D., Alfara, M. R., Zhang, Q., Onasch, T. B.,  
47 Drewnick, F., Coe, H., Middlebrook, A., Delia, A., Williams, L. R., Trimborn, A. M., Northway, M.  
48 J., DeCarlo, P. F., Kolb, C. E., Davidovits, P., and Worsnop, D. R.: Chemical and microphysical  
49 characterization of ambient aerosols with the aerodyne aerosol mass spectrometer, *Mass Spectrom.*  
50 *Rev.*, 26, 185-222, <https://doi.org/10.1002/mas.20115>, 2007.

51 Canonaco, F., Crippa, M., Slowik, J. G., Baltensperger, U., and Prevot, A. S. H.: SoFi, an IGOR-  
52 based interface for the efficient use of the generalized multilinear engine (ME-2) for the source

Field Code Changed

Field Code Changed

Field Code Changed

Field Code Changed

Field Code Changed

Field Code Changed

Field Code Changed

1 apportionment: ME-2 application to aerosol mass spectrometer data, *Atmos. Meas. Tech.*, **6**, 3649-  
2 3661, <https://doi.org/10.5194/amt-6-3649-2013>, 2013.

3 Canonaco, F., Tobler, A., Chen, G., Sosedova, Y., Slowik, J. G., Bozzetti, C., Daellenbach, K. R., El  
4 Haddad, I., Crippa, M., Huang, R. J., Furger, M., Baltensperger, U., and Prévôt, A. S. H.: A new  
5 method for long-term source apportionment with time-dependent factor profiles and uncertainty  
6 assessment using SoFi Pro: application to 1 year of organic aerosol data, *Atmos. Meas. Tech.*, **14**,  
7 923-943, <https://doi.org/10.5194/amt-14-923-2021>, 2021.

8 Chen, Y., Takeuchi, M., Nah, T., Xu, L., Canagaratna, M. R., Stark, H., Baumann, K., Canonaco, F.,  
9 Prévôt, A. S. H., Huey, L. G., Weber, R. J., and Ng, N. L.: Chemical characterization of secondary  
10 organic aerosol at a rural site in the southeastern US: insights from simultaneous high-resolution time-  
11 of-flight aerosol mass spectrometer (HR-ToF-AMS) and FIGAERO chemical ionization mass  
12 spectrometer (CIMS) measurements, *Atmos. Chem. Phys.*, **20**, 8421-8440,  
13 <https://doi.org/10.5194/acp-20-8421-2020>, 2020.

14 Chow, J. C., Bachmann, J. D., Wierman, S. S. G., Mathai, C. V., Malm, W. C., White, W. H.,  
15 Mueller, P. K., Kumar, N., and Watson, J. G.: Visibility: Science and regulation - Discussion, *J. Air  
16 Waste Manag. Assoc.*, **52**, 973-999, <https://doi.org/10.1016/j.atmosenv.2010.09.060>, 2002.

17 Crippa, M., El Haddad, I., Slowik, J. G., DeCarlo, P. F., Mohr, C., Heringa, M. F., Chirico, R.,  
18 Marchand, N., Sciare, J., Baltensperger, U., and Prévôt, A. S. H.: Identification of marine and  
19 continental aerosol sources in Paris using high resolution aerosol mass spectrometry, *J. Geophys. Res.*  
20 *Atmos.*, **118**, 1950-1963, <https://doi.org/10.1002/jgrd.50151>, 2013a.

21 Crippa, M., Canonaco, F., Slowik, J. G., El Haddad, I., DeCarlo, P. F., Mohr, C., Heringa, M. F.,  
22 Chirico, R., Marchand, N., Temime-Roussel, B., Abidi, E., Poulain, L., Wiedensohler, A.,  
23 Baltensperger, U., and Prévôt, A. S. H.: Primary and secondary organic aerosol origin by combined  
24 gas-particle phase source apportionment, *Atmos. Chem. Phys.*, **13**, 8411-8426,  
25 <https://doi.org/10.5194/acp-13-8411-2013>, 2013b, 2013a.

26 Crippa, M., El Haddad, I., Slowik, J. G., DeCarlo, P. F., Mohr, C., Heringa, M. F., Chirico, R.,  
27 Marchand, N., Sciare, J., Baltensperger, U., and Prévôt, A. S. H.: Identification of marine and  
28 continental aerosol sources in Paris using high resolution aerosol mass spectrometry, *J. Geophys. Res.*  
29 *Atmos.*, **118**, 1950-1963, <https://doi.org/10.1002/jgrd.50151>, 2013b.

30 Crippa, M., Canonaco, F., Lanz, V. A., Aijala, M., Allan, J. D., Carbone, S., Capes, G., Ceburnis, D.,  
31 Dall'Osto, M., Day, D. A., DeCarlo, P. F., Ehn, M., Eriksson, A., Freney, E., Hildebrandt Ruiz, L.,  
32 Hillamo, R., Jimenez, J. L., Junninen, H., Kiendler-Scharr, A., Kortelainen, A. M., Kulmala, M.,  
33 Laaksonen, A., Mensah, A., Mohr, C., Nemitz, E., O'Dowd, C., Ovadnevaite, J., Pandis, S. N., Petaja,  
34 T., Poulain, L., Saarikoski, S., Sellegri, K., Swietlicki, E., Tiitta, P., Worsnop, D. R., Baltensperger,  
35 U., and Prevot, A. S. H.: Organic aerosol components derived from 25 AMS data sets across Europe  
36 using a consistent ME-2 based source apportionment approach, *Atmos. Chem. Phys.*, **14**, 6159-6176,  
37 <https://doi.org/10.5194/acp-14-6159-2014>, 2014.

38 Cubison, M. J. and Jimenez, J. L.: Statistical precision of the intensities retrieved from constrained  
39 fitting of overlapping peaks in high resolution mass spectra, *Atmos Meas Tech*, **8**, 2333-2345,  
40 <https://doi.org/10.5194/amt-8-2333-2015>, 2015.

41 Daellenbach, K. R., Bozzetti, C., Krepelova, A. K., Canonaco, F., Wolf, R., Zotter, P., Fermo, P.,  
42 Crippa, M., Slowik, J. G., Sosedova, Y., Zhang, Y., Huang, R. J., Poulain, L., Szidat, S.,  
43 Baltensperger, U., El Haddad, I., and Prevot, A. S. H.: Characterization and source apportionment of  
44 organic aerosol using offline aerosol mass spectrometry, *Atmos. Meas. Tech.*, **9**, 23-39,  
45 <https://doi.org/10.5194/amt-9-23-2016>, 2016.

46 Daellenbach, K. R., Stefenelli, G., Bozzetti, C., Vlachou, A., Fermo, P., Gonzalez, R., Piazzalunga,  
47 A., Colombi, C., Canonaco, F., Hueglin, C., Kasper-Giebl, A., Jaffrezo, J. L., Bianchi, F., Slowik, J.  
48 G., Baltensperger, U., El-Haddad, I., and Prevot, A. S. H.: Long-term chemical analysis and organic  
49 aerosol source apportionment at nine sites in central Europe: source identification and uncertainty  
50 assessment, *Atmos. Chem. Phys.*, **17**, 13265-13282, <https://doi.org/10.5194/acp-17-13265-2017>,  
51 2017.

52 Daellenbach, K. R., Uzu, G., Jiang, J., Cassagnes, L.-E., Leni, Z., Vlachou, A., Stefenelli, G.,  
53 Canonaco, F., Weber, S., Segers, A., Kuenen, J. J. P., Schaap, M., Favez, O., Albinet, A., Aksoyoglu,  
54 S., Dommen, J., Baltensperger, U., Geiser, M., El Haddad, I., Jaffrezo, J.-L., and Prévôt, A. S. H.:

Field Code Changed

Field Code Changed

Field Code Changed

Field Code Changed

Field Code Changed

Field Code Changed

Field Code Changed

Field Code Changed

Field Code Changed

Field Code Changed

1 Sources of particulate-matter air pollution and its oxidative potential in Europe, *Nature*, 587, 414-419,  
2 <https://doi.org/10.1038/s41586-020-2902-8>, 2020.

3 Davison, A. C., and Hinkley, D. V.: Bootstrap methods and their application, Cambridge University  
4 Press, Cambridge, New York, NY, USA, <https://doi.org/10.1017/CBO9780511802843.1997.1997>.

5 DeCarlo, P. F., Kimmel, J. R., Trimborn, A., Northway, M. J., Jayne, J. T., Aiken, A. C., Gonin, M.,  
6 Fuhrer, K., Horvath, T., Docherty, K. S., Worsnop, D. R., and Jimenez, J. L.: Field-deployable, high-  
7 resolution, time-of-flight aerosol mass spectrometer, *Anal. Chem.*, 78, 8281-8289,  
8 <https://doi.org/10.1021/ac061249n>, 2006.

9 Elser, M., Huang, R. J., Wolf, R., Slowik, J. G., Wang, Q. Y., Canonaco, F., Li, G. H., Bozzetti, C.,  
10 Daellenbach, K. R., Huang, Y., Zhang, R. J., Li, Z. Q., Cao, J. J., Baltensperger, U., El-Haddad, I.,  
11 and Prevot, A. S. H.: New insights into PM<sub>2.5</sub> chemical composition and sources in two major cities  
12 in China during extreme haze events using aerosol mass spectrometry, *Atmos. Chem. Phys.*, 16, 3207-  
13 3225, <https://doi.org/10.5194/acp-16-3207-2016>, 2016.

14 Farmer, D. K., Matsunaga, A., Docherty, K. S., Surratt, J. D., Seinfeld, J. H., Ziemann, P. J., and  
15 Jimenez, J. L.: Response of an aerosol mass spectrometer to organonitrates and organosulfates and  
16 implications for atmospheric chemistry, *Proc Natl Acad Sci U S A*, 107, 6670,  
17 <https://doi.org/10.1073/pnas.0912340107>, 2010.

18 Faxon, C., Hammes, J., Le Breton, M., Pathak, R. K., and Hallquist, M.: Characterization of organic  
19 nitrate constituents of secondary organic aerosol (SOA) from nitrate-radical-initiated oxidation of  
20 limonene using high-resolution chemical ionization mass spectrometry, *Atmos. Chem. Phys.*, 18,  
21 5467-5481, <https://doi.org/10.5194/acp-18-5467-2018>, 2018.

22 Fenger, J.: Urban air quality, *Atmos. Environ.*, 33, 4877-4900, [https://doi.org/10.1016/S1352-  
23 2310\(99\)00290-3](https://doi.org/10.1016/S1352-2310(99)00290-3), 1999.

24 Forster, P., Ramaswamy, V., Artaxo, P., Berntsen, T., Betts, R., Fahey, D. W., Haywood, J., Lean, J.,  
25 Lowe, D. C., and Myhre, G.: Changes in atmospheric constituents and in radiative forcing. Chapter 2,  
26 in: *Climate Change 2007. The Physical Science Basis*, 2007.

27 Fry, J. L., Kiendler-Scharr, A., Rollins, A. W., Wooldridge, P. J., Brown, S. S., Fuchs, H., Dubé, W.,  
28 Mensah, A., dal Maso, M., Tillmann, R., Dorn, H. P., Brauers, T., and Cohen, R. C.: Organic nitrate  
29 and secondary organic aerosol yield from NO<sub>3</sub> oxidation of β-pinene evaluated using a  
30 gas-phase kinetics/aerosol partitioning model, *Atmos. Chem. Phys.*, 9, 1431-1449,  
31 <https://doi.org/10.5194/acp-9-1431-2009>, 2009.

32 Fry, J. L., Kiendler-Scharr, A., Rollins, A. W., Brauers, T., Brown, S. S., Dorn, H. P., Dubé, W. P.,  
33 Fuchs, H., Mensah, A., Rohrer, F., Tillmann, R., Wahner, A., Wooldridge, P. J., and Cohen, R. C.:  
34 SOA from limonene: role of NO<sub>3</sub> in its generation and degradation, *Atmos. Chem.  
35 Phys.*, 11, 3879-3894, <https://doi.org/10.5194/acp-11-3879-2011>, 2011.

36 Fuller, S. J., Wragg, F. P. H., Nutter, J., and Kalberer, M.: Comparison of on-line and off-line  
37 methods to quantify reactive oxygen species (ROS) in atmospheric aerosols, *Atmos. Environ.*, 92, 97-  
38 103, <https://doi.org/10.1016/j.atmosenv.2014.04.006>, 2014.

39 Halliwell, B., and Cross, C. E.: Oxygen-derived species: their relation to human disease and  
40 environmental stress, *Environ Health Perspect*, 102 Suppl 10, 5-12,  
41 <https://doi.org/10.1289/ehp.94102s105>, 1994.

42 Hu, W. W., Hu, M., Hu, W., Jimenez, J. L., Yuan, B., Chen, W. T., Wang, M., Wu, Y. S., Chen, C.,  
43 Wang, Z. B., Peng, J. F., Zeng, L. M., and Shao, M.: Chemical composition, sources, and aging  
44 process of submicron aerosols in Beijing: Contrast between summer and winter, *J. Geophys. Res.*  
45 *Atmos.*, 121, 1955-1977, <https://doi.org/10.1002/2015JD024020>, 2016.

46 Jimenez, J. L., Jayne, J. T., Shi, Q., Kolb, C. E., Worsnop, D. R., Yourshaw, I., Seinfeld, J. H.,  
47 Flagan, R. C., Zhang, X., Smith, K. A., Morris, J. W., and Davidovits, P.: Ambient aerosol sampling  
48 using the Aerodyne Aerosol Mass Spectrometer, *J. Geophys. Res. Atmos.*, 108,  
49 <https://doi.org/10.1029/2001JD001213>, 2003.

50 Jimenez, J. L., Canagaratna, M. R., Donahue, N. M., Prevot, A. S. H., Zhang, Q., Kroll, J. H.,  
51 DeCarlo, P. F., Allan, J. D., Coe, H., Ng, N. L., Aiken, A. C., Docherty, K. S., Ulbrich, I. M.,  
52 Grieshop, A. P., Robinson, A. L., Duplissy, J., Smith, J. D., Wilson, K. R., Lanz, V. A., Hueglin, C.,  
53 Sun, Y. L., Tian, J., Laaksonen, A., Raatikainen, T., Rautiainen, J., Vaattovaara, P., Ehn, M.,  
54 Kulmala, M., Tomlinson, J. M., Collins, D. R., Cubison, M. J., Dunlea, E. J., Huffman, J. A., Onasch,  
55 T. B., Alfarra, M. R., Williams, P. I., Bower, K., Kondo, Y., Schneider, J., Drewnick, F., Borrmann,

Field Code Changed

Field Code Changed

Field Code Changed

Field Code Changed

Field Code Changed

Field Code Changed

Field Code Changed

Field Code Changed

Field Code Changed

Field Code Changed



1 S., Weimer, S., Demerjian, K., Salcedo, D., Cottrell, L., Griffin, R., Takami, A., Miyoshi, T.,  
2 Hatakeyama, S., Shimono, A., Sun, J. Y., Zhang, Y. M., Dzepina, K., Kimmel, J. R., Sueper, D.,  
3 Jayne, J. T., Herndon, S. C., Trimborn, A. M., Williams, L. R., Wood, E. C., Middlebrook, A. M.,  
4 Kolb, C. E., Baltensperger, U., and Worsnop, D. R.: Evolution of Organic Aerosols in the  
5 Atmosphere, *Science*, 326, 1525-1529, <https://doi.org/10.1126/science.1180353>, 2009.

6 Junninen, H., Ehn, M., Petäjä, T., Luosujärvi, L., Kotiaho, T., Kostianen, R., Rohner, U., Gonin, M.,  
7 Fuhrer, K., Kulmala, M., and Worsnop, D. R.: A high-resolution mass spectrometer to measure  
8 atmospheric ion composition, *Atmos. Meas. Tech.*, 3, 1039-1053, [https://doi.org/10.5194/amt-3-1039-](https://doi.org/10.5194/amt-3-1039-2010)  
9 [2010](https://doi.org/10.5194/amt-3-1039-2010), 2010.

10 Kelly, F. J. and Fussell, J. C.: Size, source and chemical composition as determinants of toxicity  
11 attributable to ambient particulate matter, *Atmos. Environ.*, 60, 504-526,  
12 <https://doi.org/10.1016/j.atmosenv.2012.06.039>, 2012.

13 Kelly, J. M., Doherty, R. M., O'Connor, F. M., and Mann, G. W.: The impact of biogenic,  
14 anthropogenic, and biomass burning volatile organic compound emissions on regional and seasonal  
15 variations in secondary organic aerosol, *Atmos. Chem. Phys.*, 18, 7393-7422,  
16 <https://doi.org/10.5194/acp-18-7393-2018>, 2018.

17 Kiendler-Scharr, A., Mensah, A. A., Friese, E., Topping, D., Nemitz, E., Prevot, A. S. H., Aijala, M.,  
18 Allan, J., Canonaco, F., Canagaratna, M., Carbone, S., Crippa, M., Dall'Osto, M., Day, D. A., De  
19 Carlo, P., Di Marco, C. F., Elbern, H., Eriksson, A., Freney, E., Hao, L., Herrmann, H., Hildebrandt,  
20 L., Hillamo, R., Jimenez, J. L., Laaksonen, A., McFiggans, G., Mohr, C., O'Dowd, C., Otjes, R.,  
21 Ovadnevaite, J., Pandis, S. N., Poulain, L., Schlag, P., Sellegri, K., Swietlicki, E., Tiitta, P.,  
22 Vermeulen, A., Wahner, A., Worsnop, D., and Wu, H. C.: Ubiquity of organic nitrates from nighttime  
23 chemistry in the European submicron aerosol, *Geophys. Res. Lett.*, 43, 7735-7744,  
24 <https://doi.org/10.1002/2016gl069239>, 2016.

25 Kumar, V., Giannoukos, S., Haslett, S. L., Tong, Y., Singh, A., Bertrand, A., Lee, C. P., Wang, D. S.,  
26 Bhattu, D., Stefanelli, G., Dave, J. S., Puthussery, J. V., Qi, L., Vats, P., Rai, P., Casotto, R., Satish,  
27 R., Mishra, S., Pospisilova, V., Mohr, C., Bell, D. M., Ganguly, D., Verma, V., Rastogi, N.,  
28 Baltensperger, U., Tripathi, S. N., Prévôt, A. S. H., and Slowik, J. G.: Real-time chemical speciation  
29 and source apportionment of organic aerosol components in Delhi, India, using extractive electrospray  
30 ionization mass spectrometry, *Atmos. Chem. Phys. Discuss.*, 2021, 1-35, [https://doi.org/10.5194/acp-](https://doi.org/10.5194/acp-2021-1033)  
31 [2021-1033](https://doi.org/10.5194/acp-2021-1033), 2021.

32 Laden, F., Schwartz, J., Speizer, F. E., and Dockery, D. W.: Reduction in fine particulate air pollution  
33 and mortality - extended follow-up of the Harvard six cities study, *Am. J. Resp. Respir. Crit. Care*,  
34 *Med.*, 173, 667-672, <https://doi.org/10.1164/rccm.200503-443OC>, 2006.

35 Lanz, V. A., Alfarra, M. R., Baltensperger, U., Buchmann, B., Hueglin, C., and Prévôt, A. S. H.:  
36 Source apportionment of submicron organic aerosols at an urban site by factor analytical modelling of  
37 aerosol mass spectra, *Atmos. Chem. Phys.*, 7, 1503-1522, <https://doi.org/10.5194/acp-7-1503-2007>,  
38 2007.

39 [Lee, B. H., D'Ambro, E. L., Lopez-Hilfiker, F. D., Schobesberger, S., Mohr, C., Zawadowicz, M. A.,  
40 Liu, J., Shilling, J. E., Hu, W., Palm, B. B., Jimenez, J. L., Hao, L., Virtanen, A., Zhang, H.,  
41 Goldstein, A. H., Pye, H. O. T., and Thornton, J. A.: Resolving Ambient Organic Aerosol Formation  
42 and Aging Pathways with Simultaneous Molecular Composition and Volatility Observations, \*Acc\*  
43 \*Earth Space Chem.\*, 4, 391-402, \[10.1021/acearthspacechem.9b00302\]\(https://doi.org/10.1021/acearthspacechem.9b00302\), 2020.](https://doi.org/10.1021/acearthspacechem.9b00302)

44 Li, N., Sioutas, C., Cho, A., Schmitz, D., Misra, C., Sempf, J., Wang, M. Y., Oberley, T., Froines, J.,  
45 and Nel, A.: Ultrafine particulate pollutants induce oxidative stress and mitochondrial damage,  
46 *Environ Health Persp*, 111, 455-460, <https://doi.org/10.1289/ehp.6000>, 2003.

47 Lohmann, U. and Feichter, J.: Global indirect aerosol effects: a review, *Atmos. Chem. Phys.*, 5,  
48 715-737, <https://doi.org/10.5194/acp-5-715-2005>, 2005.

49 [Lopez-Hilfiker, F. D., Mohr, C., Ehn, M., Rubach, F., Kleist, E., Wildt, J., Mentel, T. F., Lutz, A.,  
50 Hallquist, M., Worsnop, D., and Thornton, J. A.: A novel method for online analysis of gas and  
51 particle composition: description and evaluation of a Filter Inlet for Gases and AEROsols  
52 \(FIGAERO\), \*Atmos. Meas. Tech.\*, 7, 983-1001, <https://doi.org/10.5194/amt-7-983-2014>, 2014.](https://doi.org/10.5194/amt-7-983-2014)

53 Lopez-Hilfiker, F. D., Iyer, S., Mohr, C., Lee, B. H., D'Ambro, E. L., Kurtén, T., and Thornton, J. A.:  
54 Constraining the sensitivity of iodide adduct chemical ionization mass spectrometry to multifunctional

Field Code Changed

Field Code Changed

Field Code Changed

Field Code Changed

Field Code Changed

Field Code Changed

Field Code Changed

Field Code Changed

Field Code Changed

Field Code Changed

Field Code Changed

1 organic molecules using the collision limit and thermodynamic stability of iodide ion adducts, *Atmos.*  
2 *Meas. Tech.*, 9, 1505-1512, <https://doi.org/10.5194/amt-9-1505-2016>, 2016.

3 Lopez-Hilfiker, F. D., Pospisilova, V., Huang, W., Kalberer, M., Mohr, C., Stefenelli, G., Thornton, J.  
4 A., Baltensperger, U., Prevot, A. S. H., and Slowik, J. G.: An extractive electrospray ionization time-  
5 of-flight mass spectrometer (EESI-TOF) for online measurement of atmospheric aerosol particles,  
6 *Atmos. Meas. Tech.*, 12, 4867-4886, <https://doi.org/10.5194/amt-12-4867-2019>, 2019.

7 Lopez-Hilfiker, F. D., Mohr, C., Ehn, M., Rubach, F., Kleist, E., Wildt, J., Mentel, T. F., Lutz, A.,  
8 Hallquist, M., Worsnop, D., and Thornton, J. A.: A novel method for online analysis of gas and  
9 particle composition: description and evaluation of a Filter Inlet for Gases and AERosols  
10 (FIGAERO), *Atmos. Meas. Tech.*, 7, 983-1001, <https://doi.org/10.5194/amt-7-983-2014>, 2014.

11 Mayer, H.: Air pollution in cities, *Atmos. Environ.*, 33, 4029-4037, [https://doi.org/10.1016/S1352-2310\(99\)00144-2](https://doi.org/10.1016/S1352-2310(99)00144-2), 1999.

12 Middlebrook, A. M., Bahreini, R., Jimenez, J. L., and Canagaratna, M. R.: Evaluation of  
13 Composition-Dependent Collection Efficiencies for the Aerodyne Aerosol Mass Spectrometer using  
14 Field Data, *Aerosol Sci. Technol.*, 46, 258-271, <https://doi.org/10.1080/02786826.2011.620041>, 2012.

15 Mohr, C., DeCarlo, P. F., Heringa, M. F., Chirico, R., Slowik, J. G., Richter, R., Reche, C., Alastuey,  
16 A., Querol, X., Seco, R., Penuelas, J., Jimenez, J. L., Crippa, M., Zimmermann, R., Baltensperger, U.,  
17 and Prevot, A. S. H.: Identification and quantification of organic aerosol from cooking and other  
18 sources in Barcelona using aerosol mass spectrometer data, *Atmos. Chem. Phys.*, 12, 1649-1665,  
19 <https://doi.org/10.5194/acp-12-1649-2012>, 2012.

20 Myhre, G., Shindell, D., and Pongratz, J.: Anthropogenic and natural radiative forcing, 2014.

21 Ng, N. L., Canagaratna, M. R., Jimenez, J. L., Chhabra, P. S., Seinfeld, J. H., and Worsnop, D. R.:  
22 Changes in organic aerosol composition with aging inferred from aerosol mass spectra, *Atmos. Chem.*  
23 *Phys.*, 11, 6465-6474, <https://doi.org/10.5194/acp-11-6465-2011>, 2011a.

24 Ng, N. L., Canagaratna, M. R., Jimenez, J. L., Zhang, Q., Ulbrich, I. M., and Worsnop, D. R.: Real-  
25 Time Methods for Estimating Organic Component Mass Concentrations from Aerosol Mass  
26 Spectrometer Data, *Environ. Sci. Technol.*, 45, 910-916, <https://doi.org/10.1021/es102951k>, 2011b.

27 Paatero, P., and Tapper, U.: Positive matrix factorization: A non-negative factor model with optimal  
28 utilization of error estimates of data values, *Environmetrics*, 5, 111-126,  
29 <https://doi.org/10.1002/env.3170050203>, 1994.

30 Paatero, P.: The Multilinear Engine—A Table-Driven, Least Squares Program for Solving Multilinear  
31 Problems, Including the n-Way Parallel Factor Analysis Model, *J. Comput. Graph. Stat.*, 8, 854-888,  
32 <https://doi.org/10.1080/10618600.1999.10474853>, 1999.

33 Paatero, P., and Hopke, P. K.: Discarding or downweighting high-noise variables in factor analytic  
34 models, *Anal. Chim. Acta*, 490, 277-289, [https://doi.org/10.1016/S0003-2670\(02\)01643-4](https://doi.org/10.1016/S0003-2670(02)01643-4), 2003.

35 Paatero, P. and Tapper, U.: Positive matrix factorization: A non-negative factor model with optimal  
36 utilization of error estimates of data values, *Environmetrics*, 5, 111-126,  
37 <https://doi.org/10.1002/env.3170050203>, 1994.

38 Paatero, P., Eberly, S., Brown, S. G., and Norris, G. A.: Methods for estimating uncertainty in factor  
39 analytic solutions, *Atmos. Meas. Tech.*, 7, 781-797, <https://doi.org/10.5194/amt-7-781-2014>, 2014.

40 Penner, J. E., Xu, L., and Wang, M. H.: Satellite methods underestimate indirect climate forcing by  
41 aerosols, *Proc Natl Acad Sci U S A*, 108, 13404-13408, <https://doi.org/10.1073/pnas.1018526108>,  
42 2011.

43 Pieber, S. M., El Haddad, I., Slowik, J. G., Canagaratna, M. R., Jayne, J. T., Platt, S. M., Bozzetti, C.,  
44 Daellenbach, K. R., Frohlich, R., Vlachou, A., Klein, F., Dommen, J., Miljevic, B., Jimenez, J. L.,  
45 Worsnop, D. R., Baltensperger, U., and Prevot, A. S. H.: Inorganic Salt Interference on CO<sub>2</sub><sup>+</sup> in  
46 Aerodyne AMS and ACSM Organic Aerosol Composition Studies, *Environ. Sci. Technol.*, 50, 10494-  
47 10503, <https://doi.org/10.1021/acs.est.6b01035>, 2016.

48 Pope, C. A., Burnett, R. T., Thun, M. J., Calle, E. E., Krewski, D., Ito, K., and Thurston, G. D.: Lung  
49 cancer, cardiopulmonary mortality, and long-term exposure to fine particulate air pollution, *Jama-J*  
50 *Am Med Assoc* *JAMA*, 287, 1132-1141, <https://doi.org/10.1001/jama.287.9.1132>, 2002.

51 Qi, L., Chen, M. D., Stefenelli, G., Pospisilova, V., Tong, Y. D., Bertrand, A., Hueglin, C., Ge, X. L.,  
52 Baltensperger, U., Prevot, A. S. H., and Slowik, J. G.: Organic aerosol source apportionment in  
53 Zurich using an extractive electrospray ionization time-of-flight mass spectrometer (EESI-TOF-MS) -  
54

Field Code Changed

Field Code Changed

Field Code Changed

Field Code Changed

Field Code Changed

Field Code Changed

Field Code Changed

Field Code Changed

Field Code Changed

Field Code Changed

Field Code Changed

Field Code Changed

Field Code Changed

Field Code Changed

Field Code Changed

1 Part 2: Biomass burning influences in winter, *Atmos. Chem. Phys.*, 19, 8037-8062,  
2 <https://doi.org/10.5194/acp-19-8037-2019>, 2019.

3 Qi, L., Vogel, A. L., Esmailirad, S., Cao, L., Zheng, J., Jaffrezou, J. L., Fermo, P., Kasper-Giebl, A.,  
4 Daellenbach, K. R., Chen, M., Ge, X., Baltensperger, U., Prévôt, A. S. H., and Slowik, J. G.: A 1-year  
5 characterization of organic aerosol composition and sources using an extractive electrospray  
6 ionization time-of-flight mass spectrometer (EESI-TOF), *Atmos. Chem. Phys.*, 20, 7875-7893,  
7 <https://doi.org/10.5194/acp-20-7875-2020>, 2020.

8 Reuter, S., Gupta, S. C., Chaturvedi, M. M., and Aggarwal, B. B.: Oxidative stress, inflammation, and  
9 cancer How are they linked?, *Free Radical BioRad. Biol. Med.*, 49, 1603-1616,  
10 <https://doi.org/10.1016/j.freeradbiomed.2010.09.006>, 2010.

11 ~~Rollins, A. W., Kiendler Scharr, A., Fry, J. L., Brauers, T., Brown, S. S., Dorn, H. P., Dubé, W. P.,  
12 Fuchs, H., Mensah, A., Mentel, T. F., Rohrer, F., Tillmann, R., Wegener, R., Wooldridge, P. J., and  
13 Cohen, R. C.: Isoprene oxidation by nitrate radical: alkyl nitrate and secondary organic aerosol yields,  
14 *Atmos. Chem. Phys.*, 9, 6685-6703, <https://doi.org/10.5194/acp-9-6685-2009>.~~

15 Rouvière, A., Brulfert, G., Baussand, P., and Chollet, J.-P.: Monoterpene source emissions from  
16 Chamonix in the Alpine Valleys, *Atmospheric Environment*, 40, 3613-3620,  
17 <https://doi.org/10.1016/j.atmosenv.2005.09.058>, 2006.

18 Slowik, J. G., Vlasenko, A., McGuire, M., Evans, G. J., and Abbatt, J. P. D.: Simultaneous factor  
19 analysis of organic particle and gas mass spectra: AMS and PTR-MS measurements at an urban site,  
20 *Atmos. Chem. Phys.*, 10, 1969-1988, <https://doi.org/10.5194/acp-10-1969-2010>, 2010.

21 Stefenelli, G., Pospisilova, V., Lopez-Hilfiker, F. D., Daellenbach, K. R., Hüglin, C., Tong, Y.,  
22 Baltensperger, U., Prévôt, A. S. H., and Slowik, J. G.: Organic aerosol source apportionment in  
23 Zurich using an extractive electrospray ionization time-of-flight mass spectrometer (EESI-TOF-MS) –  
24 Part 1: Biogenic influences and day–night chemistry in summer, *Atmos. Chem. Phys.*, 19, 14825-  
25 14848, <https://doi.org/10.5194/acp-19-14825-2019>, 2019.

26 Struckmeier, C., Drewnick, F., Fachinger, F., Gobbi, G. P., and Borrmann, S.: Atmospheric aerosols  
27 in Rome, Italy: sources, dynamics and spatial variations during two seasons, *Atmos. Chem. Phys.*, 16,  
28 15277-15299, <https://doi.org/10.5194/acp-16-15277-2016>, 2016.

29 Sun, Y. L., Wang, Z. F., Fu, P. Q., Yang, T., Jiang, Q., Dong, H. B., Li, J., and Jia, J. J.: Aerosol  
30 composition, sources and processes during wintertime in Beijing, China, *Atmos. Chem. Phys.*, 13,  
31 4577-4592, <https://doi.org/10.5194/acp-13-4577-2013>, 2013.

32 ~~Sun, Y. L., Zhang, Q., Schwab, J. J., Demerjian, K. L., Chen, W. N., Bae, M. S., Hung, H. M.,  
33 Hogrefe, O., Frank, B., Rattigan, O. V., and Lin, Y. C.: Characterization of the sources and processes  
34 of organic and inorganic aerosols in New York city with a high-resolution time-of-flight aerosol mass  
35 spectrometer, *Atmos. Chem. Phys.*, 11, 1581-1602, <https://doi.org/10.5194/acp-11-1581-2011>, 2011.~~

36 Sun, Y. L., Wang, Z. F., Fu, P. Q., Yang, T., Jiang, Q., Dong, H. B., Li, J., and Jia, J. J.: Aerosol  
37 composition, sources and processes during wintertime in Beijing, China, *Atmos. Chem. Phys.*, 13,  
38 4577-4592, <https://doi.org/10.5194/acp-13-4577-2013>, 2013.

39 Sun, Y. L., Du, W., Fu, P. Q., Wang, Q. Q., Li, J., Ge, X. L., Zhang, Q., Zhu, C. M., Ren, L. J., Xu,  
40 W. Q., Zhao, J., Han, T. T., Worsnop, D. R., and Wang, Z. F.: Primary and secondary aerosols in  
41 Beijing in winter: sources, variations and processes, *Atmos. Chem. Phys.*, 16, 8309-8329,  
42 <https://doi.org/10.5194/acp-16-8309-2016>, 2016a.

43 Sun, Y. L., Wang, Z. F., Wild, O., Xu, W. Q., Chen, C., Fu, P. Q., Du, W., Zhou, L. B., Zhang, Q.,  
44 Han, T. T., Wang, Q. Q., Pan, X. L., Zheng, H. T., Li, J., Guo, X. F., Liu, J. G., and Worsnop, D. R.:  
45 "APEC Blue": Secondary Aerosol Reductions from Emission Controls in Beijing, *Sci. Rep-UK*, 6,  
46 20668, <https://doi.org/10.1038/srep20668> (2016), 2016b.

47 Talhout, R., Opperhuizen, A., and van Amsterdam, J. G. C.: Sugars as tobacco ingredient: Effects on  
48 mainstream smoke composition, *Food Chem. Toxicol.*, 44, 1789-1798,  
49 <https://doi.org/10.1016/j.fct.2006.06.016>, 2006.

50 Tong, Y., Pospisilova, V., Qi, L., Duan, J., Gu, Y., Kumar, V., Rai, P., Stefenelli, G., Wang, L.,  
51 Wang, Y., Zhong, H., Baltensperger, U., Cao, J., Huang, R. J., Prévôt, A. S. H., and Slowik, J. G.:  
52 Quantification of solid fuel combustion and aqueous chemistry contributions to secondary organic  
53 aerosol during wintertime haze events in Beijing, *Atmos. Chem. Phys.*, 21, 9859-9886,  
54 <https://doi.org/10.5194/acp-21-9859-2021>, 2021.

Field Code Changed

Field Code Changed

Field Code Changed

Field Code Changed

Field Code Changed

Field Code Changed

Field Code Changed

Field Code Changed

Field Code Changed

Field Code Changed

Field Code Changed

Field Code Changed

Field Code Changed

Field Code Changed

1 Ulbrich, I. M., Canagaratna, M. R., Zhang, Q., Worsnop, D. R., and Jimenez, J. L.: Interpretation of  
2 organic components from Positive Matrix Factorization of aerosol mass spectrometric data, *Atmos.*  
3 *Chem. Phys.*, 9, 2891-2918, <https://doi.org/10.5194/acp-9-2891-2009>, 2009.

4 Vlachou, A., Tobler, A., Lamkaddam, H., Canonaco, F., Daellenbach, K. R., Jaffrezo, J. L.,  
5 Minguillón, M. C., Maasikmets, M., Teinemaa, E., Baltensperger, U., El Haddad, I., and Prevot, A. S.  
6 H.: Development of a versatile source apportionment analysis based on positive matrix factorization:  
7 a case study of the seasonal variation of organic aerosol sources in Estonia, *Atmos. Chem. Phys.*, 19,  
8 7279-7295, <https://doi.org/10.5194/acp-19-7279-2019>, 2019.

9 Wang, D. S., Lee, C. P., Krechmer, J. E., Majluf, F., Tong, Y., Canagaratna, M. R., Schmale, J.,  
10 Prévôt, A. S. H., Baltensperger, U., Dommen, J., El Haddad, I., Slowik, J. G., and Bell, D. M.:  
11 Constraining the response factors of an extractive electrospray ionization mass spectrometer for near-  
12 molecular aerosol speciation, *Atmos. Meas. Tech.*, 14, 6955-6972, [https://doi.org/10.5194/amt-14-](https://doi.org/10.5194/amt-14-6955-2021)  
13 [6955-2021](https://doi.org/10.5194/amt-14-6955-2021), 2021.

14 Xu, L., Suresh, S., Guo, H., Weber, R. J., and Ng, N. L.: Aerosol characterization over the  
15 southeastern United States using high-resolution aerosol mass spectrometry: spatial and seasonal  
16 variation of aerosol composition and sources with a focus on organic nitrates, *Atmos. Chem. Phys.*,  
17 15, 7307-7336, <https://doi.org/10.5194/acp-15-7307-2015>, 2015.

18 Xu, W. Q., Sun, Y. L., Wang, Q. Q., Zhao, J., Wang, J. F., Ge, X. L., Xie, C. H., Zhou, W., Du, W.,  
19 Li, J., Fu, P. Q., Wang, Z. F., Worsnop, D. R., and Coe, H.: Changes in Aerosol Chemistry From 2014  
20 to 2016 in Winter in Beijing: Insights From High-Resolution Aerosol Mass Spectrometry, *J. Geophys.*  
21 *Res. Atmos.*, 124, 1132-1147, <https://doi.org/10.1029/2018JD029245>, 2019.

22 Zhang, H., Yee, L. D., Lee, B. H., Curtis, M. P., Worton, D. R., Isaacman-VanWertz, G., Offenberg,  
23 J. H., Lewandowski, M., Kleindienst, T. E., Beaver, M. R., Holder, A. L., Lonneman, W. A.,  
24 Docherty, K. S., Jaoui, M., Pye, H. O. T., Hu, W., Day, D. A., Campuzano-Jost, P., Jimenez, J. L.,  
25 Guo, H., Weber, R. J., de Gouw, J., Koss, A. R., Edgerton, E. S., Brune, W., Mohr, C., Lopez-  
26 Hilfiker, F. D., Lutz, A., Kreisberg, N. M., Spielman, S. R., Hering, S. V., Wilson, K. R., Thornton, J.  
27 A., and Goldstein, A. H.: Monoterpenes are the largest source of summertime organic aerosol in the  
28 southeastern United States, *Proc Natl Acad Sci U S A*, 115, 2038,  
29 <https://doi.org/10.1073/pnas.1717513115>, 2018.

30 Zhang, J. K., Sun, Y., Liu, Z. R., Ji, D. S., Hu, B., Liu, Q., and Wang, Y. S.: Characterization of  
31 submicron aerosols during a month of serious pollution in Beijing, 2013, *Atmos. Chem. Phys.*, 14,  
32 2887-2903, <https://doi.org/10.5194/acp-14-2887-2014>, 2014.

33 Zhang, Q., Worsnop, D. R., Canagaratna, M. R., and Jimenez, J. L.: Hydrocarbon-like and  
34 oxygenated organic aerosols in Pittsburgh: insights into sources and processes of organic aerosols,  
35 *Atmos. Chem. Phys.*, 5, 3289-3311, <https://doi.org/10.5194/acp-5-3289-2005>, 2005.

36 Zhang, Q., Jimenez, J. L., Canagaratna, M. R., Ulbrich, I. M., Ng, N. L., Worsnop, D. R., and Sun, Y.  
37 L.: Understanding atmospheric organic aerosols via factor analysis of aerosol mass spectrometry: a  
38 review, *Anal. Bioanal. Chem.*, 401, 3045-3067, <https://doi.org/10.1007/s00216-011-5355-y>, 2011.

39 Zhang, Y. X., Schauer, J. J., Zhang, Y. H., Zeng, L. M., Wei, Y. J., Liu, Y., and Shao, M.:  
40 Characteristics of particulate carbon emissions from real-world Chinese coal combustion, *Environ.*  
41 *Sci. Technol.*, 42, 5068-5073, <https://doi.org/10.1021/es7022576>, 2008.

42 Zhao, J., Qiu, Y. M., Zhou, W., Xu, W. Q., Wang, J. F., Zhang, Y. J., Li, L. J., Xie, C. H., Wang, Q.  
43 Q., Du, W., Worsnop, D. R., Canagaratna, M. R., Zhou, L. B., Ge, X. L., Fu, P. Q., Li, J., Wang, Z.  
44 F., Donahue, N. M., and Sun, Y. L.: Organic Aerosol Processing During Winter Severe Haze  
45 Episodes in Beijing, *J. Geophys. Res. Atmos.*, 124, 10248-10263,  
46 <https://doi.org/10.1029/2019JD030832>, 2019.

47 Zhou, J., Zotter, P., Bruns, E. A., Stefanelli, G., Bhattu, D., Brown, S., Bertrand, A., Marchand, N.,  
48 Lamkaddam, H., Slowik, J. G., Prévôt, A. S. H., Baltensperger, U., Nussbaumer, T., El-Haddad, I.,  
49 and Dommen, J.: Particle-bound reactive oxygen species (PB-ROS) emissions and formation  
50 pathways in residential wood smoke under different combustion and aging conditions, *Atmos. Chem.*  
51 *Phys.*, 18, 6985-7000, <https://doi.org/10.5194/acp-18-6985-2018>, 2018.

Field Code Changed

Field Code Changed

Field Code Changed

Field Code Changed

Field Code Changed

Field Code Changed

Field Code Changed

Field Code Changed

Field Code Changed

Field Code Changed